On the Development of a Contactless Thermal Characterisation Technique for Micro-scale Thermoelectric Modules (μTEMs)

UNIVERSITY of LIMERICK

OLLSCOIL LUIMNIGH

Séamus Hickey, B. Eng (Hons) Biomed. Eng

A thesis submitted for the degree of Doctor of Philosophy at the School of Engineering, University of Limerick, Ireland

Supervisors

Dr. Jeff Punch, Stokes Laboratories, School of Engineering, University of Limerick

& **Dr. Nicholas Jeffers**, Nokia Bell Labs, Ireland

Submitted to the University of Limerick, December 2018

Declaration

The substance of thesis is the original work of the author, and due reference and acknowledgement has been made, where necessary, to the work of others. No part of this thesis has been submitted in candidature for any degree.

Séamus Hickey (Candidate)

Dr Jeff Punch (Supervisor)

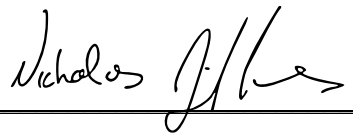

Dr Nicholas Jeffers (Supervisor)

Abstract

Contemporary internet consumer usage, in the form of social media and wide scale video streaming, has induced an exponential rise in the demand for high speed data. Optical communications infrastructure has had to evolve at a rapid pace to meet the appetite for data. Photonic Integrated Circuits (PICs) are critical components of optical communications equipment that transmit and receive coded light signals of specified wavelengths to transfer high volumes of data over optical fibres. Wavelength is sensitive to thermal fluctuations, however, with variations of as low as ± 0.1°C shifting the wavelength of the encoded signal outside design specifications. Conventional macro-scale thermoelectric modules (TEMs) are currently employed to maintain tight thermal control of PICs, but shrinking device footprints and the resultant higher heat fluxes are driving the need for smaller, micro-scale TEMs. Determining the thermal characteristics (temperature difference across the TEM, ΔT, and heat pumped by the TEM, Q_c, for a range of electrical currents through the TEM, I) of these micro TEMs (µTEMs) has emerged as a challenge, however, primarily due to their poor compressive strength (~200 MPa). Conventional characterisation techniques typically use a heat stack configuration, which involves compressing the TEM between a controlled heat source and sink combination to measure ΔT and Q_c with minimum losses at the thermal interfaces.

The objective of this thesis is to design, commission and demonstrate a novel contactless apparatus to thermally characterise a µTEM (ΔT ~ 20 K, Q_c ~ 0.3 W, I ~ 1 A) in a compression-free fashion. Compressive forces on the upper surface of the thermoelectric devices were obviated by using an infra-red (IR) source to apply a heat load to the upper surface of the TEMs, and an IR sensor was used to measure the upper surface temperature. A calorimeter was used to control the temperature of the lower surface of the TEMs as a constant reference and to determine Q_c. Measures were implemented to minimise errors due to reflected radiation within the setup, and an extensive calibration was undertaken on all measurements to minimise uncertainty. The contactless apparatus was benchmarked against a high precision conventional compression apparatus using a macro scale TEM (15 mm x 15 mm x 3 mm) in order to validate the methodology. Then, an array of twelve µTEMs on an aluminium nitride substrate (15 mm x 15 mm x 0.6 mm) was manufactured (4 x 3) in order to produce sufficient heat flow for accurate measurement. The array was characterised in both apparatuses, allowing the thermal characteristics of a single µTEM (0.83 mm x 2.14 mm 1.05 mm) to be isolated from the performance data for the array.

The contactless characterisation technique produced values for Q_c within 15 – 357 mW (1 – 25.5%) and values for ΔT within 0.4 – 6.2 K (0.5 – 7.6%) of the conventional characterisation apparatus for the macro-scale TEM. The characteristics extracted for a single µTEM measured within 15 – 100 mW (2.5 – 15%) of the conventional characterisation apparatus for Q_c, while the values for ΔT were within 0.5 – 1.9 K (1.5 – 6.5%). The thermoelectric figure of merit ZT (0.292), calculated from the Seebeck coefficient (0.0147 V/K), conductance (0.07782 W/K) and resistance (2.83 W) of the µTEM, was within ± 5.2% of the conventional compression method (0.308). It was concluded that the novel contactless characterisation method developed in this thesis could be used to accurately characterise the thermal performance of micro-scale thermoelectric devices in a compression-free manner.

Acknowledgements

This thesis is the culmination of an exceptionally long and winding road. I have been inspired, demoralised and humbled in equal measure along the way. Good friends and critical influences have entered and exited stage left as the production trundled on through ever more unlikely and scarcely believable circumstances and often staggering odds.

I wanted to do a PhD the day I started my co-op in Stokes Bio in 2009. I was in awe of intelligent and funny people who made their passion for research and their profession one and the same. Damian Curtin (my brother-in-law in the future), Kieran Curran, Dave Maguire, John Daly, Noel Sirr, Brian Barrett and Angela Morris are all part culpable for my life decisions beyond that work placement. I was enamoured with research and what it could become, where Tara Dalton and Mark Davies' ambition could take it and the doors it opened beyond Irish shores.

When I met Jeff Punch and began my post graduate journey I didn't remotely appreciate the journey I would go on. It took me to Bell Labs in Blanchardstown with John and Nick Jeffers, to Murray Hill, New Jersey and the phenomenon that is Paul Kolodner, to NYC, to Tyndall in Cork, to Denver, Colorado, Santry, Carrigtwohill, Ringaskiddy, Brussels, Eindhoven, Milan, Frankfurt, the Regional Maternity (a lot) and to every floor of the Engineering Research Building in UL (invariably with Marc, thanks desk buddy). That I was on a first name basis with the staff in the Paddocks after 3 weeks of the PhD probably reveals some of my life priorities. Lunch with Leonard, Golden and Hardiman was…. Memorable.

Jeff is the single biggest reason that I am even near enough the end to be writing acknowledgements, in a stream of consciousness fashion no less (Séamus Joyce?). Perseverance, patience and well-timed pep talks ("Toughen the *expletive* up" JP 2015) are solid attributes for a PhD supervisor. I will be forever grateful for those attributes and hopefully I can carry some of them with me. Thank you Jeff.

My meanderings have been enabled, supported, encouraged, rerouted and willed along by family. Mam and Dad, you've never doubted me in anything I have ever faced, blindly believing in the successful arrival at the end destination regardless of the road I took to get there. That belief has been fuel for 31 years and it will propel me to any lofty goal I set beyond this point. Thank you, I love you. To my brothers and sisters, Sinéad, Ronan, Seán, Caitríona, Mairéad and Cian, thank you all for caring. For effortlessly making me feel like I had an army behind me every time I went to study, work or lace up boots. Six is a borderline literal army but the metaphor still stands. I love you all beyond what conscious thought could express. My second family, my Collins family, Con, Abina, Mike, Tim, Juli and Mary. Your prayers, companionship and support have carried me when I felt like I could go no further, even more important ye have carried my children literally and figuratively for which I will be forever grateful. Fun and love is your hallmark and I pray it permeates generations.

There are 3 new people in my world since I began this endeavour, I intend to use this tome as a teachable moment in redefining possible and commitment. Who am I kidding? I'll be playing hurling in the hall and rolling around the floor with ye convinced I can postpone adulthood until ye are teenagers.

Ellen. You are an incredible person. You alter my concept of selfless love every hour of every day, I will be grateful to my dying breath for your perseverance and resolve. You inspire my desire to be the best father and husband I can be just so I can try to emulate a shadow of your capacity as a mother and wife. Thank you.

Luimneach Abu!

God is good.

Dedication

This work is for Ellen and Anna, Patrick and Matthew and whoever God decides should join us.

Contents

List of Tables

List of Figures

Nomenclature

Roman Symbols		**Units**
A	Area	m^2
C_p	Specific Heat Capacity	kg m^2 / K s^2
D	Diffusivity	m^2 / s
I	Electrical Current	A
h	Thickness	m
K	Thermal Conductance	W / K
k	Thermal Conductivity	W / m K
L	Length	m
N	Number of Thermoelectric Pairs	-
n	Negatively Doped Semiconductor	-
P	Electrical Power	W
p	Positively Doped Semiconductor	-
Q	Heat Flux	W / m^2
Q*	True Heat Flux Accounting for Losses	W / m^2
R	Electrical Resistance	Ω
r^2	Goodness of fit for 3D curve fit	-
T	Temperature	ºC, K
V	Electrical Voltage	V

x	Spatial Location	m
Z	Thermoelectric Figure of Merit	1 / K
ZT	Dimensionless Thermoelectric Figure of Merit	-

Greek Symbols		**Units**
α	Seebeck Coefficient	V / K
ΔT	Temperature Difference Across the Module	K
ΔT^*	True Temperature Difference Accounting for Losses	K
π	Peltier Coefficient	V
ρ	Density	kg / m^3
σ	Thomson Coefficient	V / K

Subscripts

+	Positive
-	Negative
c	Cold Side of TEM
e	Epoxy Support Layer
h	Hot Side of TEM
j	Junction of Dissimilar Materials
M	Module Level
max	Maximum Condition
n	Negatively Doped Semiconductor
P	Pumped from the Thermoelectric Junction
p	Positively Doped Semiconductor
S	Seebeck
su	Silicon Layer Upper

sl	Silicon Layer Lower
T	Thomson

Acronyms

AC	Alternating Current
AlN	Aluminium Nitride
CoP	Coefficient of Performance
DC	Direct Current
DSC	Differential Scanning Calorimetry
IR	Infra-Red
PIC	Photonic Integrated Circuit
PID	Proportional Integral Derivative
RTD	Resistance Temperature Detectors
TEG	Thermoelectric Generator
µTEG	Micro-Thermoelectric Generator
TEM	Thermoelectric Module
µTEM	Micro-Thermoelectric Module

Chapter 1

Introduction and Literature

With the increased miniaturisation and enhanced functionality of today's electronic and photonic devices, the resulting heat load is generated over ever decreasing footprints resulting in high device-level heat fluxes (~ 10^2 W/m^2). This creates hotspots which can adversely affect the devices' performance and reliability due to failure mechanisms such as thermo-mechanical stresses induced in the materials and packaging. The application area of communications, the focus of this thesis, has seen an explosion of innovation in data transfer and management over the past half century, in response to the increase in consumer and technological demand. In parallel with this technical and digital innovation has been an evolution of thermal engineering and heat management; this thesis focuses on this aspect of communications hardware with a view to enhancing the application of the current state-of-the-art cooling solutions for optical components in communications infrastructure.

The following sections detail the growth of the communications industry, the current state-of-the-art thermal management technology used to address its inherent challenges, and the importance of quantifying the fundamental characteristics of cooling devices. Outlines of the thesis objectives and compendium close the chapter.

1.1 Communications growth

From Morse code and tapping dot-dash messages, to Alexander Graham Bell and the first telephone transmission, we have been linked by electrical communications. The policy of

"universal service" espoused by Theodore Vail of Bell Labs in the early 20th Century was an aspiration seen as unattainable at the time, as per Bernstein [1]. It was ambition of this nature that drove the establishment of a telephone network connecting every major city across the Atlantic ocean by the middle of the century.

Having successfully connecting millions of homes and thousands of cities, the desire to communicate on the move became the next aspiration. Mobile communication was already a reality during the second world war for field communications, harnessing radio waves to wirelessly transmit voice signals. The phones were designed to communicate with each other via "towers" arranged in cells. These towers contained receivers and transmitters which relayed voice signals via a common infrastructural point. The increase in connectivity resulted in a significant increase in the volume of data being transferred by the communications infrastructure. To address the requirements for the ever-growing data volumes and the long range integrity of the signal transmissions, optical fibres were implemented as part of the communications network from the early 1980's, according to Pal [2].

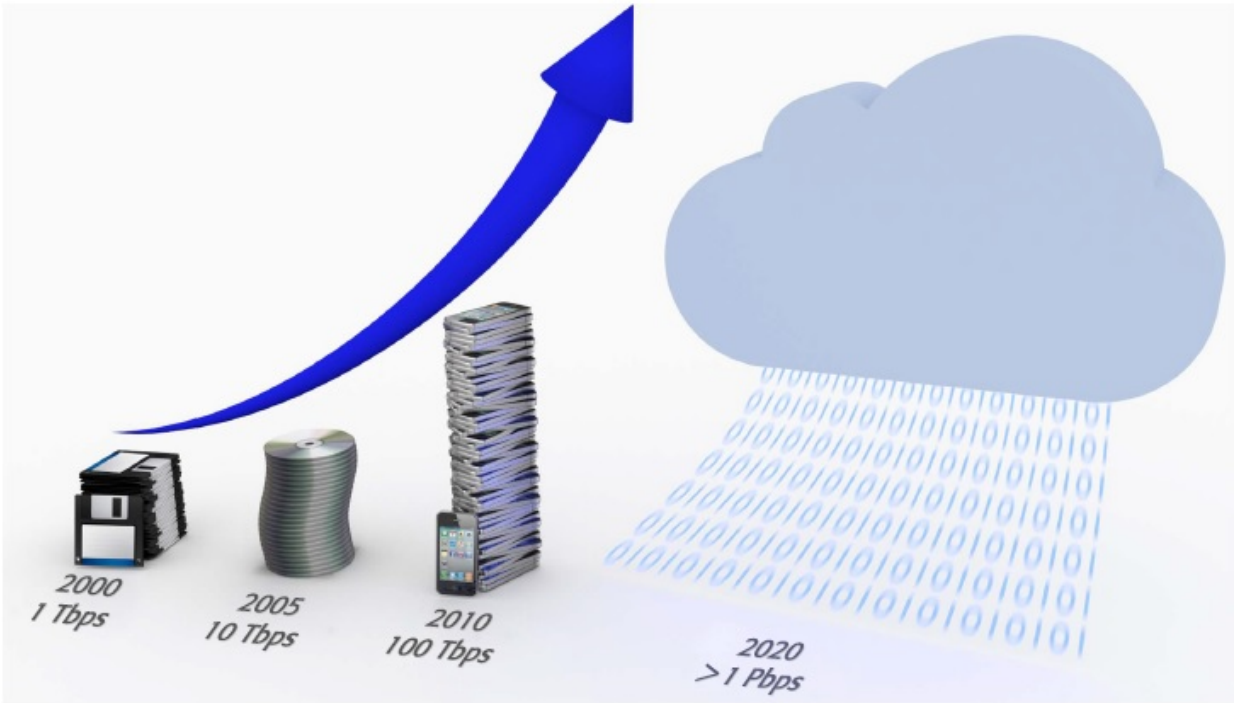

Figure 1.1: Increase in data consumption over the past two decades and expected trend to 2020 [3].

The advent of the internet in the mid 1990's resulted in an exponential growth in the demand for data usage, facilitated by the evolution of mobile device technology and an expanding range of commercial personal devices. Figure 1.1, from Enright *et al.* [3], illustrates the data consumption trend and the technical advances in devices enabling it. Currently, communications infrastructure and networks are struggling to keep pace. One of the principal reasons is the need for increased integration and miniaturisation of optical communications technology to escalate data volumes within existing network hardware.

1.2 Optical communications

Increasing demand for faster data transmission has led to the emergence of opto-electronics communications technologies, where coded light signals, generated by lasers of a specific wavelength, transfer data along optical fibres for improved data volumes per second in comparison with conventional electrical signals through copper wires, due to the superior bandwidth of optical transmission, Taubenblatt [4]. Multiple optical and electronic functionalities are combined in photonic circuits to generate and transmit light signals, in a packaging framework known as Photonic Integrated Circuits (PICs). An example of current technology in PICs is shown in Figure 1.2, where the signal generating lasers are shown. This configuration presents a complex and challenging thermal control scenario: in order to maintain the emission wavelengths of the lasers within design specifications, their operating temperature must be held within ± 0.1 K to ensure the integrity of the encoded light signal, Enright *et al.* [3]. In this scenario, removing heat alone is not sufficient and the need to maintain such a thermally constrained operating range requires artefacts with the dual ability to both heat and cool: Thermoelectric Modules (TEMs) are deployed for this purpose.

The section of a PIC shown in Figure 1.2, is composed of an optical circuit of signal generating lasers, each with their own resistive heater to "tune" the operating temperature of the laser and maintain the integrity of the signal. Also visible in the image are the track-like waveguides which carry the light signals and convey them to other discrete optical devices (such as interferometers) or to an optical fibre for transmission.

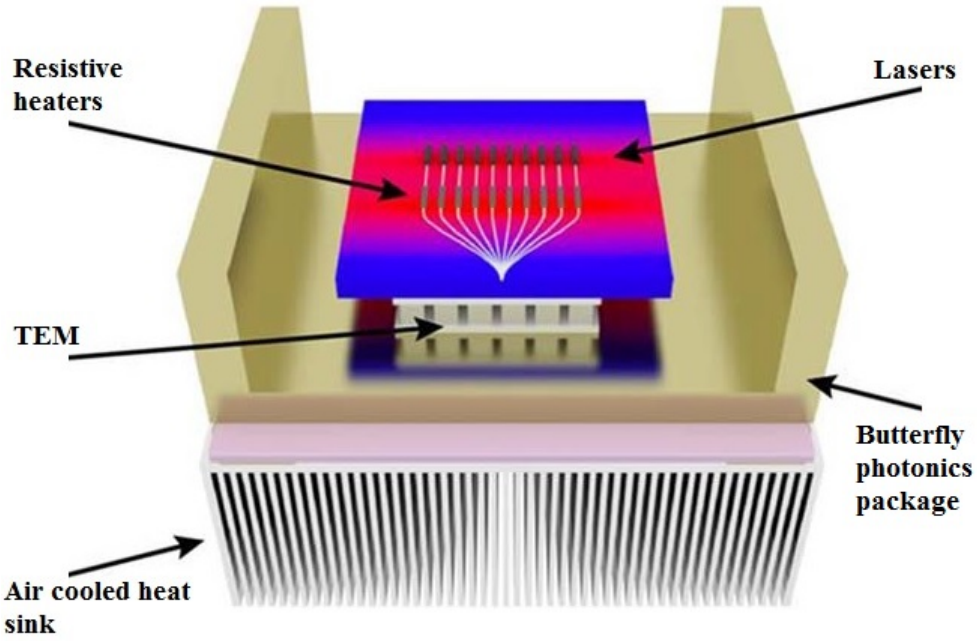

Figure 1.2: Example of butterfly PIC package comprising lasers, waveguides and resistive heaters [3].

The circuit is energy intensive, as it sits upon a heat spreading substrate, Hickey *et al.* [5], which, ideally, presents a one dimensional heat transfer path to a TEM in the order of ~ 10 mm^2 planar dimension. The TEM is responsible for cooling the entire PIC, while the resistive heaters assigned to each laser add the necessary heat required to maintain the desired signal operating temperature within ±0.1 K, Jeffers *et al.* [6]. This technique of globally cooling and locally heating is inherently inefficient and creates an energy management challenge at the server level.

In summary, the advent of high density opto-electronic components in the latter half of the 20th century brought about a necessity for the thermal control of an associated heat load occurring over an ever decreasing footprint. Energy losses from high speed data transfers, in the form of heat, need to be transferred away from the PICs in order to maintain optimal performance and device reliability. Many of the advances in communications functionality and miniaturisation, particularly in the area of PICs, can be tracked linearly with improvements in heat transfer technology and thermal process design, chief among them is the emergence of TEMs, Kraus and Bar-Cohen [7]. The following section takes a closer look at TEMs and the current state-of-the-art in thermal control for PICs.

1.3 Thermoelectric modules

TEMs, as deployed in Figure 1.2, emerged as an elegant thermal control solution for PICs in the area of optical communications. They are solid state devices, seen in Figure 1.3, made up of pairs of alternatively doped semiconductors that can cool or heat, depending on the direction of current supplied to them. They are also used in the area energy recovery, as thermoelectric generators (TEGs), due to their ability to convert temperature difference into electrical potential difference.

They possess many desirable attributes for optical communications applications, including:

- Low device profile (~ mm) which is important due to constrained slot widths in communications servers, Enright *et al.* [3].
- High device reliability with the absence of moving parts and minimal need for maintenance or servicing.
- High scalability of thermoelectric materials from macro-scale devices to thin films.
- Sub-ambient cooling which is unachievable using conventional conduction and convection methods alone.

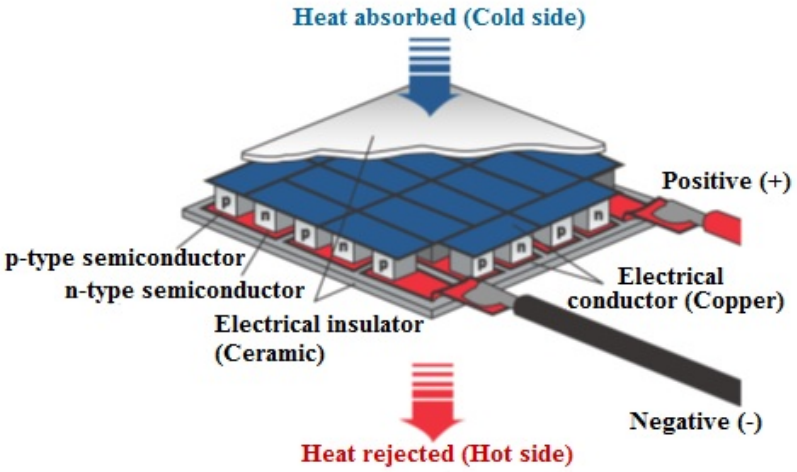

Figure 1.3: Thermoelectric module (TEM) diagram with labelled constituent parts [8].

An undesirable attribute of TEMs, however, is their low coefficient of performance (CoP) relative to other thermal control devices, such as convection heat sinks, in combination with vapour-phase refrigeration units and micro-fluidic cooling [6].

While considering the many desirable aspects of TEMs, the currently-used thermal control approach for PICs, outlined in section 1.2, remains inefficient due to cooling of the entire footprint of the PIC only to heat locally using resistive heaters. A potential improvement of this approach is to use micro thermoelectric modules, μTEMs, of the order of 1 mm^2 in planar area, to address optical components individually in order to locally control the temperature rather than over cooling the entire substrate, O'Dwyer *et al.* [9].Their suitability for the application of thermal control of PICs is an area neglected in research and requires investigation.

Determining the suitability of TEMs for use in thermal control applications is dependent on knowing the modules' performance characteristics under the desired operating conditions and being able to compare devices across a common set of measures. TEM characterisation is well understood and extensively applied for conventional macro-scale devices. Since the emergence of mass produced thermoelectric materials in the mid 1970's, methodologies to determine cooling performance and material characteristics have been developed. When characterising TEMs there are two categories to be determined:

- The first category is the fundamental thermoelectric properties of the materials that comprise the alternately doped semiconductor pairs, namely: the Seebeck coefficient, α, thermal conductance, K, and electrical resistance, R. These properties provide a base reference across devices and allow an effective comparison between different thermoelectric materials. By convention, these characteristics are combined into a figure of merit, ZT (see Chapter 2, sub-section 2.2.2).

- The second category consists of thermal performance characteristics. These are the practical comparators when determining the suitability of a TEM for use in a desired application. The performance measures are: the heat pumped from the cold side of the module, Q_c, and the temperature difference across the faces of the TEM, ΔT, expressed as functions of the current through the module, I. By convention, these are typically expressed as maxima: $Q_{c\,max}$, ΔT_{max} and I_{max}.

The methodology used to characterise TEMs depends on the category of device characteristics desired and the end application. The following sections describe relevant literature in the area of thermoelectric characterisation.

1.4 Material and thin film characterisation

The emergence of semiconductor thermoelectrics presented a need to measure and compare the materials to determine their capability and suitability for use in cooling and energy harvesting applications. Material characterisation methodologies were developed to meet this need. Among the initial widely used methodologies was that of Harman [10], which used a transient electrical technique to accurately measure the AC resistance and ZT of the thermoelectric materials. The transient electrical technique used a pulsed AC current to generate a voltage profile, seen in Figure 1.4, from which the Seebeck coefficient, α, and electrical resistance, R, could be measured. This method represents a simple and fast way to determine ZT for direct comparison of materials, as well as thermoelectric material characteristics such as α and R and, from these, the thermal conductance, K.

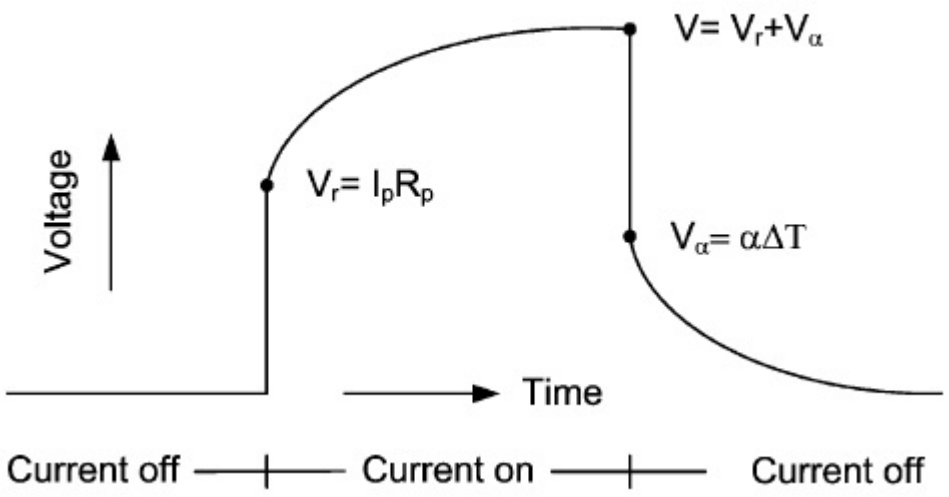

Figure 1.4: Typical voltage profile obtained from the Harman method showing the Seebeck voltage, V_α .

The Harman method has provided the basis for numerous related techniques to directly measure ZT of thermoelectric materials [11, 12, 13, 14, 15, 16, 17, 18], and it was critically important to the development of semiconductor thermoelectrics. The Harman method was, however, limited in its application to characterising thin-film thermoelectric materials when they emerged due to parasitic effects from electrical and thermal contact resistances at interfaces and heat losses through the substrate and through the electrodes used to apply electrical current to the sample, as per Castillo *et al.* [19]. This led to the use of the four point electrical characterisation technique developed by van der Pauw [20], to compensate for electrical and thermal contact resistances while accurately measuring α, R and ZT for thin films. This four point methodology was further developed by deBoor and Schmidt [21] to include the direct measurement of K also, thereby minimising the effect of parasitic thermal losses by quantifying the thermal resistance directly. A schematic representation of the four point technique is seen in Figure 1.5.

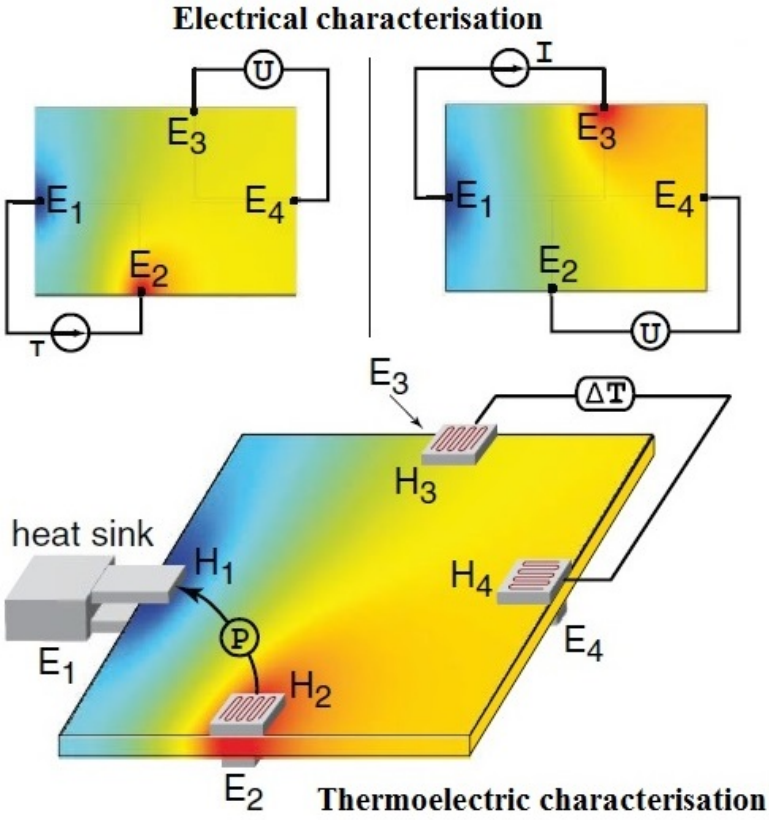

Figure 1.5: The four point electrical and thermal characterisation technique used by DeBoor and Schmidt for thin film thermoelectric materials [21].

These material characterisation methods are important to commercially available TEM manufacturers who generally use bulk material properties to model the thermoelectric behaviour of TEMs as the basis of data sheets for thermal performance quantities such as maximum temperature difference, ΔT_{max}, and maximum cold side heat pumping, $Q_{c\,max}$.

1.5 Transient electrical TEM characterisation methods

While the Harman method provided the basis for characterising thermoelectric materials, a number of methods built upon it to characterise modules (TEMs). Buist [22] developed a transient electrical method which compared the characteristics measured for α, R and ZT across multiple TEM testing configurations from suspended modules, to a single-sided heat sink and double-sided heat sinks which exhibited a more stable ΔT across the module. Buist also accounted for convective and radiative heat losses via a derived correction factor which resulted in uncertainties of less than 1.2% for ZT.

Buist's method again required K to be calculated instead of directly measured, and this was addressed by Mitrani *et al.* [23, 24] who used the transient electrical method to directly measure α, R and K for a commercially available TEM. Their experimental set-up, which can be seen below in Figure 1.6, closely resembled Buist's double-sided heat sink configuration and the set-up achieved thermal uncertainties below 0.2°C. Mitrani *et al.* apply a thermal load to the cold side of the test TEM in order to measure K, introducing a compressive force and thermal grease in order to minimise thermal interface resistances, addressing the most challenging aspect of thermal management as per Garimella [25] and Razeeb *et al.* [26].

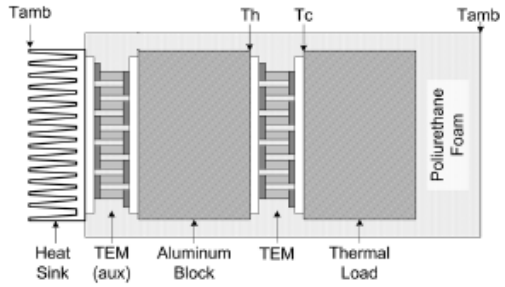

Figure 1.6: A schematic of the experimental apparatus used by Mitrani *et al.* [24].

Transient electrical characterisation techniques, based on the Harman method, utilise TEMs in "generator" mode as opposed to the "cooling" mode used in telecommunications [27, 28]. Due to this operating principle, values for Q_c as a function of ΔT are not known and require an altogether different characterisation method.

1.6 Steady-state TEM characterisation methods

Although Harman's method allowed the comparison of thermoelectric material characteristics in a quick and accurate manner, the transient electrical technique did not allow for the characterisation of TEMs in their operational conditions (such as the cooling of photonics devices). In photonics cooling applications, discrete optical components must be maintained at target operating temperature ±0.1°C. The power levels of individual devices may be small (under 10 W), but TEM efficiency is at a premium to ensure energy efficiency. In this domain, TEMs are operated at low-to-moderate electrical drive currents (~ 0.1-2 A), for two reasons.

- The first is to maximize efficiency: the CoP peaks at low currents.
- The second applies when a TEM is used in proportional integral derivative (PID) control, where the relationship between Q_c and current, I, is preferably linear to prevent losses and maintain robust control over a specified target temperature, ΔT.

These performance characteristics of ΔT and Q_c , for given values of I, are necessary when choosing a TEM for a specific application and therefore require suitable characterisation methods.

Wang *et al*. [29] developed a steady-state TEM characterisation method, shown in Figure 1.7, to measure ΔT across a test module and the Q_c through it. Heat losses due to radiation were minimised by the use of a radiation shield above the TEM in order to maintain a temperature equilibrium between the shield and the heat sink. Convection heat losses were also minimised by placing the set-up in a vacuum. These steps minimised thermal losses and yielded an overall measurement accuracy of approximately 2%.

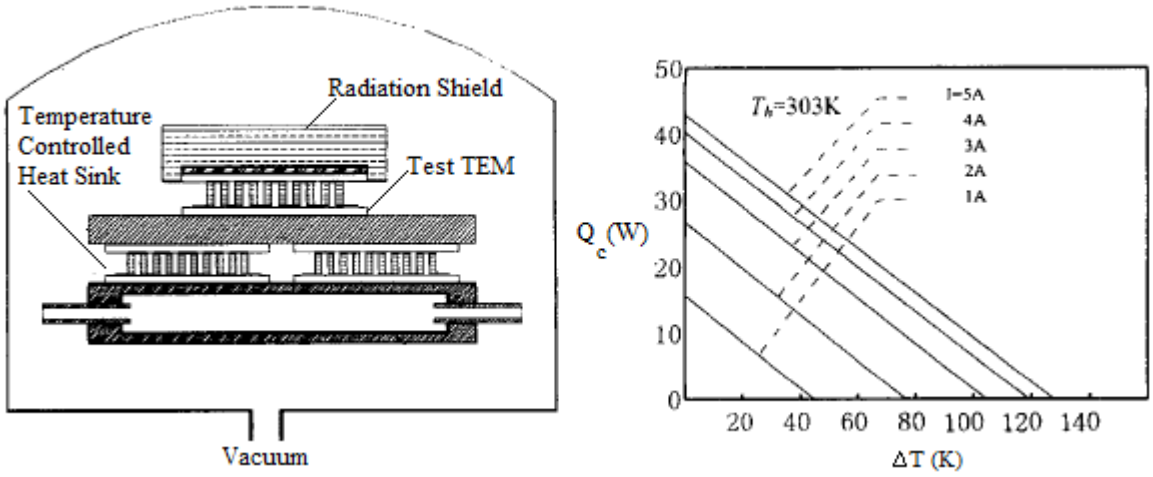

Figure 1.7: The experimental set-up developed by Wang *et al.* with sample results for ΔT as a function of Q_c for values of I [29].

Kolodner [27] further developed the steady-state apparatus with a focus on high thermal and electrical measurement precision. Kolodner took steps to eliminate or quantify all conceivable sources of stray heat in the experimental set-up: the use of a radiation shield, ~ 394 kPa TEM clamping pressure to reduce thermal contact resistances (as shown by Sandoz-Rosado *et* Stevens [30]), high vacuum and thermal guarding of electrical wires and thermistors. The apparatus has a temperature accuracy better than 0.01°C and heat flow measurement uncertainty of less than 10 mW over a range of 0 – 10 W. It is presented in greater detail in Chapter 3 as it was chosen as the bench-mark for the work of this thesis.

Other examples of steady-state TEM characterisation can be found in Lofgreen [31] and Rauscher *et al.* [32]. Lofgreen developed a thermal stack approach similar to that used by Mitrani *et al.*: parasitic losses were quantified and a compensation factor applied. Rauscher *et al.* developed a steady-state characterisation apparatus for TEMs employed in energy generation mode. They employed high vacuum and a temperature-controlled radiation shield, but their precision in temperature and power measurements was limited by the need to function at high temperature (50 - 300°C) and power (2 - 60 W) for the purposes of energy generation. While not suitable to the application of low powered TEMs for photonics, the apparatus of Rauscher *et al.* is compatible with the device powers and high temperatures seen in thermoelectric generators (TEGs).

Micro-scale thermoelectric devices are typically subjected to a variation of the transient thermal characterisation technique outlined in Section 1.4, due to the unsuitable mechanical properties of the materials under compression. Beretta *et al.* [33], however, investigated a novel steady-state characterisation apparatus for micro TEGs (μTEGs) focusing on flexible, organic thermoelectric materials which were more suitable to deformation in order to circumvent the mechanical limitations of conventional thermoelectric materials (Bi_2Te_3) for energy recovery in bio-sensor applications in wearable sensors. The measurement apparatus, shown in Figure 1.8, and approach were heavily influenced by Rauscher *et al*.

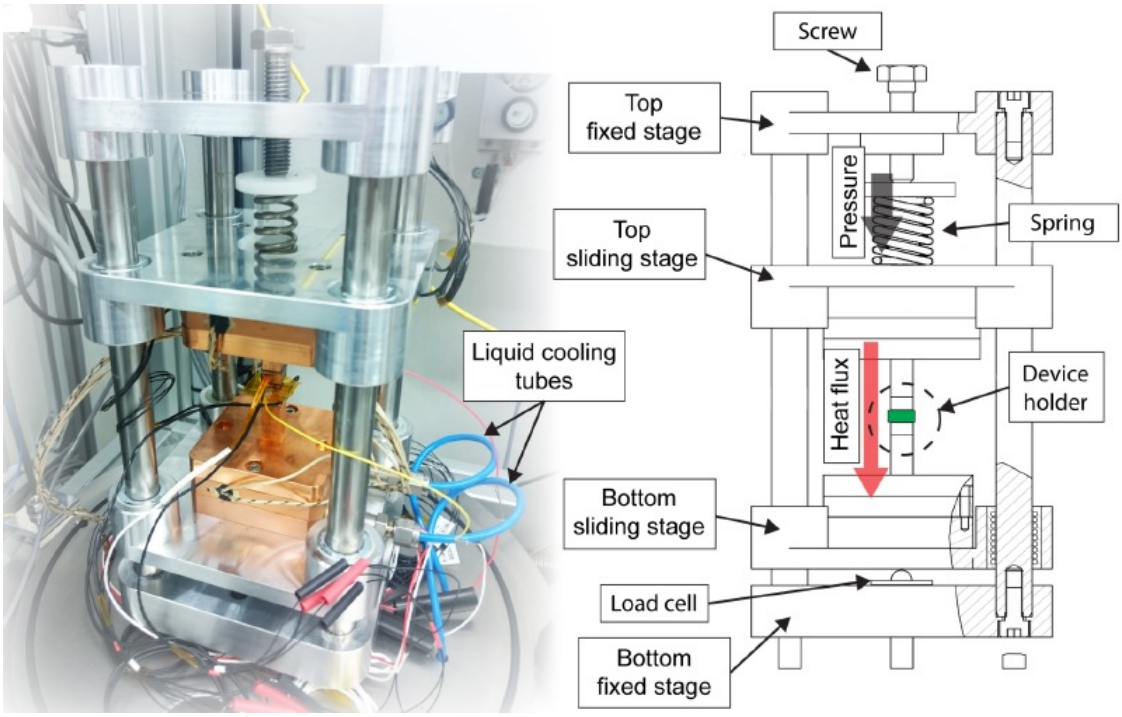

Figure 1.8: Image and schematic of the experimental apparatus used by Beretta *et al.* [33].

Beretta *et al.* determined that increasing compressive loads across the test μTEG improved power and efficiency measurement variation from 5% to 3%, a consequence of reducing the thermal contact resistances at the interface. It was also determined that again these compressive loads were unsuitable for existing μTEMs operating in refrigeration mode.

1.7 Contactless characterisation

Having established the current state-of-the-art in thermoelectric characterisation at material level and module level, the following can be summarised: bulk material properties, whether thin film or macro-scale, can be attained but do not fully translate to module level where thermal and electrical interface resistances affect thermoelectric performance and necessitate module level characterisation. Module level characterisation, both transient and steady-state, relies significantly on thermal contact being established between the heat source and the module, requiring compression of the module to minimise thermal contact resistances in the experimental set-up.

A contactless characterisation method for TEMs has already exhibited promise in characterising TEM performance under telecommunications operating conditions, Hickey *et al.* [34]. This thesis addresses the need to scale module level characterisation to micro thermoelectric modules which have potential uses for the thermal control of optical communications as well as other applications. In general, module level characteristics are currently calculated and estimated without application specific testing or characterisation.

The novel contactless method proposed in this thesis is a steady-state performance characterisation method suitable for μTEMs due to the obviation of potentially destructive compressive loads on the upper module surface. These loads are a feature of conventional state-of-the-art and high precision heat measurement techniques which measure low heat loads from the micro-scale devices with small experimental uncertainty.

1.8 Objectives

The overall aim of this thesis is to thermally characterise a single μTEM device. To this end, the following objectives are outlined:

- To design, commission and utilise a contactless characterisation apparatus for the characterisation of μTEMs.
- To bench-mark the novel contactless characterisation apparatus against a high precision conventional characterisation apparatus.

1.9 Thesis compendium

The remainder of this thesis has been divided into four chapters, which are organised as follows:

Chapter 2 Theory addresses the thermoelectric phenomena responsible for the heat pumping capability of thermoelectric materials, the governing equations for thermoelectric heat pumping, and the derived quantities considered in thermoelectric module (TEM) characterisation.

Chapter 3 Experimental Methods and Instrumentation details the novel contactless TEM characterisation apparatus and the associated experimental procedures, while also describing the conventional compression characterisation apparatus which was used as a bench-mark for this thesis.

Chapter 4 Results and Discussion presents the experimental outcomes from the bench-marking of a novel contactless TEM characterisation technique against an established conventional compression method. It also outlines the results obtained for the contactless characterisation of μTEMs and expands on the practical implications.

Chapter 5 Conclusions and Recommendations draws conclusions from the presented results, and makes recommendations for future work in the area of thermoelectric characterisation.

Chapter 2

Theory

In this thesis, the thermal performance characteristics of thermoelectric devices, both macro- and micro-scale, are investigated and characterised. This chapter describes the phenomena responsible for the heat pumping capability of thermoelectric materials, the governing equations for thermoelectric heat pumping, and the derived quantities considered in thermoelectric module (TEM) characterisation.

2.1 Thermoelectric phenomena

Thermoelectricity is the evolution or absorption of heat as a result of an electric current flowing through a material, or the temperature difference across the material, as per Kraus and Bar-Cohen [7]. The term thermoelectricity is generally used to describe three thermoelectric phenomena; namely the Seebeck, Peltier and Thomson effects which are illustrated in Figure 2.1 and described below in sub-sections 2.1.1 to 2.1.3. Thermoelectricity has been well understood for over a hundred years; Seebeck's effect was discovered in 1823, but its significance became more practical in the mid to late 20th century through advances in materials science, and particularly semiconductor technology, with the emergence of bismuth telluride (Be_2Te_3) as a high efficiency thermoelectric material relative to its metallic predecessors, Rowe [35]. Prior to these advances, thermoelectric materials had poor coefficient of performance, CoP, and figure of merit, Z, characteristics, as outlined below in section 2.2, resulting in inefficient energy conversion. The improvements in material technology

enabled the extensive use of thermoelectric materials in cooling and energy recovery applications in the communications field, automotive industry, space exploration and many more besides. In the following sub-sections, all first principles relationships and derived constitutive equations for the thermoelectric phenomena are presented with reference to Kraus and Bar-Cohen [7], unless explicitly stated.

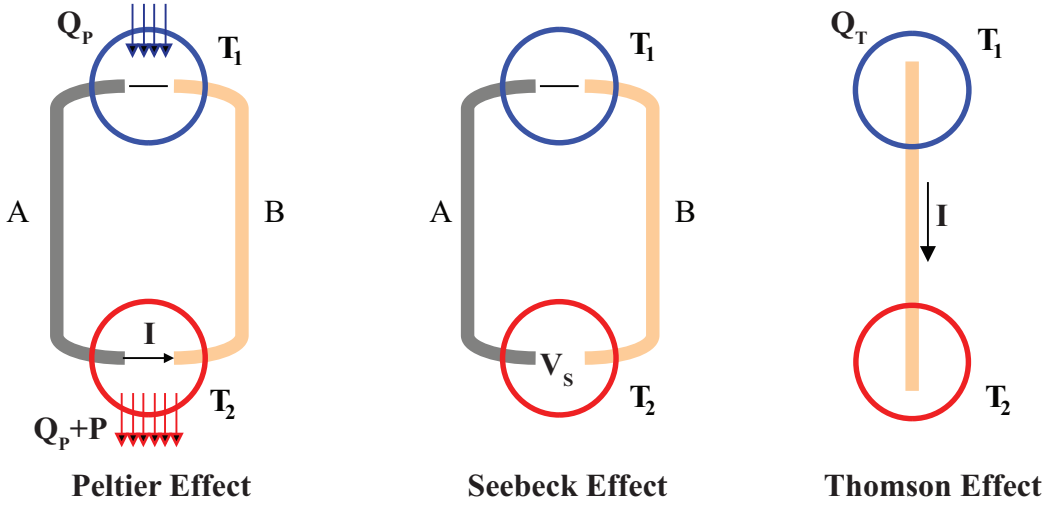

Figure 2.1: Thermoelectric phenomena: Peltier effect between dissimilar materials A and B, Seebeck effect between dissimilar materials A and B, and Thomson effect for a homogeneous conductor. All terms are described in the text.

2.1.1 Peltier effect

The Peltier effect is defined as the net emission or absorption of heat at the junction of two dissimilar materials when a electric current is passed through them. It is a junction effect that occurs at the interface of the two dissimilar materials, where electrical current through the junction causes the migration of heat from one side of the junction to the other. The amount of heat pumped, Q_P, across the junction is proportional to the magnitude of the current, I, through it, as per Equation 2.1. The Peltier coefficient, π, shown in Equation 2.2 is a material property representing the proportionality of heat flow to current; the higher the coefficient, the more heat is pumped from the junction per unit current.

$$dQ_P \sim Idt \tag{2.1}$$

$$Q_P = \pm \pi I \tag{2.2}$$

2.1.2 Seebeck effect

The Seebeck effect is defined as the net conversion of thermal energy to electrical energy under zero current conditions. A temperature difference, dT, across the junction of two dissimilar materials results in the movement of electrons across the junction, thereby creating a potential difference known as the Seebeck voltage, V_S. The magnitude of the voltage is directly proportional to the temperature difference across the junction, as per Equation 2.3. The Seebeck coefficient, α, listed in Equation 2.4 is a material property representing the proportionality of Seebeck voltage generated to the temperature difference across the junction; the higher the coefficient, the more voltage is generated per unit temperature difference.

$$dV_S \sim dT \tag{2.3}$$

$$V_S = \pm \int_{T_1}^{T_2} \alpha dT \tag{2.4}$$

2.1.3 Thomson effect

The Thomson effect is defined as the evolution or absorption of heat when a current is applied to a homogeneous conductor while maintaining a temperature difference across it. The Thomson heat flow, Q_T, in the conductor is proportional to the temperature difference across it, dT, and the current through it, I, as defined in Equation 2.5. The Thomson coefficient, σ, is a material property that represents the proportionality between the heat flow and the current through the conductor per unit temperature difference, as presented in Equation 2.6. As the relationship is directly proportional, again the higher the coefficient, the more heat flow in the conductor per unit current and temperature difference.

$$dQ_T \sim IdT\,dt \tag{2.5}$$

$$dQ_T = \pm\sigma I dT dt \tag{2.6}$$

2.1.4 Interdependence of thermoelectric coefficients

Having considered each of the thermoelectric phenomena above in isolation, it is instructive to consider their relationships to each other. Equation 2.7 is a fundamental thermodynamic representation of the energy relationship between the Seebeck , the Peltier and the Thomson effects, as found in Rowe [35]. The relationship assumes the thermoelectric circuit to be a reversible heat engine.

$$\alpha = \frac{d\pi}{dT} + \sigma \tag{2.7}$$

When considering the entropy change at a Peltier junction, the assumption of thermodynamic reversibility results in a zero entropy condition. Equation 2.8 describes the entropy change at the junction.

$$\frac{\pi}{T} = \frac{d\pi}{dT} + \sigma \tag{2.8}$$

Substituting 2.7 into 2.8 yields the relationship between the Seebeck and Peltier coefficients seen in equation 2.9, where T_j is the absolute temperature at the Peltier junction.

$$\pi = \alpha.T_j \tag{2.9}$$

The derivative of 2.9 then yields a relationship between the Thomson and Seebeck coefficient in the form of equation 2.10. The Thomson coefficient is related to the differential of the Seebeck coefficient, which implies that in cases where the Seebeck coefficient is assumed to be independent of temperature, the Thomson coefficient equates to zero.

$$\sigma = \frac{d\alpha}{dT}.T \tag{2.10}$$

For the thermoelectric materials under consideration in this thesis, bismuth telluride, the Seebeck coefficient is assumed to be invariant for a given hot side temperature, T_h, and

as a result the effects of the Thompson coefficient are neglected [7].

Having considered the thermoelectric effects that govern fundamental thermoelectric material behaviour, focus is now shifted to thermoelectric behaviour and characteristics on the module level.

2.2 Module level characteristics

This section presents the constitutive equations for the primary building block of thermoelectrics, the thermoelectric pair, and proceeds to upscale this base unit to a module level consisting of multiple pairs.

At the outset, a brief note on the notation to the thermoelectric theory in this section. In the communications environment, TEMs are deployed primarily in cooling applications. Specifically, TEMs are used to remove heat produced by signal generating lasers in PIC applications, in order to maintain a steady operating temperature. In this convention, the side of the TEM where heat is absorbed is determined the "cold side" and the side of the TEM where the heat is expelled is considered the "hot side". This thesis holds this convention throughout with reference to cold side heat pumping, Q_c, and cold side temperature, T_c, as well as their hot side counterparts[1].

The main assumptions relating to the constitutive equations below are:

- One-dimensional heat conduction (Fourier's Law) in the vertical plane only.
- Isothermal surfaces on both the hot and cold sides.
- Temperature-independent and equal magnitude thermophysical properties over the length of the semiconductor elements in the thermoelectric pair.
- Constant Seebeck coefficient over the length of the semiconductor elements, which implies that the Thomson effect can be ignored, as per sub-section 2.1.4.

[1] Other sources in literature maintain a convention that refers to controlled and uncontrolled sides of the TEM, as well as sink side to refer to the side where heat is expelled from the TEM. These sources include Hodes [36] and Lofgreen [31].

2.2.1 Thermoelectric pair

The thermoelectric pair consists of alternatively doped, positive (p_+) and negative (n_-), semiconductors connected electrically by metallic conduits, illustrated in Figure 2.2. When current is applied to the pair, the Peltier effect draws heat from the cold side of the pair and pumps it to the hot side along with the heat generated by electrical power dissipation.

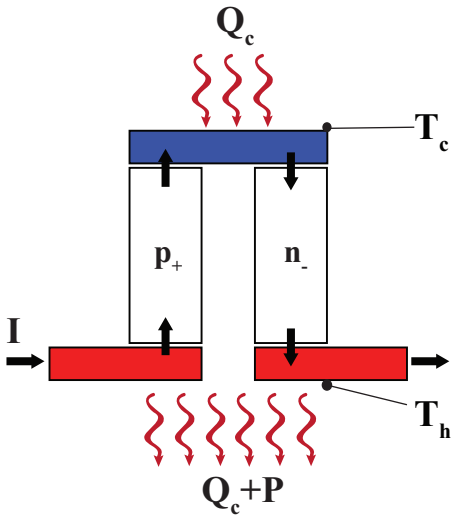

Figure 2.2: Thermoelectric pair schematic illustrating fundamental building block of TEMs. All terms are defined in the text.

The heat absorbed from the cold side, Q_c, is described in Equation 2.11:

$$Q_c = \alpha I T_c - \frac{I^2 R}{2} - K\Delta T \tag{2.11}$$

Where α is the Seebeck coefficient, I is current, T_c is the cold side temperature, R is the material electrical resistance, K is the thermal conductance of the material, and ΔT is the temperature difference between the hot and cold side of the pair. The thermoelectric heat pumping term, $\alpha I T_c$, works against the generation of Joule heat, I^2R, half of which is assumed to go *contra* the thermoelectric pumping direction, and also the back conductance, $K\Delta T$, caused by the presence of a temperature difference across the module.

The heat absorbed from the cold side of the pair is pumped to the hot side of the pair, along with the heat resulting from the electrical power, P, required to generate the temperature difference.

$$P = \alpha I \Delta T + I^2 R \tag{2.12}$$

Equation 2.12 describes the heat generated by electrical power, a combination of Joule heating and the heat generation resulting from the Seebeck voltage, $\alpha I \Delta T$.

Each material property described for the thermoelectric pair in Equations 2.11 and 2.12 incorporates the combined properties for both semiconductors, i.e. $\alpha = \alpha_p - \alpha_n$, $R = R_p + R_n$, $K = K_p + K_n$.

2.2.2 Thermoelectric module

A thermoelectric module, TEM, is a series of thermoelectric pairs connected electrically in series and thermally in parallel, with a substrate and superstrate (typically ceramic) providing common thermal sinks and mechanical structure. Figure 2.3 illustrates this relationship between pair and module. The heat pumped by the module, Q_c, scales up from the base pair in direct proportion with the number of pairs within the module.

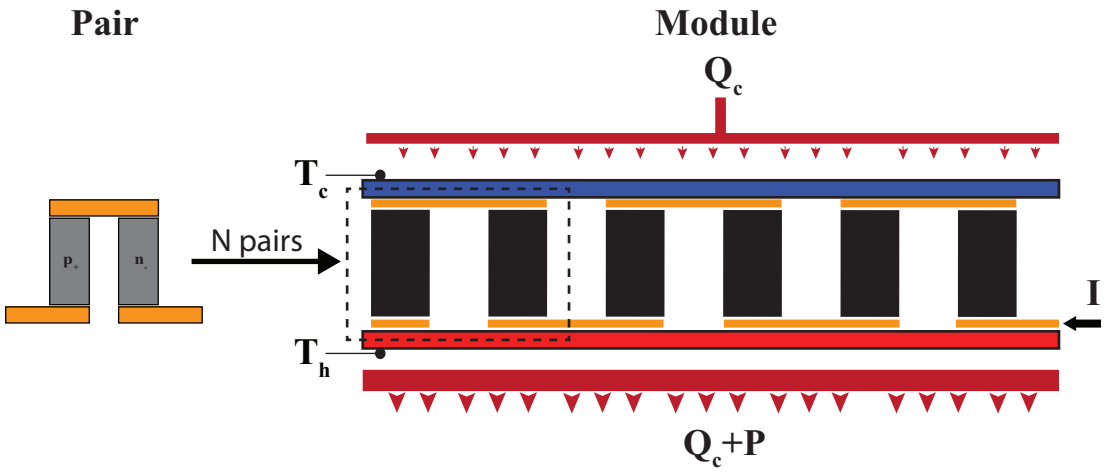

Figure 2.3: Thermoelectric module schematic with relationship of base pair to module level.

The material properties described in Equations 2.11 and 2.12 become the module level properties, α_M, R_M and K, shown in Equations 2.13 to 2.15, which are dependent on the number of pairs in the module, N.

$$\alpha_M = N\alpha \tag{2.13}$$

$$R_M = NR \tag{2.14}$$

$$K_M = NK \tag{2.15}$$

Equations 2.11 and 2.12 are combined for a relative module performance metric shown below in Equation 2.16. The coefficient of performance, CoP, is conventionally used across the field of thermodynamics to present a ratio of heat pumped versus the power required to pump it. The metric is particularly useful in device design for specific applications.

$$CoP = \frac{Q_c}{P} \tag{2.16}$$

A key comparative measure for thermoelectrics is the figure of merit, shown in Equation 2.17, which describes the relationship between the thermoelectric property of the module, α_M, and the module properties which inhibit Peltier heat flow in the TEM, as seen previously in Equation 2.11.

$$ZT = \frac{\alpha_M^2}{K_M R_M}.T_h \tag{2.17}$$

For an optimum ZT, it is desirable to have a high Seebeck coefficient, while having the lowest possible values for electrical resistance and thermal conductance.

Comparing TEMs across characterisation techniques, as done in this thesis, is most effective on the level of module level characteristics such as α_M, R_M and K_M. These provide a fundamental reference platform that is common across TEMs and application conditions. This thesis, however, yielded experimental data in the form of TEM performance values of Q_c, I and ΔT, similar to the information provided in device data sheets for TEMs by their manufacturers. Figure 2.4 shows the characteristic module performance curves usually presented by manufacturers, including highlighted points where the performance maxima

occur.

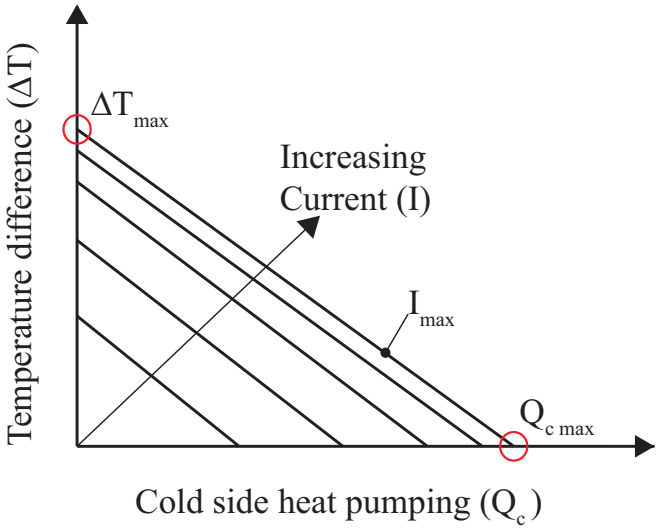

Figure 2.4: TEM level characteristic curves: temperature difference across the module as a function of cold side heat pumping, for set values of current.

It is evident from the graph that $Q_{c\,max}$ occurs when ΔT_{max} is zero and *vice versa*, and that both occur at the value for I_{max}. These performance maxima are determined by projecting the experimental data to the axes for each of the three variables; this is done using a curve-fitting tool which describes the 3D plane that the data occupies as per the governing equation for thermoelectric heat pumping, Equation 2.11. The curve-fitting tool used in this thesis is detailed in section 2.5.

Using the constitutive relationships established here, data collected in this thesis using the conventional and novel contactless apparatuses are used in Chapter 4 to plot curves of Q_c against ΔT for a range of values of I on the μTEM and macro-scale TEM level, as well as determining calculated values for module level characteristics, α_M, K_M and R_M.

2.3 Heat and temperature measurements in contactless apparatus

To quantify the thermal performance of μTEMs, the objective of this thesis, measures of temperature difference generated across the module, ΔT, are plotted as a function of heat pumped through the module, Q_c, for a given value of current, I, through the device. The

following are the relevant equations used to derive performance values from the primary measurements of the contactless characterisation apparatus, detailed further in Chapter 3.

In the contactless apparatus designed to characterise μTEMs, total heat from the hot side of the test module (or array) is measured using a calorimeter. A simplified schematic of the measurement arrangement is shown in Figure 2.5.

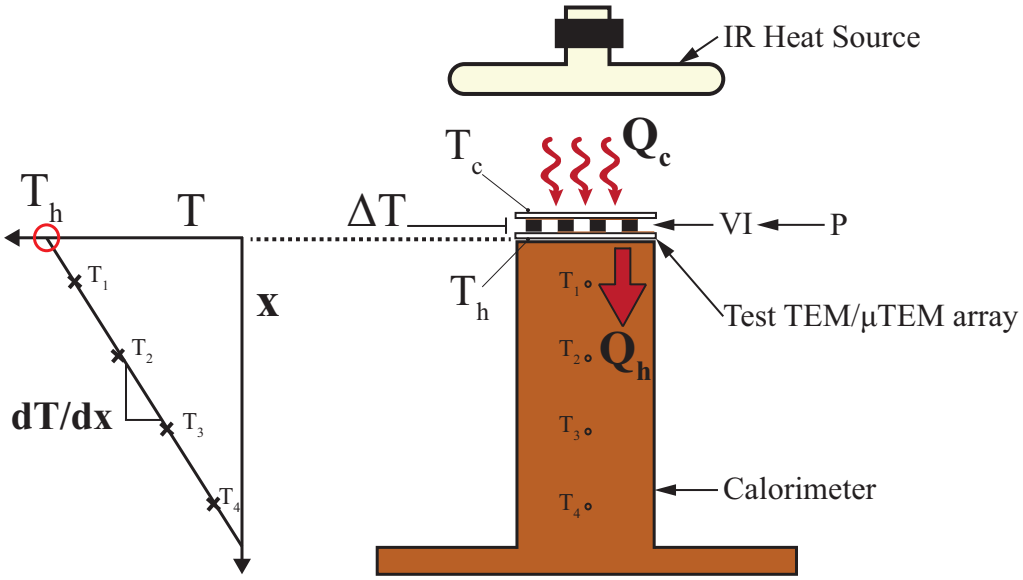

Figure 2.5: Calorimeter and temperature measurements schematic from contactless characterisation apparatus, with extrapolation method for hot side temperature and heat flow from the hot side of the module.

Heat pumped from the cold side of the module, Q_c, is defined in Equation 2.18, where Q_h is the total heat flow through the calorimeter from the hot side of the test TEM / μTEM array and P is the heat dissipation resulting from the electrical power supplied to the module. It shows that in order to isolate Q_c, the contribution of the heat generated from the electrical power supplied must first be subtracted from the heat flow measured at the module's hot side:

$$Q_c = Q_h - P \tag{2.18}$$

Heat flow through the calorimeter, presented in Equation 2.19, is calculated using a best approximation least-squares regression fit to the temperature gradient, dT/dx, in the calorimeter, illustrated in Figure 2.5. The gradient is determined using thermistors to

measure temperature at four points of known spatial positioning. This gradient, combined with the conductivity, k, of the copper calorimeter and its area, A, yields a value for heat flow from the hot side of the module, Q_h. Fourier's law of one-dimensional heat flow is assumed to apply:

$$Q_h = -kA\frac{dT}{dx} \tag{2.19}$$

Electrical power delivered to the module is defined in Equation 2.20:

$$P = VI \tag{2.20}$$

Where voltage, V, and current, I, are measured across, and through, the terminals of the module / array respectively.

Temperature difference across the module, Equation 2.21, is the calculation of difference between the constant temperature maintained at the hot side and the temperature measured on the cold side:

$$\Delta T = T_h - T_c \tag{2.21}$$

The hot side temperature of the test module is again determined using a best approximation least-squares regression fit similar to Q_h, which is in turn used to extrapolate the temperature intercept at the surface of the calorimeter, depicted in Figure 2.5. This is computed in real time using a Labview programme, the interface and block diagram of which are included in Appendix C. The cold side temperature is a direct measurement taken by the IR sensor over a spot size of ~1 mm^2 at the centre of the upper TEM surface; or, in the case of the μTEM array, the upper surface of the selected μTEM. An uncertainty analysis, expanded on later in section 3.4.3, was also employed in order to quantify the uncertainties associated with each primary measurement and their influence on the calculated properties in the TEM / μTEM performance characteristics.

2.4 Data adjustment for varying hot side temperature

For this thesis, experimental results were taken from two TEM characterisation apparatuses, described in detail in Chapter 3. Due to the design of the conventional characterisation apparatus, the desired hot side temperature, T_h, of 25°C limited the measurable temperature difference, ΔT, across the test device because of the calibration range of the apparatus (20 - 80°C, Kolodner [27]). In order to achieve a data set for a satisfactory range of ΔT, the macro-scale TEM was characterised in the conventional apparatus at T_h = 45°C. The change in baseline temperature caused a change in thermoelectric properties, as the assumption of temperature independence applied only to set values of T_h. Figure 2.6 shows the variance with temperature of thermoelectric properties for Bi_2Te_3, produced by Rauscher *et al.* [32]. It can be seen that the Seebeck coefficient and module resistance both increase with absolute hot side temperature; this leads to increased values of $Q_{c\,max}$ and ΔT_{max} for increasing values of T_h, as seen in the TEM manufacturer data sheets found in Appendix A.

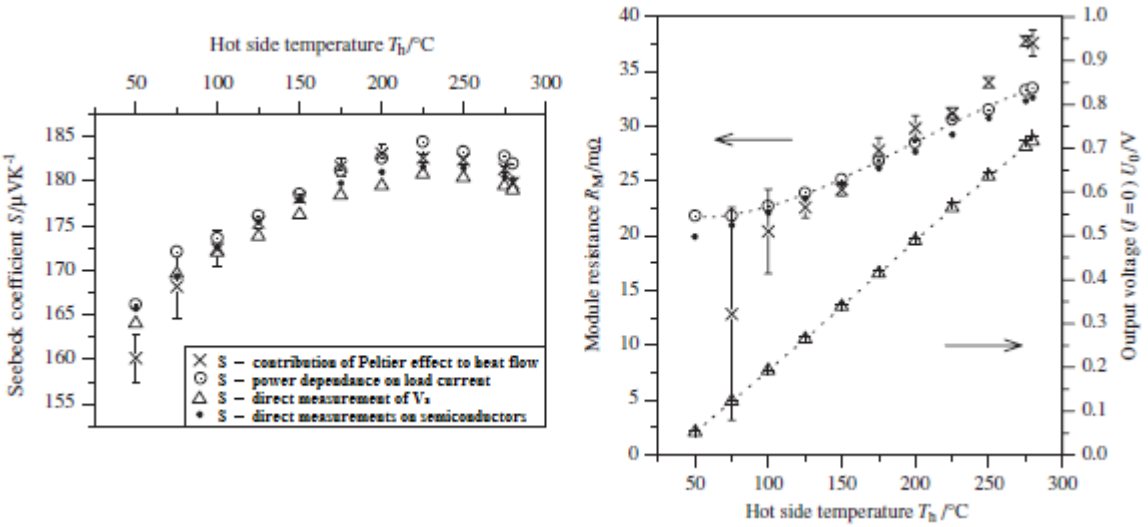

Figure 2.6: Variance of thermoelectric properties: module resistance, R_M, and Seebeck coefficient, S, of Bi_2Te_3 as per Rauscher *et al.* [32].

This change in hot side temperature necessitated a translation of the measured characteristics in order to compare across characterisation methods as set out in the thesis objectives section 1.8. The data transposition was achieved using the performance values provided in the data sheet by the manufacturer Multicomp replicated in Appendix A. The

data sheet contains performance maxima, as per sub-section 2.2.2, for T_h= 45°C and T_h= 25°C. Using the linear percentage difference between the values at the respective temperatures provides a translation for the points of $Q_{c\ max}$ and ΔT_{max}, at I_{max}. In order to apply the translation to all values of current, Equations 2.22 and 2.23 for maximum cold side heat pumping and maximum temperature difference, respectively, were derived from Equation 2.11:

$$Q_{cmax}(T_h) = \alpha_M(T_h) I T_h - \frac{I^2 R_M(T_h)}{2} \tag{2.22}$$

$$\Delta T_{max}(T_h) = \frac{\alpha_M(T_h) I T_h}{\alpha_M(T_h) I + K_M(T_h)} - \frac{I^2 R_M(T_h)}{2(\alpha_M(T_h) I + K_M(T_h))} \tag{2.23}$$

Maximum values of Q_c and ΔT were calculated for each experimental value of I for both cases of hot side temperature, 25°C and 45°C, and then used to determine a translation for each of the data points in the conventional characterisation apparatus. Thus, it allows a comparison of data taken from both characterisation apparatuses on the same TEM in order to provide a bench-mark for the novel contactless characterisation methodology.

2.5 Curve-fitting tool for data analysis

The experimental results obtained from both apparatuses in this thesis were analysed using a Matlab R2015b Curve Fitting Toolbox [37] and presented in Sections 4.1 and 4.2 in Chapter 4. The measured parameters of ΔT, Q_c and I were mapped to a 3D surface in the toolbox using the characteristic thermoelectric equation 2.11 and a non-linear least-squares regression fit. The Curve Fitting Toolbox software uses a least-squares formulation to fit a non-linear model to data. An iterative approach is applied, starting with an initial estimate for each coefficient of the governing function and adjusting the coefficients until the fit reaches the specified convergence criteria. An example of the toolbox in use can be seen in Figure 2.7.

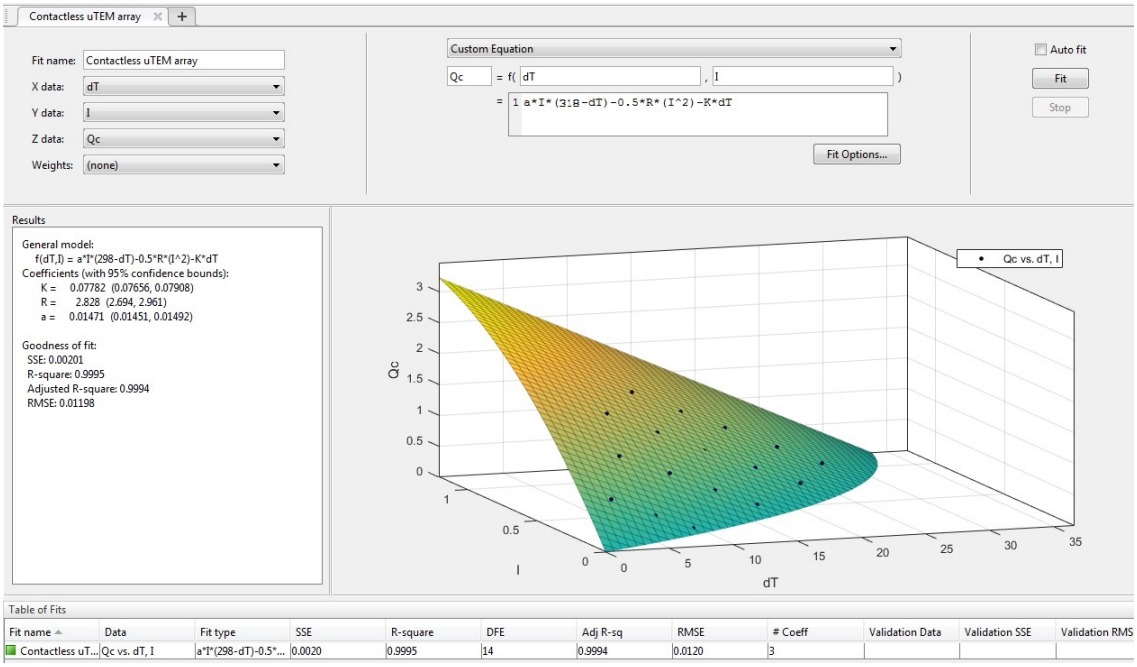

Figure 2.7: An example of the Matlab Curve Fitting Toolbox used to fit a 3D surface to the experimental data.

The use of the Curve Fitting Toolbox had two benefits in terms of analysing the experimental data:

- The extrapolation of the measured data set to the maxima of ΔT and Q_c in the regions where the experimental apparatuses could not obtain data. This was especially relevant in the region of higher I, ΔT and Q_c values obtained from the contactless apparatus. An example of this can be seen in Figure 4.1 where the curve fit generated from the experimental data was used to extrapolate to the maximum temperature difference condition where the trendlines cross the y-axis. This is discussed further in sub-section 4.1.1.

- The determination of the coefficients in the governing equation 2.11, in this case the thermoelectric characteristics of α_M, R_M and K_M, from the experimental data ΔT, Q_c and I. This is demonstrated in Table 4.3 in sub-section 4.1.3.

2.6 Summary

This chapter outlined the theoretical basis for thermoelectric phenomena and their governing equations. From these relations, module level performance characteristics of maximum temperature difference across the TEM, maximum heat pumping through the TEM and maximum electrical current, were derived and, using a methodology, equations to describe the fundamental module characteristics of Seebeck coefficient, thermal conductance and electrical resistance were presented. The following chapter describes the experimental methods and apparatuses associated with both the conventional and contactless characterisation procedures utilised in this thesis.

Chapter 3

Experimentation and Instrumentation

This chapter details the experimental methods and instrumentation used in the thermal characterisation of commercially-available TEMs and μTEMs. The devices were characterised using two methods:

- Firstly, utilising an apparatus which involved the conventional method of compressing the thermoelectric device between a heat source and sink to provide a low thermal resistance conduction path.
- Secondly, a novel contactless apparatus which obviated contact with the upper surface of the μTEMs in order to avoid mechanical compression. The validity of the contactless method was established by using the conventional characterisation apparatus as a bench-mark.

Instrumentation for both apparatuses is detailed and the procedures followed to characterise the thermoelectric devices are described. In this chapter, the measurements recorded using each characterisation method are detailed and corresponding uncertainties addressed in the subsequent data analysis for both apparatuses.

The physical, electrical and thermal properties of the TEMs and μTEMs used in both methods are listed below in section 3.1.1 and 3.1.2 respectively. In the case of the μTEMs, it was necessary to create an array of the devices in order to subject them to characterisation. Their preparation in grid-like arrays is also detailed in the section 3.1.3.

3.1 TEMs and μTEMs

This section details the thermoelectric devices subjected to the thermal characterisation methods outlined in the following sections. A single stage Multicomp TEM and an array of Micropelt μTEMs were used in each method, in order to compare values of physical module characteristics and performance parameters across both characterisation methods.

3.1.1 TEMs

A Multicomp MCPF-031-10-25 single stage TEM, with dimensions 15 mm x 15 mm x 4.8 mm, was used as the standard commercially-available TEM for direct comparison between both characterisation methods. The TEMs used for testing were adapted for electrical measurements by cutting the wires 10 mm from the positive and negative terminals and stripping the ends. Two wires were then soldered to each exposed wire to provide a four wire electrical measurement for current and voltage. Standard multi-core electrical wires, with internal diameter 1.0 mm and external diameter 1.2 mm, were used.

Multicomp MCPF-031-10-25 (and Micropelt MPC D303 μTEM) performance characteristics, as per the manufacturers' data sheets included in Appendix A, are shown in Table 3.1.

Table 3.1: Quoted performance characteristics for TEMs and μTEMs used in characterisation, as seen in Appendix A.

		TEM: Multicomp MCPF-031-10-25	**μTEM: Micropelt MPC D303**
Hot Side Temperature	$\mathbf{T_h}$ **(°C)**	25	25
Max. Electrical Current	$\mathbf{I_{max}}$ **(A)**	2.0	1.2
Electrical Resistance	**R (Ω)**	1.76	0.3
Max. Heat Pumping	$\mathbf{Q_{max}}$**(W)**	4.5	0.225
Max. Temperature Difference	$\mathbf{\Delta T_{max}}$**(°C)**	74	32

3.1.2 μTEMs

The μTEMs used were Micropelt MPC D303 modules; a schematic of the modules complete with dimensions is shown in Figure 3.1. The larger surface area of the lower half of the μTEMs allowed for greater heat removal from the base of the devices, and also provided the platform for electrical connections in the form of gold contact pads on the overlapping shoulders. The performance characteristics for the MPC D303 μTEM are outlined in Table 3.1. A key physical characteristic of the μTEMs was their low threshold for compressive forces, with the devices able to withstand only 0.52 N of downward force on the upper surface before mechanical failure, according to Micropelt's application note, shown in Appendix A. This low compressive strength is relevant considering that conventional thermoelectric characterisation methods generally rely on high compressive loads on TEMs to minimise thermal contact resistance.

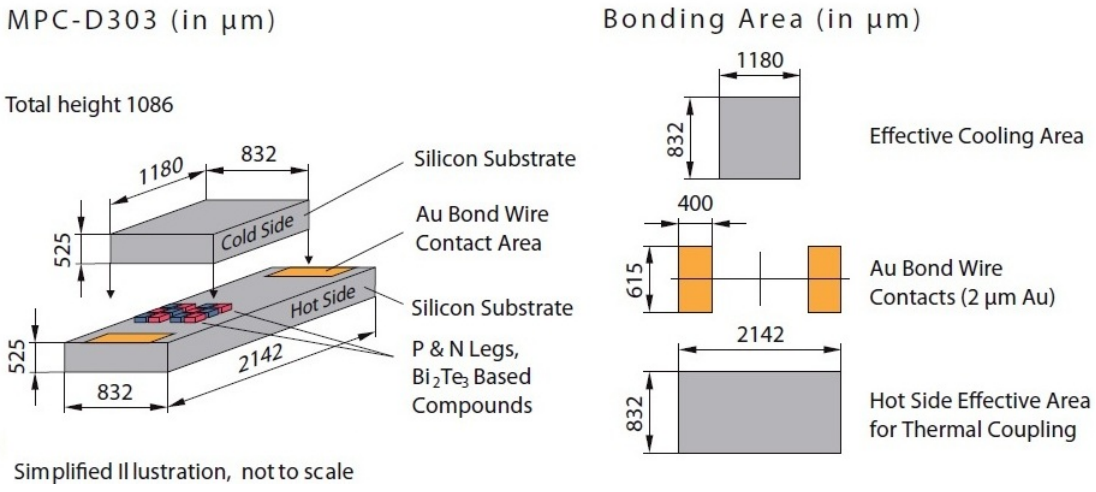

Figure 3.1: Schematic of Micropelt MPC D303 μTEM illustrating dimensions for surface areas and electrical bonding sites, as seen in Appendix A.

3.1.3 μTEMs sample preparation

Due to the small footprint of the μTEMs, 1.78 x10^{-6} m^2 (1.78 mm^2), it is physically challenging to measure temperature across the devices using conventional thermistors or thermocouples. Moreover, the measurement of heat flow in the order of 0.225 W, as per Table 3.1, is difficult without introducing large uncertainties. In order to measure the thermal

performance of a single μTEM, it was necessary to arrange multiple devices in an array. The array, a grid of 3 x 4 μTEMs, was characterised using two characterisation methods, a conventional compression method and a novel contactless characterisation technique. The array was designed with a form factor of 15 mm x 15 mm to utilise an existing compression characterisation apparatus, while the contactless apparatus was designed to accommodate the same form factor. To this end, μTEMs were laid out in a symmetrical grid pattern on an aluminium nitride (AlN) ceramic wafer, as shown in Figure 3.2. This provided a single, high conductivity (180 W/m K) heat spreader on the hot side of the μTEMs, connecting the parallel thermal paths to achieve an isothermal hot side temperature. The primary difference in the array between the two methods was the compression required for the conventional characterisation, which necessitated stress relieving mechanisms in order to preserve the functionality of the μTEMs.

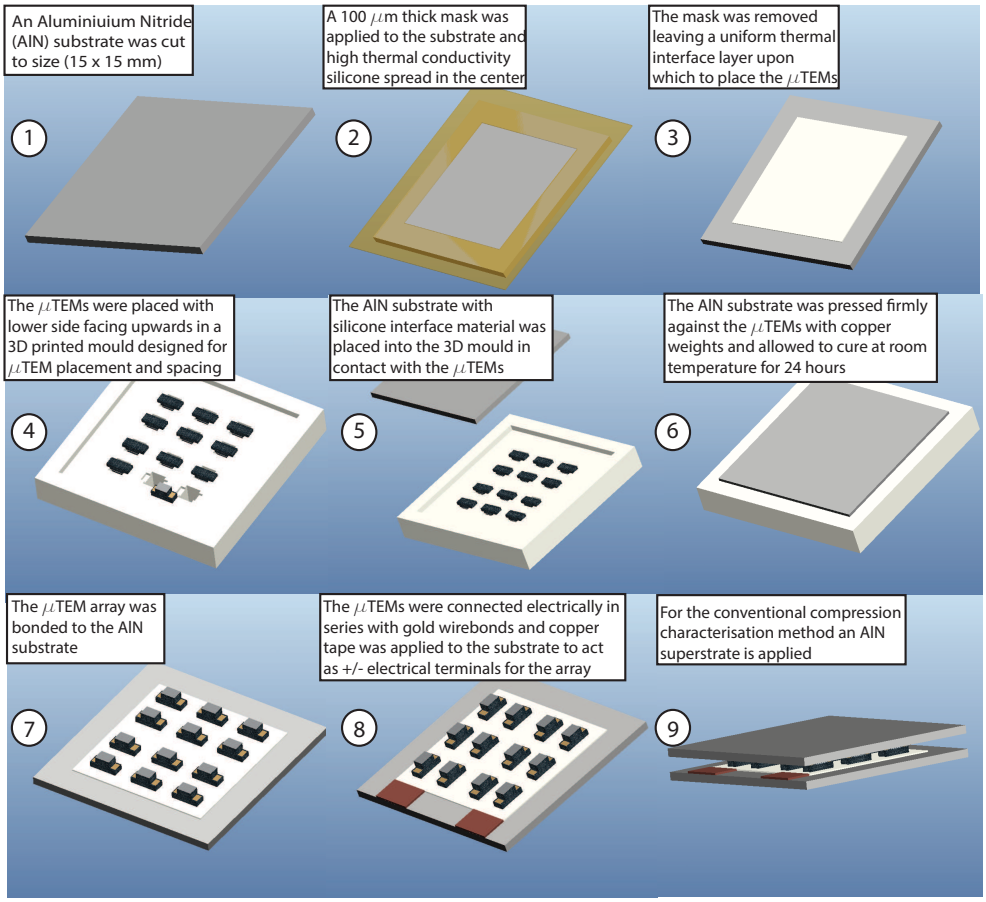

Figure 3.2: μTEM array preparation sequence.

An AlN superstrate, with identical dimensions to the substrate, was placed on the cold side of the μTEMs to spread the downward force of the apparatus over a greater area; this essentially created a macro-scale TEM with the μTEMs as the Peltier elements. To further stress relief the array, a stiff low conductivity epoxy, 3M Scotch Weld DP 190, was introduced between the upper and lower ceramic wafers sealing the perimeter of the intermediate space. The resulting heat leak through the epoxy is accounted for using the approach outlined in sub-section 4.2.1.

The procedure for μTEM array preparation was as follows (numbered steps referenced to Figure 3.2):

1. AlN sheets 0.6 mm thick were cut to 15 mm x 15 mm substrates using a diamond saw ❶.

2. High conductivity Electrolube TCOR RTV silicone (2 W/m K) was applied to the AlN substrates using a mask ❷ to create a uniform layer 100 μm thick. The silicone layer was spread over an area of 11 mm x 11 mm in the center of the substrate ❸.

3. Micropelt MPC D303 μTEMs were placed in a 3D printed mould, as seen in 3.2, for accurate spacing in grid placement. The μTEMs were placed in the mould, top first, supported by the gold bond pad with lower side surface facing up ❹.

4. The first AlN substrate, prepared with the silicone layer, was placed into the mould on top of the lower surfaces of the μTEMs ❺ with the walls of the mould ensuring repeated alignment of the AlN ❻. Three 100 g copper weights were placed on top of the substrate and the mould. The silicone was allowed a 24 hour room temperature cure and the substrate was removed from the mould with the μTEMs bonded to the surface ❼.

5. Copper tape, 100 μm thick, was cut to size and bonded, using a heat resistant 3M Scotch Weld DP 190 epoxy adhesive, to the substrate surface at each end of the μTEM grid ❽. These copper pads served as electrical terminals for the array.

6. The μTEMs were connected electrically in series using a semi-automated gold wire-bonding process. Four gold wires, 50 μm in diameter, were bonded at each positive-to-negative gold bond pad μTEM junction and to the copper terminals, yielding an effective electrical resistance of 3.825×10^{-3} Ω. Electrolube ESLE-10 silver loaded epoxy was also used to ensure that the wires remained adhered to the bond pads.

7. Standard multi-core electrical wires, with internal diameter 1.0 mm and external diameter 1.2 mm, were soldered to the copper terminals of the array. The wires were then prepared for the four terminal measurement of voltage and current as per subsection 3.1.1. This concluded the sample preparation for arrays used in the contactless characterisation apparatus.

8. For the conventional compression method, the AlN superstrate was then coated with RTV silicone, again using a mask for a uniform application 100 μm thick. Using a right angle support, the superstrate was placed and aligned on the upper surfaces of the μTEMs ❾. A 100 g copper weight was placed on top of the substrate and the silicone was allowed 24 hours to cure at room temperature.

9. In order to relieve the μTEMs from the downward pressure applied to the AlN superstrate, a 3M Scotch Weld DP 190 epoxy support structure was applied into the perimeter space between the upper and lower AlN ceramics. The epoxy penetrated approximately 2.0 mm inside the external edges of the AlN ceramic. The array was placed in an oven at 80°C for 2 hours until the epoxy set, and it was then allowed a minimum of 24 hours at room temperature before testing to ensure that maximum epoxy strength was achieved.

Once the μTEM arrays were prepared, they were characterised and the data was used to determine the thermal performance of a single μTEM and presented in Chapter 4. The characterisation methods to which the arrays were subjected are detailed in the following sections. Their physical and mechanical properties are discussed in the context of thermoelectric characterisation and their use in the characterisation methods is outlined.

3.2 Conventional compression characterisation

Characterisation of the μTEMs using the conventional compression method was carried out in Bell Laboratories, Alcatel-Lucent, Murray Hill, NJ, USA. The characterisation facility in Bell Labs was used for the following purposes:

- To establish an industry standard for TEM characterisation against which the contactless apparatus could be bench-marked.
- To provide a platform for applying conventional characterisation methods to μTEMs and a bench-mark for the contactless apparatus developed in this thesis.

Every practical step was taken to minimize heat transfer losses and uncertainty in temperature and performance measurements of the TEMs in the conventional compression method. These steps will be outlined in a detailed view of the apparatus below. For further detail on the apparatus used, refer to Kolodner [27].

3.2.1 Apparatus

The conventional compression apparatus was designed and commissioned to characterise TEMs under representative thermal control conditions. Fundamentally, the apparatus maintains a constant temperature difference across the module using a PID control circuit, and both the heat and module power required to maintain that difference are measured.

The apparatus, illustrated in Figure 3.3, had a copper base plate 177.8 mm in diameter and 25.4 mm thick. The copper was nickel plated and polished to minimize radiation heat transfer. A 15.2 mm deep trench outlined a rectangular block, 47.6 mm x 73.0 mm, at the center of the base plate. The temperature of the isolated rectangular block was water cooled within ±0.005°C using a Matlab 2XXX PID control loop including a Julabo model F32-HL bath circulator and an Omega F3105 109.8 Ω platinum RTD embedded in the copper base plate. All thermistors and RTDs in the apparatus were calibrated for the temperature range 20-80°C.

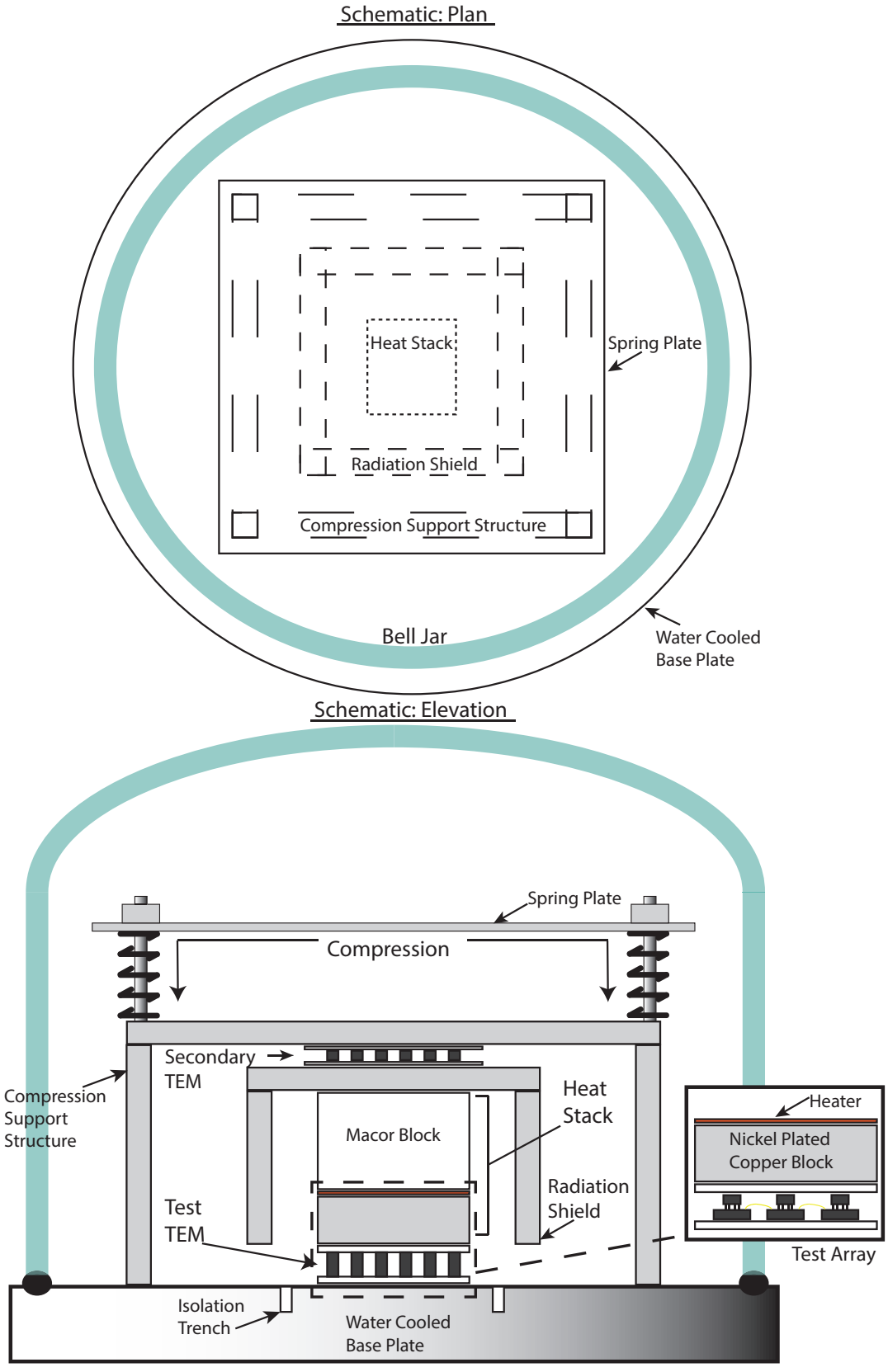

Figure 3.3: Schematic of the conventional characterisation apparatus.

The test module was placed in the center of the temperature controlled block and positioned using an alignment plate. Laird T-grease 2500 thermal grease was applied to both articulating surfaces of the test specimen. Beneath the lower surface of the module, an MS G22K7MCD419 22 kΩ thermistor was placed in a shallow groove milled in the surface of the base plate. This thermistor was used to record the temperature of the lower surface of the test device, the nominal hot side for the purposes of characterisation, to yield the measure of the hot side temperature, T_h.

Heat was applied to the upper surface of the test specimen via the heater stack, the core component of the apparatus, seen in the center of Figure 3.3. It consisted of a nickel plated copper block as a low resistance heat conduit, a film heater heat source, a high thermal resistance Macor insulation block, and a temperature-controlled radiation shield to minimise stray heat transfer. The copper heater block was in contact with the upper surface of the test TEM, which had dimensions of 14.46 mm square × 4.468 mm thick. Two further MS G22K7MCD419 22 kΩ thermistors were placed within the copper block, 2.5 mm deep and centered 0.63 mm above the bottom surface of the block in order to determine the cold side temperature of the test TEM. Above the heater block, a Birk Manufacturing Inc. thin film foil heater was attached using a thermally conductive Omegabond 200 epoxy. The film heater provided the heat to be pumped through the test TEM, with the heat stack designed for the heat flow path to be almost entirely through the copper heater block and then through the test specimen. This was achieved by the use of a high thermal resistance Macor insulation block above the film heater, with a thermal resistance of 32.3 K/W compared with 0.055 K/W for the copper heater block. It had dimensions of 14.42 mm square x 9.804 mm. The temperature of the Macor block was monitored using an MS 10K3MCD1 10 kΩ thermistor located 0.101 mm from the lower surface, and this was used to calculate conduction losses through the insulation block.

In order to minimize heat losses due to radiation from the heater block, it was surrounded by a temperature controlled radiation shield made from polished nickel plated copper. The shield consisted of a top plate in direct contact with the heater stack and four side plates extending downwards to the lower surface of the heater block, as shown in Figure 3.3. The upper surface of the Macor block was attached to the underside of the

radiation shield top plate using 3M DP 640 urethane adhesive. The temperature of the radiation shield was measured using an MS 10K3MCD1 10 kΩ thermistor located in the top plate; this allowed the calculation of the temperature differential between the Macor block and the shield and, in turn, the heat lost by conduction from the film heater. This could then be accounted for in the calculation of heat flow through the heater block. Radiation losses were also minimized using a nickel foil collar placed over the electrical wires of the test TEM during testing. The leads were soldered to electrical conduits on the base plate, which were connected to a Keithley model 2001 multimeter to measure voltage and a Fluke model 8845A multimeter for current measurements.

The temperature of the radiation shield was adjusted using a Laird Technologies HT4,7,F2,3030,11 TEM and a servo control system. The servo control made use of the ability of the TEM to both heat and cool and, therefore, to adjust the temperature as required. The mechanical support structure of the apparatus above the shield TEM acted as a thermal sink for the radiation shield to the water-cooled base plate and also contributed the downward force on the heater stack and the test sample. The force was generated by springs in place above the support structure, as seen in Figure 3.3, which were compressed by thumbscrews, with the force measured using an Omega LCCA-50 load cell. A glass bell jar was placed over the apparatus and a rubber o-ring formed a seal between it and the water cooled copper base plate. An opening in the base plate was connected to a diffusion vacuum pump and the enclosed space was evacuated to a base pressure of 0.002 Pa to minimize any convective heat losses. The internal pressure was monitored by a Granville-Philips type 355 micro-ion vacuum gauge.

3.2.2 Procedure for conventional TEM characterisation

A single-stage TEM was thermally characterised using the conventional, compression based apparatus. Using measurements of temperature difference across the array, ΔT, heat flow through it, Q, and electrical current, I, through the module, the performance of a Multicomp MCPF-031-10-25 TEM was obtained.

The characterisation procedure was as follows:

1. A uniform layer of Dow Corning DC340 heat sink compound, 0.06 mm thick, was

applied using an adhesive mask, 0.06 mm thick, and a leveling blade to both the upper and lower surfaces of the test TEM.

2. The test module was placed under the heater block using an alignment plate and the mechanical super-structure was clamped in place with a downward force of 8.5 kg, producing a clamping pressure of 394 kPa.

3. A nickel foil collar was placed over the electrical wires of the test TEM and connected to the electrical conduits in the base plate.

4. The water cooler was set to 45°C and the base plate was allowed to reach thermal steady-state. The bell jar was placed on top of the base plate and the diffusion vacuum pump was switched on. The system was allowed to reach an absolute pressure of 0.002 Pa.

5. The PID circuit for control of the temperature difference across the test TEM was switched on and allowed to reach steady-state, initially set at 0 K temperature difference between heater block and base plate, and then increased in increments of 5 K.

6. The heater power, Q_c, was set at the desired value, starting at 0 W and increased in increments of 0.5 W up to 4 W. Based on the temperature measurements from the Macor block and the shield thermistor, the heat leaked through the Macor was calculated and offset from the heat flow through the test TEM.

7. The Matlab control programme recorded measurements for T_{base}, T_{heater}, T_{macor} and T_{shield}, as well as currents and voltages for the test module and foil heater. These measurements yielded values for temperature difference across the test TEM, as well as electrical current and heat pumped through it.

3.2.3 Procedure for conventional compression characterisation of a μTEM array

The procedure for the conventional compression characterisation of the μTEM array was similar to that outlined in sub-section 3.2.2. A 4 x 3 array of Micropelt MPC D303 μTEMs was assembled as per the μTEM sample preparation procedure outlined in sub-section 3.1.3 and subjected to the characterisation. Using measurements for temperature difference across the array, ΔT, heat flow through it, Q_c, and electrical current, I, through the sample, the performance of a single μTEM was extrapolated from the measured data. The adjustments required to characterise the μTEM array in place of the TEM were as follows:

1. The downward force applied through the mechanical super structure was reduced to 6.0 kg, producing a clamping pressure of 261.6 kPa. This was to take account of the lower compressive strength of the μTEM array when compared to the that of the TEM, and to reduce the risk of fracturing the μTEM structures within the array.

2. The temperature difference across the test array was initially set at zero, between heater block and base plate, and then increased in increments of 2.5 K.

3. The heater power, Q_c, was set to 0 W and initial data was recorded. Q_c was then increased in increments of 0.4 W up to 2 W.

All other steps were as per the procedure outlined in sub-section 3.2.2.

3.3 Contactless characterisation bench-marking of TEM

The conventional compression-based characterisation method, described in section 3.2, was used to obtain the thermal performance characteristics of commercially-available TEM and μTEMs. The compressive forces used in the method were unsuitable for the routine characterisation of μTEMs, however. To address the shortcomings of the conventional methods for μTEMs, an experimental characterisation setup, illustrated in Figure 3.4, was devised to deliver heat to the upper surface of a μTEM array in a contactless fashion via an infra-red

(IR) heat source, while measuring the heat pumped through the sample, Q_c, and temperature difference across it, ΔT.

This section details the components of the experimental apparatus and the associated test procedure, in sub-section 3.3.1 and 3.3.2 respectively. An analysis of experimental measurement and uncertainty is discussed in sub-section 3.4.3, data reduction.

3.3.1 Apparatus

Figure 3.4 is a schematic illustration of the contactless experimental apparatus that was used to characterise both macro and micro TEMs. The individual components of the apparatus and the principles of contactless thermal characterisation are detailed in this section.

A calorimeter was machined to the dimensions of 15 x 15 x 40 mm with a base of 30 x 30 x 5 mm using oxygen free copper (390 W/m K) obtained from Goodfellow Materials. Four 0.82 mm holes were drilled 3 mm deep at 5, 15, 25 and 35 mm from the surface into which were embedded four 0.8 mm diameter, 1.2 mm long, 5kΩ Epcos B57540G502F thermistors. Temperature measurements from the embedded thermistors were recorded using a Labview (2011) programme, shown in Appendix C. Using this temperature gradient, the heat transfer from, Q_h, and temperature of, T_h, the hot side of the TEM were determined. The upper face of the copper calorimeter was polished to a mirror finish ensuring that planarity was maintained. Polyurethane foam insulation (0.035 W/m K) was placed around the calorimeter to minimize thermal losses. The copper calorimeter was placed on top of a secondary TEM, European Thermodynamics model number ET-241-14-15, in order to hold T_h at the desired temperature via PID control. The calorimeter and secondary TEM were then mounted on a water-cooled aluminium block with water circulated at 10°C by a Lauda E100 water bath. To reduce thermal resistance at the interfaces, all interfacing surfaces were coated with a thin layer of Electrolube HTSP heat transfer compound (2.0 W/m K).

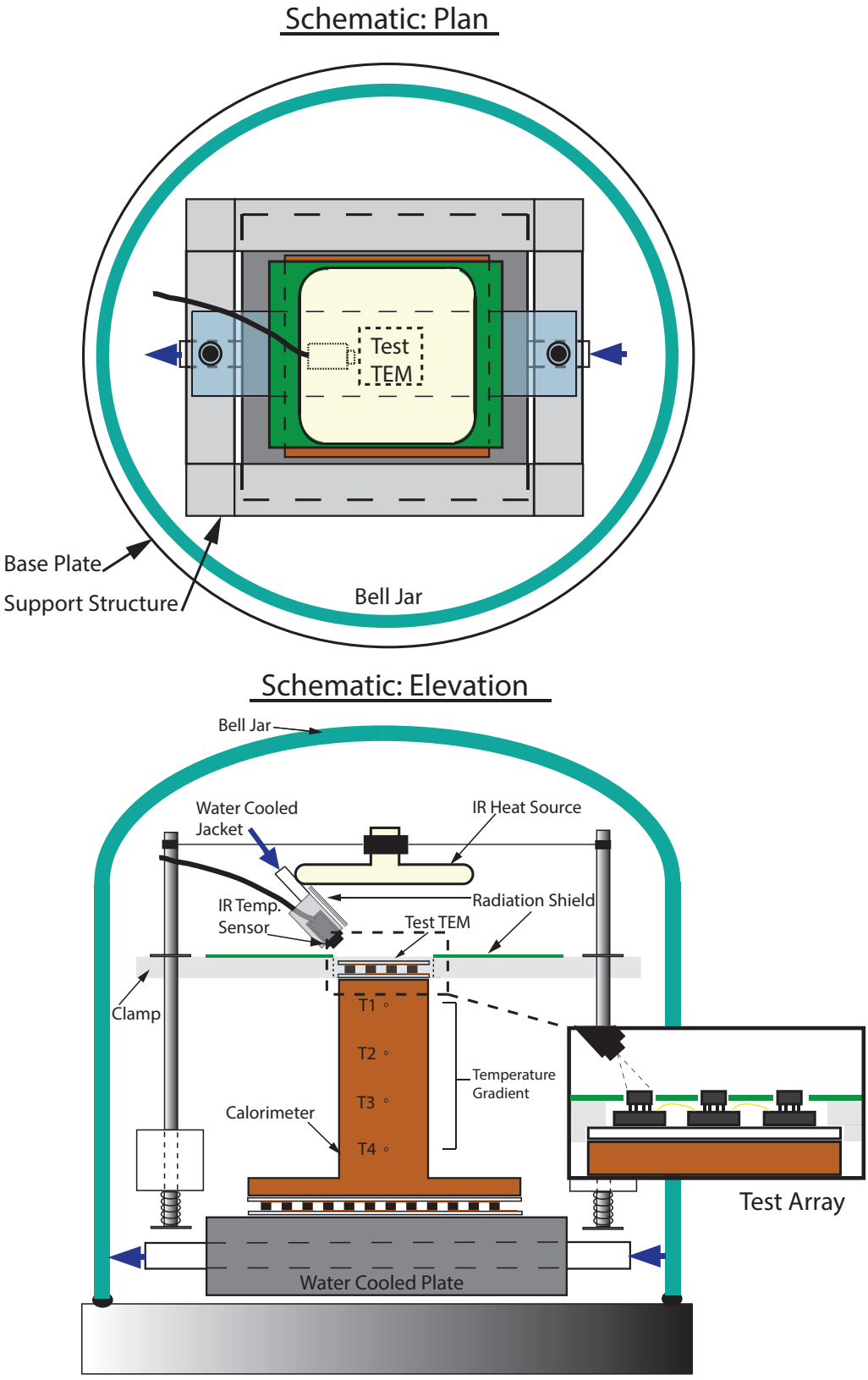

Figure 3.4: Schematic of the contactless characterisation apparatus.

Bench-marking tests were carried out using a Multicomp MCPF-031-10-25 single stage TEM, the same device used in the conventional compression method and detailed previously in section 3.1.1. The upper surface of the TEM, referred to as the cold side, was coated with an approximately 20 μm layer of Rust-oleum Painter's Touch matte black paint to increase the IR absorptivity of the ceramic surface. The test TEM was fixed in place by a spring clamping mechanism, shown in Figure 3.4. The clamp consisted of a polycarbonate sheet, 5 mm thick, machined to hold the TEM at each of the four corners, leaving a minimal area of the TEM surface in contact with the clamp and almost the entire face of the TEM exposed. The clamp was fixed to two spring loaded stainless steel rods which applied the downward force. Two steel springs, each 2.5 kN/m stiffness, applied a minimum of 50 N downwards force. This imposed a pressure of 222 kPa over the area of the test TEM in order to minimize interfacial thermal resistance.

The contactless heat source was a 125 W Ceramicx IR quarter flat ceramic heater 60 mm x 60 mm in area. The heater was fixed 45 mm above the test TEM using steel guide rods and heat resistant rubber rings in order to adjust its height. The heater was connected to a high voltage DC power supply (~250 V) with adjustable current and voltage in order to vary the temperature of the heat source and, hence, to control the heat supplied to the test TEM. Controlling the heat supply was critical to manipulating the Q_c operating point of the test TEM in order to produce characteristic thermoelectric performance curves Kraus and Bar-Cohen [7]. Low emissivity (< 0.1) aluminium foil was used to cover all exposed surfaces and wires except the upper test TEM surface, in order to reduce radiation heat transfer from the heater to the calorimeter and electrical wires within the bell jar. The cold side temperature of the test TEM, T_c, was measured by a Raytek MI3 miniature IR sensor. The sensor was fitted with a close focus lens and positioned, using a custom mounting bracket, at an angle of 51 degrees, 9 mm above the test TEM. This focused the sensor on a spot size of ~1 mm^2 on the center of the TEM cold side surface. Due to the proximity of the miniature IR sensor to the heater, it was necessary to incorporate a means of cooling the sensor head. A water-cooled aluminium jacket, shown in Figure 3.4, was placed around the sensor head. Water was circulated through the cooling jacket by the Lauda E100 water bath at a temperature of 10°C. The sensor's temperature reading was monitored and recorded

using Raytek's Data Temp Multidrop software.

Constant current was conveyed to the TEM under test using a TTi QL355TP power supply, with measurements of voltage and current taken using certified calibrated Fluke 45 and Fluke 37 multimeters respectively (calibration certificates are included in Appendix B). Voltage measurements were taken across the test device using the four wire arrangement outlined previously in the sub-section 3.1.1, minimising uncertainty attributed to resistance in the TEM leads. The experimental assembly was mounted on an aluminium base plate, 380 mm in diameter, and enclosed in a glass bell jar 320 mm in diameter and 360 mm in height. The enclosure was evacuated using a PVR PHV-5 vacuum pump to an absolute vacuum of 400 Pa, measured using Thermovac TM 101 digital piezo pressure gauge, which was the lowest achievable vacuum for this setup. The experimental setup was held under vacuum to remove moisture from the air, preventing condensation build up on the upper TEM surface at low temperatures, and to minimise convective losses. Vacuum rated water fittings were used to supply the water-cooled plate and IR sensor cooling jacket from the Lauda E100 water bath. Electrical power supply wires and sensing wires were connected across the aluminium base plate by vacuum rated electrical fittings with connectors on both sides. Vacuum losses were reduced by using a rubber sealing ring around the bottom of the bell jar and Dow Corning high vacuum silicone grease.

3.3.2 Procedure for contactless TEM characterisation

In order to measure the thermal performance of a commercially-available TEM using the contactless apparatus detailed above, the following test procedure was applied:

1. The water bath was switched on one hour in advance of each test to allow the water to cool from room temperature to the test condition of 10°C and to enable the water cooled plate and IR sensor jacket to reach steady-state.

2. The test TEM was fitted in place on the upper surface of the calorimeter with a thin layer of Electrolube HTSP heat transfer compound on the contact surface to minimize thermal resistance at the interface. The spring-loaded clamping mechanism was then applied to hold it in place.

3. The miniature IR sensor was positioned using its custom mounting bracket. Positional repeatability was ensured using physical stops to locate the bracket.

4. The IR heater was then put in place above the test TEM surface. Initially the heater remained off for the case of zero heat flow, 0 W Q_c.

5. The bell jar was then placed over the apparatus and sealed to the vacuum plate. The vacuum release valve was then closed and the vacuum pump was switched on. The chamber then took approximately 15 minutes to reach an absolute pressure of 400 Pa.

6. The test TEM was powered with a constant current set to 0.4 A. The system was allowed to reach steady-state with T_h maintained at 25°C (consistent with temperature quoted by manufacturer); on average this took between 15 to 20 minutes.

7. Electrical measurements of TEM voltage and current were then taken.

8. Cold side temperature and the temperature gradient along the calorimeter were recorded and averaged over a five minute interval.

9. Test TEM current was then raised in steps of 0.4 A as far as 2 A, allowing each step to reach steady-state. Electrical and temperature measurements were again recorded for each current step.

10. Upon collecting a full set of data for the current range, the heater power was then increased in steps of 20 W up to a maximum of 120 W. Increasing the heater power also increased the time required to reach steady-state thermally, when compared to adjusting TEM current, requiring approximately 45 minutes.

11. The procedure was repeated for each current setting until a complete set of data was obtained for all heater power settings.

Temperature and heat flow were given ample time (45 minutes) to stabilise and reach steady-state for both instances of adjusting TEM current and heater power, a time period of zero heat or temperature differential was observed before measurements were recorded.

These experimental measurements were used to compare the TEM performance characteristics provided by the manufacturer and those obtained using the conventional compression apparatus. The experimental results are presented in Chapter 4, sub-sections 4.1.2 and again in a comparison to the bench-mark conventional TEM characterisation results in sub-section 4.1.3.

3.4 Contactless characterisation of μTEMs

The novel contactless apparatus was bench-marked using a commercially-available TEM and conventional characterisation apparatus. The experimental setup was then adjusted to accommodate a μTEM array in pursuit of the objective to thermally characterise a single μTEM in a contactless fashion. The adjustments to the apparatus required are detailed in the following sub-sections as well as the procedure for the thermal characterisation of the μTEM array.

3.4.1 Apparatus

The apparatus was altered to accommodate the specially designed μTEM arrays, prepared and assembled as per sub-section 3.1.3, to obviate the compressive forces experienced in conventional TEM characterisation methods. The mechanical alterations required were confined to the method of clamping the arrays and the form of low emissivity radiation shields used to prevent radiation heat transfer to any surface other than the upper faces of the μTEMs. The clamping mechanism, shown in Figure 3.5, was similar to that used to clamp the macro-scale TEMs, but instead of holding the μTEM array at each of the four sides, it held it along the length of two edges free of electrical terminals and wires. This provided the downward force required to minimize the thermal resistance across the thermal paste layer between the array and calorimeter. The radiation shield, manufactured by UTZ Technologies and shown in Figure 3.5, was 25 mm x 25 mm and made from 100 μm thick nickel foil. The μTEM grid profile was laser cut, using a CO_2laser, with a 1 μm dimensional accuracy. The shield allowed heat from the IR heater to the cold side of the μTEMs while blocking it from the gold wire-bonding on the hot side of the devices and

ceramic base of the array. This allowed only heat pumped through the μTEMs to pass to the calorimeter below. The custom radiation shield was supplemented with aluminium foil 50 μm thick to further insulate the calorimeter and wiring from the thermal radiation of the heater.

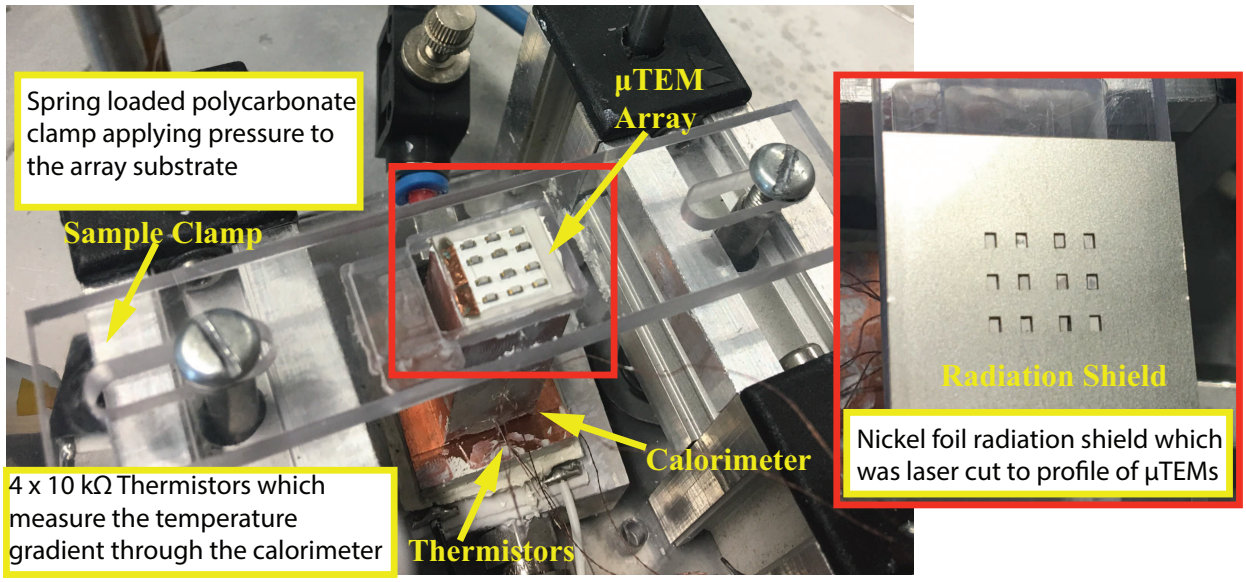

Figure 3.5: μTEM array clamping mechanism with radiation shield inset.

The assembled μTEM array was subjected to the characterisation procedure outlined in detail in the next sub-section.

3.4.2 Procedure for contactless μTEM array characterisation

The procedure to measure the thermal performance of a μTEM array using the contactless apparatus detailed above, was similar to that outlined in sub-section 3.3.2. The following adjustments were made to accommodate the μTEM array in the apparatus:

1. The miniature IR sensor focused on a spot size of 1 mm^2 on the cold side surface of a single μTEM in the central column of the array.

2. The test array was powered with a constant current set to 0.2 A. The system was allowed to reach steady-state with T_h maintained at 25°C (consistent with T_h quoted by manufacturer); on average this took between 15 to 20 minutes.

3. Test array current was then raised in steps of 0.2 A as far as 0.8 A, allowing each step to reach steady-state. Electrical and temperature measurements were again recorded for each current step.

4. All other steps remained the same as outlined in 3.3.2.

Similar to the macro TEM case in sub-section 3.3.2, temperature and heat flow were given time (45 minutes) to stabilise and reach steady-state for both instances of adjusting μTEM current and heater power, a time period of zero heat or temperature differential was observed before measurements were recorded. A data reduction and uncertainty analysis was conducted for the contactless characterisation method, and this is detailed in the following sub-section.

3.4.3 Data reduction

In this section, all the calculated variables derived from the contactless characterisation experimental data are presented, with each of their related primary measurands.

The hot side temperature, T_h, was determined using a best approximation least-squares regression fit. This took the temperature gradient from the thermistor locations and calculated the temperature at the intercept with the calorimeter surface. Heat flow through the calorimeter, Q_h, was also calculated using the temperature gradient between thermistors and, similar to T_h, was computed in real time during the test using a Labview (2011) programme. The cold side temperature was a direct measurement taken by the Raytek IR sensor. Each measured, and calculated, quantity and its uncertainty are listed in Table 3.2 as part of a robust uncertainty analysis.

Table 3.2: Uncertainty in measured quantities for contactless characterisation method.

Measured Quantities	**Uncertainty**
Thermistor temperature (T_t)	± 0.005°C
Thermistor location (x)	± 50 μm
Calorimeter area (A)	± 1.2825x10^{-6} m^2
Calorimeter thermal conductivity (k)	± 4.6%
IR sensor temperature (T_c)	± 0.5°C
TEM Current (I)	± 0.01 A for 0.3 A - 3 A
TEM Voltage (V)	± 1x10^{-4} V for 1 V - 3 V
Calculated Quantities	**Uncertainty**
Cold side heat flow (Q_c)	± 5.2%
Temperature difference (ΔT)	± 0.9°C

Many of the measured quantities listed in Table 3.2 were subjected to calibration, and various other steps in order to minimize uncertainty.

- The thermistors used were calibrated in the Lauda E100 water bath using a Fluke 1504 reference thermistor (calibration cert in Appendix B), for a temperature range of 15-40°C.

- The location of each thermistor along the length of the calorimeter was found using a digital microscope for an optical measurement, which determined the thermistor position to a resolution of 50 μm. The area of the calorimeter surface was found in a similar manner.

- Goodfellow Materials supplied the copper used in the calorimeter and the aluminium nitride used in the μTEM arrays. Goodfellow's data sheets for both materials quoted thermal conductivity values of 390 W/m K and 180 W/m K respectively. The uncertainties provided for both conductivity values were ± 5% which, in the case of the copper, was the largest single contributor to the uncertainty value for the Q_h experimental measurement and, as previously explained in section 2.3, the cold side heat flow, Q_c, is derived from Q_h. The contribution of ill defined copper thermophysical properties to experimental uncertainties has been investigated by Boudenne *et al.* [38], who used values of copper parameters available in literature to estimate an improved uncertainty of ± 4.6% in the thermal conductivity of Goodfellow copper. This

marginal improvement still resulted in the uncertainty in the thermal conductivity of the calorimeter being the largest contributing factor to the uncertainty of Q_c.[1]

- The cold side temperature measurement is a non-contact IR measurement which was rigorously calibrated *in situ* under replicated test conditions. For each increase in heater power setting, the increase in reflected radiation was accounted for in the temperature measurement of the sensor. This was achieved using a copper meter bar with its surface painted with a 20 μm layer of black paint, consistent with test TEM, with two 1.2 mm diameter, 2 mm long, Epcos B57550G502F thermistors calibrated for a temperature range of -30°C to 30°C to a certified accuracy of 0.05°C, embedded 2mm from the surface. The temperature read by the IR sensor was compared to the actual reading of the thermistors in the meter bar, for a range of emissivity values. The temperature range was established on the surface of the meter bar using the secondary TEM to raise and lower temperature. Limiting the accuracy of the IR sensor is the ± 0.5°C repeatability quoted in the device data sheet.

- Current through the test TEM, and voltage across it, were measured using the certified calibrated Fluke meters previously detailed in sub-section 3.3.1.

Knowing the accuracy of the measured values, the uncertainties for all calculated values were resolved using the Kline and McClintock method for determining uncertainty in single sample experiments [40] and included in the presentation of experimental results in Chapter 4.

[1] In an effort to reduce the uncertainty of the cold side heat pumping measurement in the contactless apparatus in this thesis, the thermal conductivity of the copper calorimeter was characterised. The approach used was to measure the diffusivity and specific heat capacity of the copper. The diffusivity was determined using the laser flash method developed by Parker *et al* [39], where a high-intensity short-duration light pulse was absorbed at the front surface of a thermally insulated specimen and the resulting temperature profile of the rear surface was measured by a thermocouple and recorded with an oscilloscope and camera. The diffusivity was then determined by the shape of the temperature versus time curve at the rear surface; a planar measurement in the specified direction of heat flow from one surface to another. The specific heat capacity of the copper was measured using differential scanning calorimetry (DSC), which measured the temperature profile as a function of time and compared it to a well defined sapphire reference. Knowing the diffusivity and the specific heat of the copper, the conductivity was determined by knowing the material density according to the relationship $k = \rho C_p D$, where k is thermal conductivity, ρ is material density, C_p is the specific heat and D is diffusivity. This approach, however, did not reduce the uncertainty of the thermal conductivity of copper due to the compound uncertainties of the laser flash method, the DSC and the density measurement.

3.5 Summary

This chapter described the experimental methods and instrumentation utilised to thermally characterise both macro-scale TEMs and μTEM arrays in a conventional compressive heat stack method and a novel contactless manner. The conventional compressive method was used to bench-mark the novel contactless apparatus developed for the purpose of thermally characterising μTEMs. A data reduction of the contactless apparatus was presented with a in-depth uncertainty analysis of all measured and calculated quantities.

In the next chapter, the results obtained from the bench-marking of the novel contactless apparatus and thermal characterisation of μTEMs are presented and discussed.

Chapter 4

Results and Discussion

This chapter presents and discusses the experimental results obtained from the conventional compression and the novel contactless characterisation apparatuses. The thermal characteristics of a macro-scale TEM are presented for both methods in section 4.1, and compared in order to bench-mark the novel contactless apparatus against the conventional compression apparatus. Following this, the results obtained for the thermal characterisation a μTEM array are presented, again for both characterisation methods. Finally, the thermal characteristics of a single μTEM are then extracted from the performance of the array and subsequently discussed.

4.1 Thermal characterisation of a macro-scale TEM

A Multicomp MCPF-031-10-25 TEM was thermally characterised using both methods previously outlined in Chapter 3, allowing the novel apparatus to be bench-marked against the conventional compression apparatus.

Subsection 4.1.1 presents the results for the thermal characterisation of the TEM using the conventional compression method. The apparatus used, which was detailed in section 3.2, represented a high precision standard in TEM characterisation. Results are presented for measurements of temperature difference across the module, ΔT, heat pumped through the module from the cold side, Q_c, and electrical current supplied, I. All thermal measurements were taken at steady-state and as per the respective procedures outlined in

Chapter 3. Sub-section 4.1.2 describes the results obtained for the TEM using the novel contactless apparatus, while sub-section 4.1.3 compares and discusses the results obtained in order to bench-mark the novel contactless apparatus against the conventional compression apparatus.

4.1.1 Conventional compression characterisation of a TEM

The data obtained from the characterisation of the Multicomp MCPF-031-10-25 TEM in the conventional compression apparatus are presented here and compared with performance data quoted by the manufacturer Multicomp in order to ascertain the difference between measured performance values (ΔT, Q_c and I) and those quoted on the device's data sheet, seen in Appendix A. The data are also analysed in order to ascertain the module level characteristics (α_M, R_M and K_M) of a macro-scale TEM using the novel characterisation apparatus.

Figure 4.1 displays a plot of ΔT as a function of Q_c for a range of values of I. Least-squares regression trend lines, generated for each data series of I, have been added to illustrate the characteristic thermoelectric behaviour as described in sub-section 2.2.2.

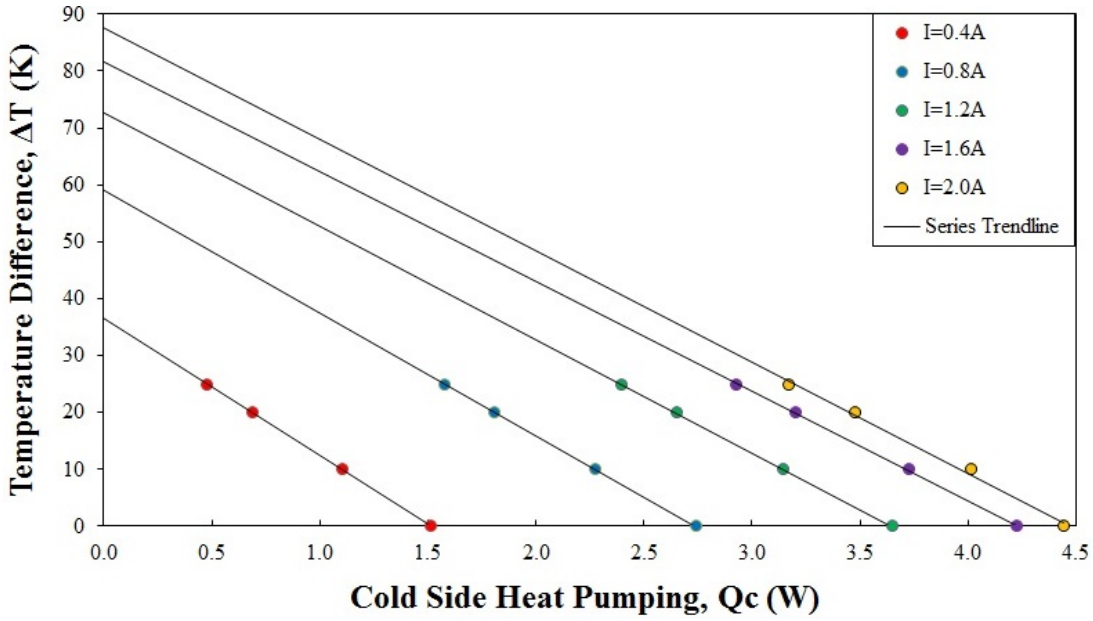

Figure 4.1: Temperature difference across the module ΔT as a function of heat pumped from the cold side Q_c, at a hot side temperature of $T_h = 45°C$ for conventional compression characterisation of the Multicomp MCPF-031-10-25 TEM. Uncertainty bars have been added for both variables but are so small as to be unnoticeable.

As outlined previously in sub-section 3.2.1, the maximum achievable ΔT across the module in the conventional compression apparatus is limited to 25 K by the lower calibration range of the thermistors, 20 – 80°C; this is evident in Figure 4.1 with the absence of data above the 25 K limit. Another notable feature of the data shown in Figure 4.1 is the goodness-of-fit, r^2, of the experimental data to the linear least squares regression trend line, tabulated in Table 4.1. The linearity of the experimental data is consistent with theoretical thermoelectric material behaviour seen in Kraus and Bar-Cohen [7]. This, coupled with the imperceptible uncertainty bars on the data points (< 0.1% ΔT and < 0.1% as per Kolodner [27]), reinforces the accuracy of the experimental setup and the efforts undertaken to minimise, and account for, stray heat in the setup such as the thermal shielding, highly reflective surfaces and evacuated test conditions outlined in section 3.2. The apparatus described is the highest available standard in literature for precision thermal measurement of TEM performance; it is against this standard that the novel contactless characterisation method was bench-marked.

Table 4.1: r^2 goodness-of-fit values for the least squares regression fit and data series seen in Figure 4.1 for the conventional compression characterisation of the Multicomp MCPF-031-10-25 TEM.

Data Series (I)	0.4 A	0.8 A	1.2 A	1.6 A	2 A
r^2	0.999983	0.999993	0.999985	0.999600	0.995000

4.1.2 Contactless characterisation of a macro-scale TEM

This section presents the data from the characterisation of the Multicomp MCPF-031-10-25 TEM in the novel contactless characterisation apparatus. The module level characteristics of the TEM are determined using the novel characterisation apparatus, described in sub-section 3.3.1, in order to compare them to those derived from the conventional characterisation method; this comparison is made in sub-section 4.1.3. The hot side temperature of the TEM, T_h, controlled by the water-cooled base plate, was set at 25°C to replicate conditions for the thermal performance characteristics quoted on the TEM data sheet by the manufacturer Multicomp. According to the data sheet, the test conditions were for T_h

maintained at 25°C over a current range of 0.4 A – 2.0 A (in steps of 0.4 A), using the four terminal material characterisation method, outlined previously in section 1.4.

The contactless characterisation data obtained for the Multicomp MCPF-031-10-25 TEM is displayed in Figure 4.2. It features a plot of ΔT versus Q_c for a range of values of I. Trend lines have been added for each data series of I to project both the x- and y-axis intercepts of maximum temperature difference, ΔT_{max}, across the module (y-axis intercept) at the condition of zero heat pumping, and the maximum heat pumping, $Q_{c\,max}$, at the condition of zero temperature difference across the module (x-axis intercept).

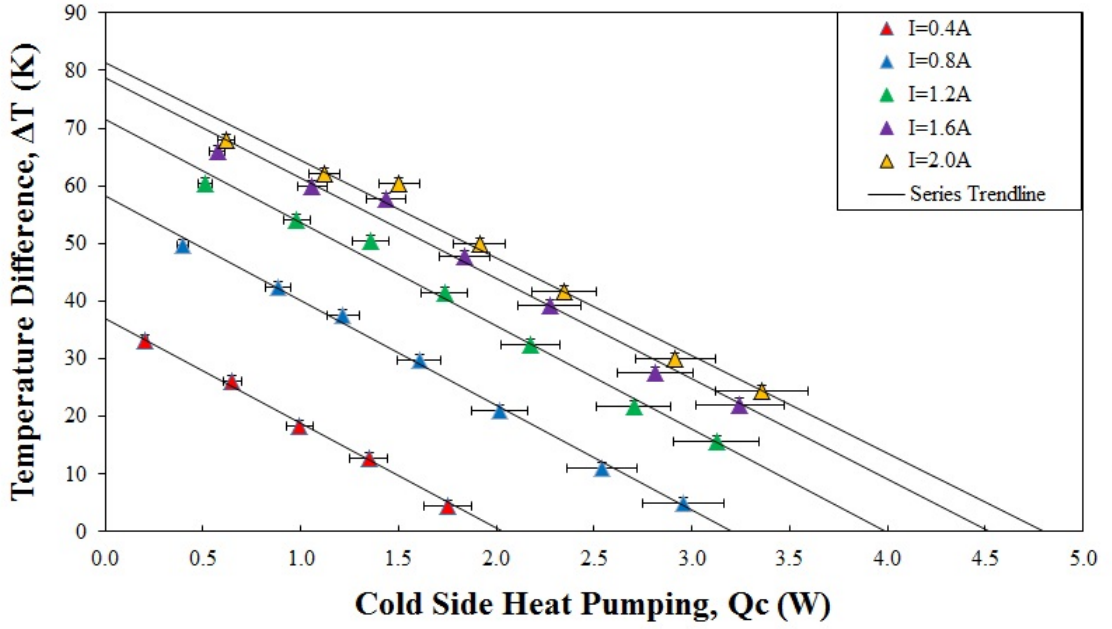

Figure 4.2: Temperature difference across the module ΔT as a function of heat pumped from the cold side Q_c. Data was recorded at a hot side temperature of T_h = 25°C for contactless characterisation of the Multicomp MCPF-031-10-25 TEM and then normalised for a hot side temperature of T_h = 45°C as per Section 2.4.

It is again evident from the trend lines in Figure 4.2 that the contactless characterisation data significantly behaves as per the theory outlined in Kraus and Bar-Cohen [7]. r^2 values for the trend lines, tabulated in Table 4.2, show good fits to the data and lend confidence to the theoretical thermoelectric behaviour illustrated. However, the r^2 values for the contactless apparatus data trend lines are lower than those for the corresponding trend lines for the conventional apparatus; this is postulated to be the result of a combination of inferior thermal shielding (in comparison with the conventional apparatus) and greater uncertainty

in Q_c, 5.2% for the contactless method, as shown in sub-section 3.4.3, compared with < 0.1% for the conventional characterisation method. These causes of inferior r^2 values for the contactless characterisation data set are expanded upon in the following sub-section, where the two methods are compared for the case of the thermal characterisation of the macro-scale TEM.

Table 4.2: r^2 goodness-of-fit values for the least squares regression fit and data series seen in Figure 4.2 for the conventional compression characterisation of Multicomp MCPF-031-10-25 TEM.

Data Series (I)	0.4 A	0.8 A	1.2 A	1.6 A	2 A
r^2	0.9980	0.9960	0.9897	0.9828	0.9796

4.1.3 Comparison of methods for the macro-scale TEM case

This section compares the thermal characterisation results obtained from both the conventional compression and the novel contactless apparatuses for the Multicomp MCPF-031-10-25 TEM. By comparing the results across the apparatuses for the same TEM, a bench-marking standard can be established for the novel contactless apparatus to provide confidence in the method. The experimental data of TEM performance (ΔT, Q_c and I) obtained for both characterisation apparatuses is compared graphically in Figure 4.3. In addition, the fundamental TEM characteristics (α_M, R_M and K_M) are determined using the 3D curve fitting methodology outlined in section 2.5 and presented in Table 4.3 at the end of this sub-section.

Using the data from the conventional characterisation method as a bench-mark, with the trend lines for the data set included for visual comparison, it is evident in Figure 4.3 that the data obtained from the contactless apparatus is in moderate overall agreement for the Multicomp MCPF-031-10-25 TEM (Q_c within 15-357 mW (1 – 25.5%) and values for ΔT within 0.4 – 6.2 K (0.5 – 7.6%)).

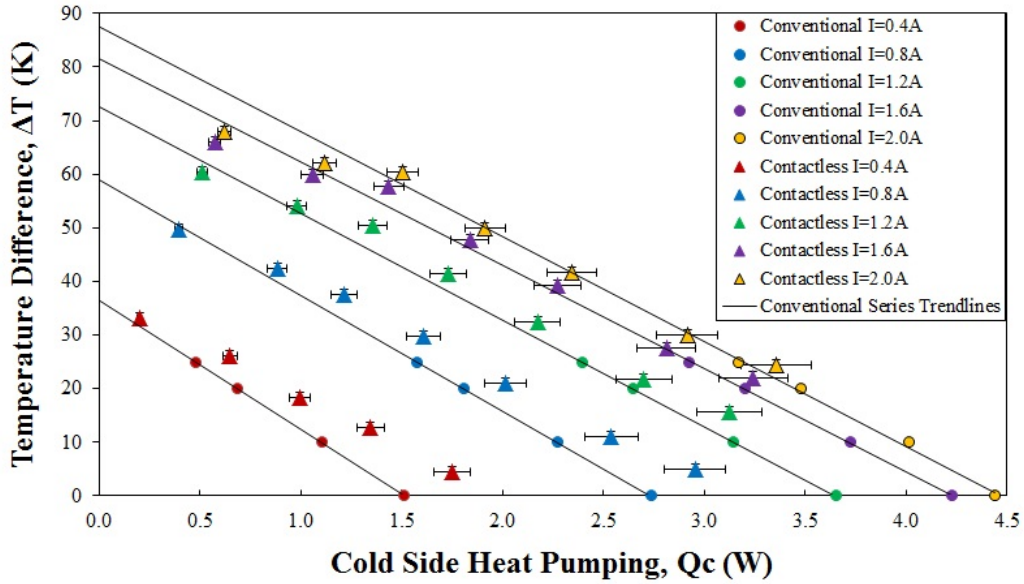

Figure 4.3: Combined plot of ΔT as a function of Q_c for conventional and contactless characterisation of the Multicomp MCPF-031-10-25 TEM normalised for a hot side temperature of T_h = 45°C as per section 2.6, with trend lines for the conventional compression data providing a bench-mark for comparison.

The largest discrepancy between the methods occurs for higher values of Q_c for each I series and for the lower range of ΔT (below $\Delta T = 20\ K$). The largest differences in Q_c in the this range varies from 196 mW to 357 mW (6.7 – 25.5%) across all values of current. It is hypothesised that the discrepancy between the data sets occurs for two main reasons:

- Within the evacuated bell jar in the contactless method, it is evident that the reflected radiation from the large surface area of the IR heat source is not shielded as rigorously as the bench-mark (the conventional method). This reflected radiation increases with heater power as objects within the bell jar, including the surfaces of the bell jar itself, absorb the radiated heat from the IR source and increase their own emitted radiation. This phenomenon is illustrated in Figure 4.4.

- As per Stafford *et al.* [41], natural convection in a vacuum contributes approximately 4% in an absolute pressure in the order of 10^2 Pa. While this factor is small, it is postulated to be a contributor to the overall discrepancy between the data from both characterisation methods.

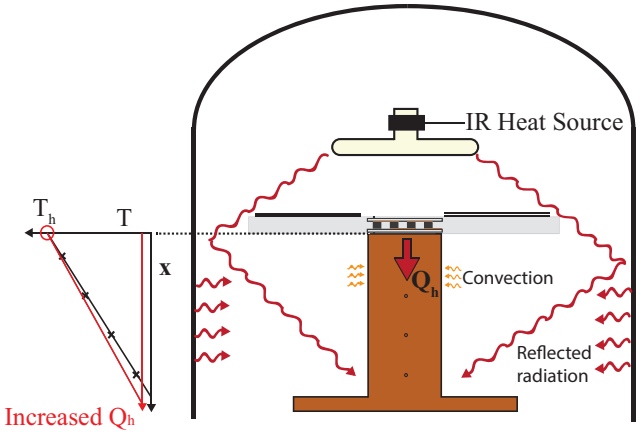

Figure 4.4: Reflected radiation hypothesis for the contactless characterisation apparatus showing the heat source and calorimeter, as illustrated in Figure 2.5, section 2.3.

The other observed difference between both data sets is the deviation of the ΔT measurement in the contactless method above the threshold of $\Delta T = 60\ K$:

- The possible reason for this is that the cold side temperature measurement above the threshold is -35°C, which is slightly outside the calibration limit (-30°C to 30°C, as stated in sub-section 3.4.3) of the IR temperature sensor.

Further comparison of the the characterisation methods is presented in Figure 4.5 and Figure 4.6 in which the maxima of ΔT and Q_c are plotted as a function of I through the TEM.

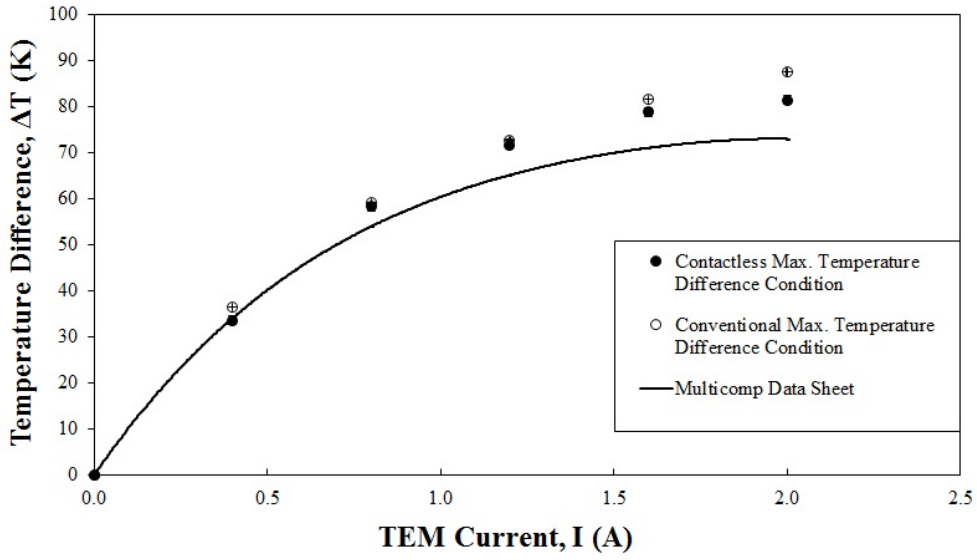

Figure 4.5: Combined plot of ΔT_{max} as a function of I at $Q_c = 0$ for conventional and contactless characterisation of the Multicomp MCPF-031-10-25 TEM.

The data points were obtained from the global curve fits, outlined previously in section 2.5, applied to the experimental data for both characterisation methods. The maxima for ΔT and Q_c occur at the intersection of the curve fit with the opposing axis (ie. ΔT_{max} at $Q_c = 0$ and *vice versa*).

In Figure 4.5, there is close agreement (within 1.6 K, 4.3% on average) between both methods for values of $\Delta T < 70K$ however, above this threshold, the discrepancy increases to 6.3 K, or 7.6%, at the maximum value of I, with the value for ΔT in the contactless method measuring lower than the conventional compression method. This is consistent with Figure 4.3, in which it is evident that below the lower limits of the temperature calibration range, the cold side temperature measurement, T_c, is inconsistent with the values measured in the conventional method.

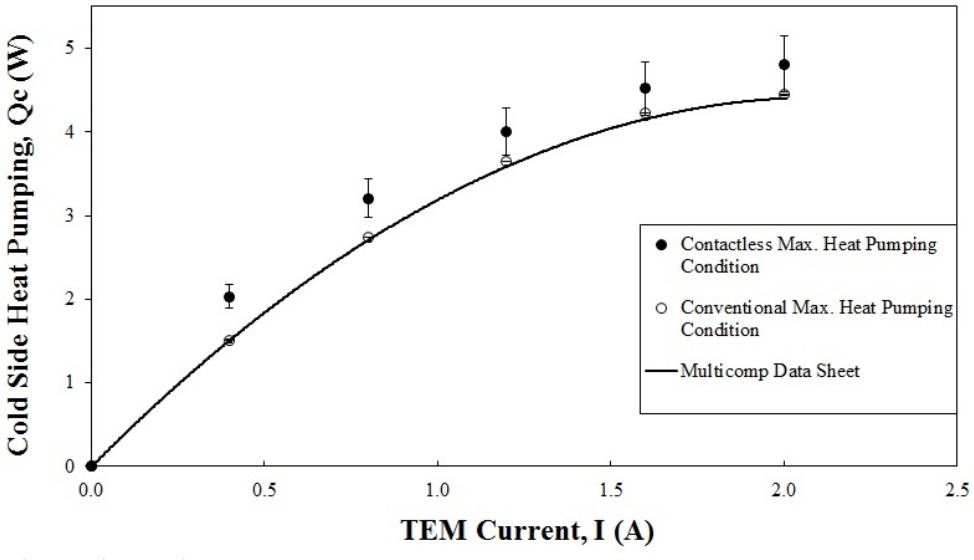

Figure 4.6: Combined plot of $Q_{c\,max}$ as a function of I at $\Delta T = 0$ for conventional and contactless characterisation of the Multicomp MCPF-031-10-25 TEM normalised for a hot side temperature of $T_h = 45°C$ as per section 2.6.

In Figure 4.6, the values for maximum heat pumping for the contactless method are consistently greater than those for the conventional bench-marking method (on average 399 mW, 14.1%); this supports what is seen in Figure 4.3, where Q_c values are consistently higher, 15 – 357 mW (1 – 25.5%), in the contactless characterisation data. This suggests the presence of stray heat gained by the calorimeter which is hypothesised to be due to reflected radiation from the IR heater and convection heat transfer from the heated air in

the bell-jar.

To develop the comparison of both methods further and to put a quantitative understanding on the experimental data set, Table 4.3 below shows the performance maxima for the TEM characterised using both methods. Also presented are the fundamental thermoelectric characteristics of the TEM obtained from applying the governing equation 2.11 to the experimental data set as outlined in section 2.5. Comparing thermoelectric characteristics across both methods provides a common reference for the two methodologies.

From Table 4.3, the contactless characterisation method compares moderately well with the conventional bench-mark method on the thermoelectric characteristics α_M, R_M and K_M. The differences are +13.5% (0.0015 V/K), +23.8% (0.264 Ω) and +19.9% (0.0056 W/K) respectively. The contactless method measures higher in all three characteristics but it produces a lower dimensionless figure of merit, ZT, value by 18%. The ZT value, as outlined in sub-section 2.2.2, is a common dimensionless metric used to express TEM performance. It is a ratio of the thermoelectric properties, α_M, of the TEM and the the loss mechanisms inhibiting thermoelectric heat pumping, R_M and K_M. While the contactless method indicates a higher α_M (which is good for heat pumping in the TEM), it also has higher loss mechanisms in the form of higher R_M and K_M. Due to these higher values in the contactless TEM characterisation relative to the conventional method, the latter method shows a superior ZT for the Multicomp MCPF-031-10-25 TEM.

Table 4.3: Module level parameters and performance maxima for Multicomp MCPF-031-10-25 TEM.

	ΔT_{max} (K)	$Q_{c\,max}$ (W)	I_{max} (A)	α_M (V/K)	R_M (Ω)	K_M (W/K)	ZT (T_h = 318 K) -
Conventional	87.5	4.45	2.0	0.0111	1.1061	0.0281	1.260
Contactless	81.3	4.80	2.0	0.0126	1.3702	0.0337	1.025
Manufacturer	74.0	4.40	2.0	0.0113	1.2016	0.0358	0.885

Having bench-marked the novel contactless characterisation apparatus against a high precision conventional compression method, an array of μTEMs was then thermally characterised using both methods. The results and comparison of the two methods is presented in the following section.

4.2 Thermal characterisation of the μTEM array

A 4 x 3 array of Micropelt D303 μTEMs was thermally characterised using both the novel contactless method and the conventional compression method. In this section, results are presented for measurements of ΔT, Q_c and I. All thermal and electrical measurements were taken at steady-state and in accordance with the respective procedures outlined in sub-sections 3.2.3 and 3.4.2.

The following sub-section presents the characterisation results for both methods on the μTEM array and compares the performance characteristics (ΔT, Q_c and I) and fundamental thermoelectric characteristics (α_M, R_M and K_M) obtained. The characteristics of a single μTEM are then isolated from the array data and presented in sub-section 4.2.2.

4.2.1 Comparison of methods for characterisation of the μTEM array

This sub-section compares the thermal characterisation results obtained from both the conventional compression and the novel contactless apparatuses for the μTEM array. As previously outlined in sub-section 3.1.3, the differences in characterisation methods necessitated two different μTEM array configurations. Initially, the experimental data of μTEM array performance obtained for both characterisation apparatuses is compared without adjustment in Figure 4.7. The thermal resistances of each of the array materials are then outlined and accounted for in the data from both characterisation methods, with the adjusted data presented and compared in Figure 4.9. In addition, the fundamental thermoelectric characteristics are determined from the adjusted data using the 3D curve fitting methodology outlined in section 2.5 and presented in Table 4.5 at the end of the sub-section.The comparison presented in Figure 4.7 shows a large discrepancy between the conventional and contactless characterisation methods. A difference of up to 0.35 mW (60 %) is seen in Q_c and up to 4 K (80 %) for ΔT. The discrepancies illustrated highlight the differences in μTEM array between the two methodologies.

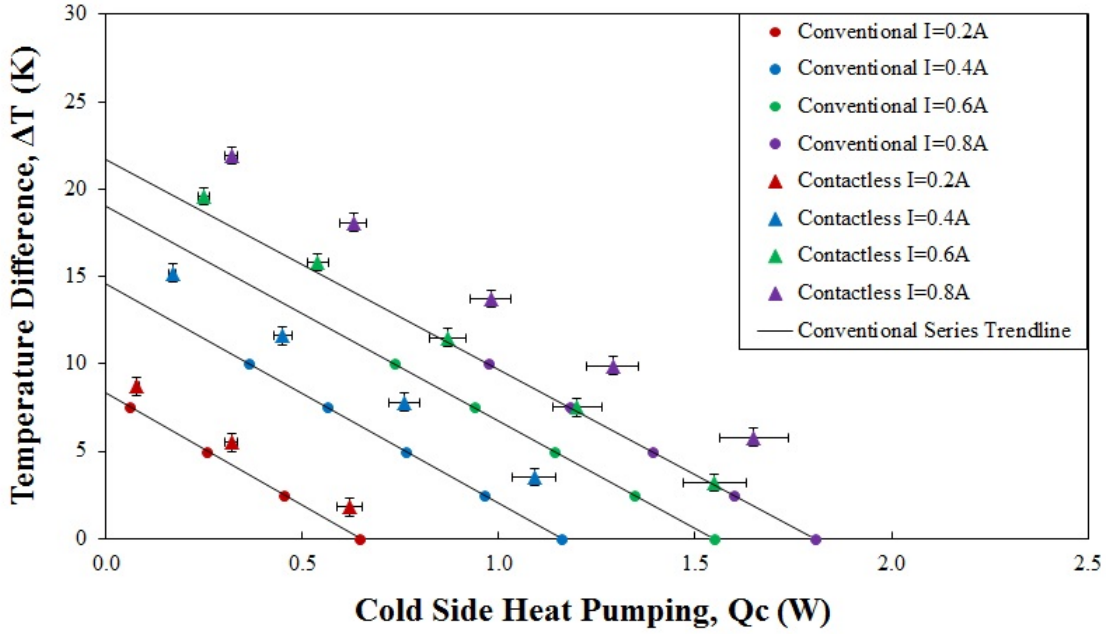

Figure 4.7: Combined plot of ΔT as a function of Q_c for conventional and contactless characterisation of the 4 x 3 MPC D303 μTEM array normalised for a hot side temperature of T_h = 45°C as per section 2.6, with trend lines for the conventional compression data providing a bench-mark for comparison.

For the purpose of reliable heat flow measurement, both methodologies required the assembly of an array of μTEMs on an AlN substrate. Additionally for the conventional characterisation method, due to the application of the heat load on the cold side via a heater block, it was necessary to apply an AlN superstrate to uniformly spread the heat across the upper surfaces of the μTEMs. This required mechanical reinforcement in the form of an epoxy support structure between the AlN substrate and superstrate to prevent the compressive forces applied in the conventional apparatus from damaging the μTEMs. With these additional layers of thermal resistance in place, the true value of temperature difference, ΔT^*, for both arrays and the true cold side heat flow, Q_c^*, for the conventional array required the calculation of the respective thermal resistances in order to correct the measured experimental data. Both arrays and the associated thermal resistances are illustrated in Figure 4.8. The thermal resistance was calculated for the epoxy support, R_e, as well as the resistances of the AlN substrate and superstrate, R_{AlN}, the upper silicone layer between the superstrate and the μTEM, R_{su}, and the lower silicone layer between the μTEM base and the substrate, R_{sl}. It is assumed that the spreading resistance in the AlN substrate and

superstrate is negligible due to the high thermal conductivity of the ceramic material (~180 W/m K).

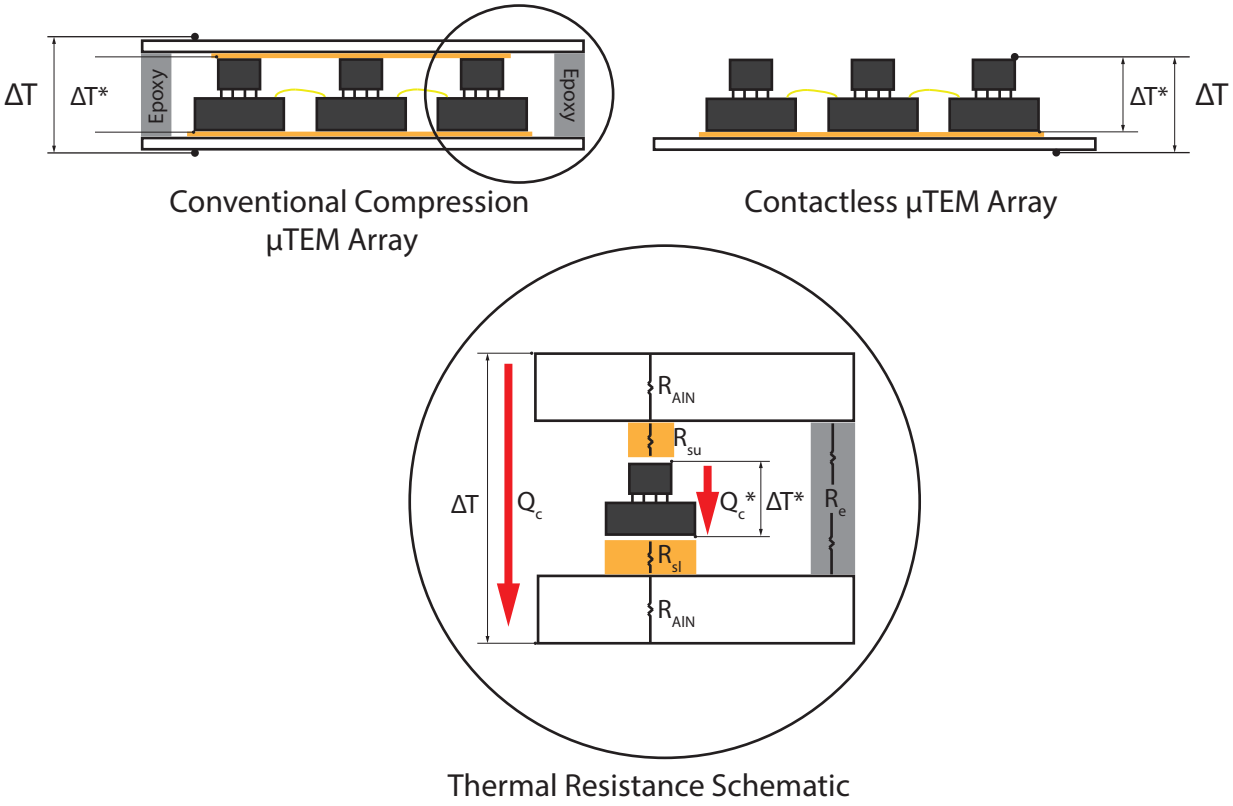

Figure 4.8: Comparison of μTEM arrays used in the conventional and contactless characterisation methods respectively. Inset: thermal resistance schematic of μTEM array.

R_e, R_{AlN}, R_{su} and R_{sl} were calculated using Equation 4.1, found in Holman [42], and are presented in Table 4.4. The thermal resistances are expressed as a ratio of the thermal conductivity, k, divided by the product of the thickness, h, and area, A, of the respective material layers:

$$R = \frac{h}{kA} \tag{4.1}$$

. The "true" heat flow through the conventional μTEM array, Q_c*, was calculated by accounting for heat leaked through the epoxy support structure, R_e, proportional to the temperature difference measured across the array, ΔT:

$$Q_c^* = Q_c + \frac{\Delta T}{R_e} \tag{4.2}$$

Table 4.4: Material thicknesses and thermal resistances for μTEM array.

	Material Thickness (m)	Area (m^2)	Thermal Conductivity (W/m K)	Thermal Resistance (K/W)
AlN Substrate/Superstrate (R_{AlN})	0.60 x 10^{-3}	225 x 10^{-6}	180.00	0.01
Electrolube TCOR RTV silicone superstrate (R_{su})	0.05 x 10^{-3}	1.2 x 10^{-6}	2.00	1.73
Electrolube TCOR RTV silicone substrate (R_{sl})	0.05 x 10^{-3}	2.2 x 10^{-6}	2.00	0.95
3M Scotch Weld DP 190 epoxy (R_e)	1.35 x 10^{-3}	56 x 10^{-6}	0.38	63.30

Once the resistances and true heat flow were known, the true temperature difference, ΔT*, was calculated by adding the product of the cold and hot side heat flows, Q_c* and Q_h, and their respective thermal resistances, R_{AlN}, R_{su} and R_{sl}, to the measured temperature ΔT:

$$\Delta T* = \Delta T + Q_h (R_{sl} + R_{AlN}) + Q_c * (R_{su} + R_{AlN}) \tag{4.3}$$

In the case of the contactless μTEM array, only Q_h, R_{sl} and R_{AlN} for the substrate were considered in the absence of an AlN superstrate. With the thermal resistance values seen in Table 4.4, Equations 4.2 and 4.3 were applied to the experimental data to adjust for the associated losses.

Figure 4.9 shows the adjusted experimental data to reflect the true temperature difference and heat flow through the μTEMs in both the conventional compression and novel contactless characterisation methods. With the data adjusted for the thermal resistance layers of the μTEM arrays, a comparison of both characterisation methods was made. Using the data from the conventional characterisation method as a bench-mark, with the trend lines for the data set included for visual comparison, it is evident in Figure 4.9 that the data obtained from the contactless apparatus is in good overall agreement for the μTEM array (Q_c within 15-100 mW (2.5 – 15%) and values for ΔT within 0.5-1.9 K (1.5 – 6.5%)). This is an improvement on the comparison of the macro-scale TEM bench-marking in subsection 4.1.3.

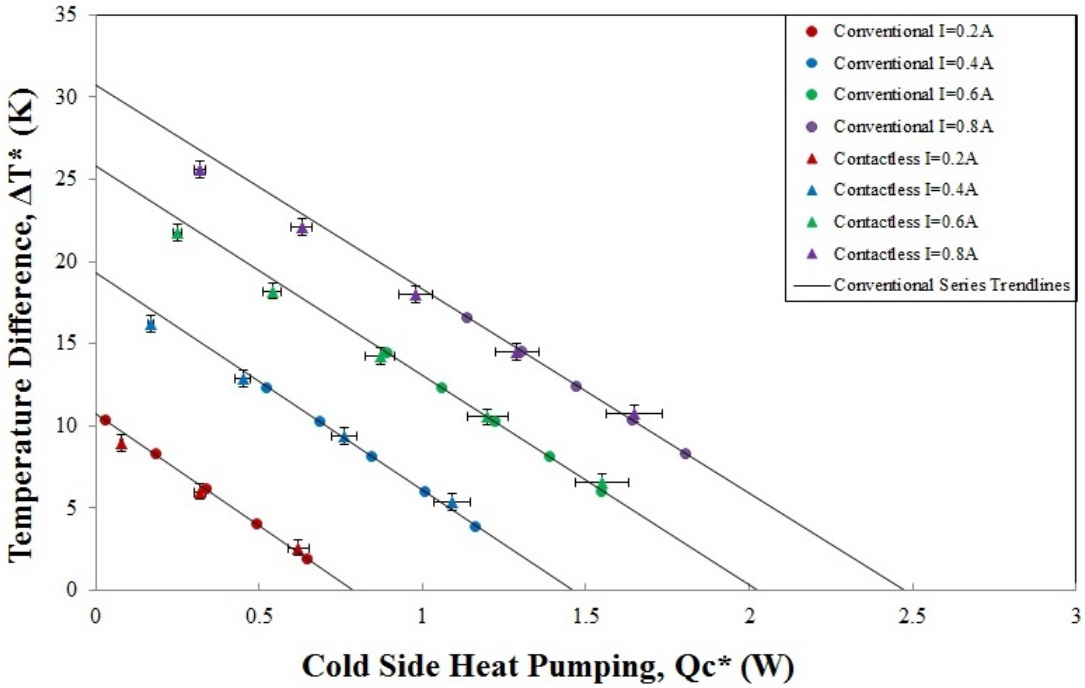

Figure 4.9: Combined plot, adjusted for thermal interface resistances, of ΔT as a function of Q_c for conventional and contactless characterisation of the 4 x 3 MPC D303 μTEM array normalised for a hot side temperature of T_h = 45°C as per section 2.6, with trend lines for the conventional compression data providing a bench-mark for comparison.

One reason for the improved agreement is the lower heater power required from the IR heat source to produce the data set in the contactless method due to the decreased heat pumping capacity of the μTEMs compared to the macro-scale TEM (80 W maximum heater power in comparison with 120 W). As previously outlined in sub-section 4.1.3, radiative stray heat within the contactless set up is believed to be a significant factor in the divergence of data at higher values of Q_c. In the case of the μTEM arrays, the compensation for the thermal resistance of the various layers means a lack of data values for higher Q_c. However, the 3D surface fit, outlined in section 2.5, again projects the discrepancies between the methods occurring for higher values of Q_c for each I series and for the lower range of ΔT (below $\Delta T = 5\ K$). The largest differences in Q_c in this range vary from 70 mW to 100 mW (4.2 – 15%) across all values of current.

Table 4.5 presents the performance and module level characteristics of the μTEM array from both characterisation methods as well as from the manufacturer Micropelt. It is evident that the contactless characterisation method compares reasonably well with both

the conventional bench-mark method and Micropelt's data sheet on the thermoelectric characteristics α_M, R_M and K_M. The differences are +4.2% (0.0006 V/K), +2.9% (0.08 Ω) and +11.4% (0.008 W/K) compared to the conventional compression method, and +5.7% (0.0008 V/K), -9.3% (0.29 Ω) and +15.8% (0.0106 W/K) compared to Micropelt's data. The contactless method records higher for α_M, K_M and R_M but yields a lower overall value for ZT (-5.2%) in comparison to the conventional compression method, while it measures higher for α_M and K_M but lower for R_M yielding a higher overall value for ZT (+6.1%) in comparison to the manufacturer Micropelt.

Table 4.5: Module level parameters and performance maxima for MPC D303 μTEM array.

	ΔT_{max} (K)	$Q_{c\,max}$ (W)	I_{max} (A)	α_M (V/K)	R_M (Ω)	K_M (W/K)	ZT (T_h = 318 K) -
Conventional	36.5	3.12	1.2	0.0141	2.75	0.06984	0.308
Contactless	34.1	3.25	1.2	0.0147	2.83	0.07782	0.292
Manufacturer	36	3.08	1.2	0.0139	3.12	0.06720	0.275

Further comparison of the the characterisation methods for the μTEM array case is presented in Figure 4.10 and Figure 4.11, in which the maxima of ΔT and Q_c, respectively, are plotted as a function of I through the TEM. The data points are obtained from the global curve fits, outlined previously in section 2.5, applied to the experimental data for both characterisation methods.

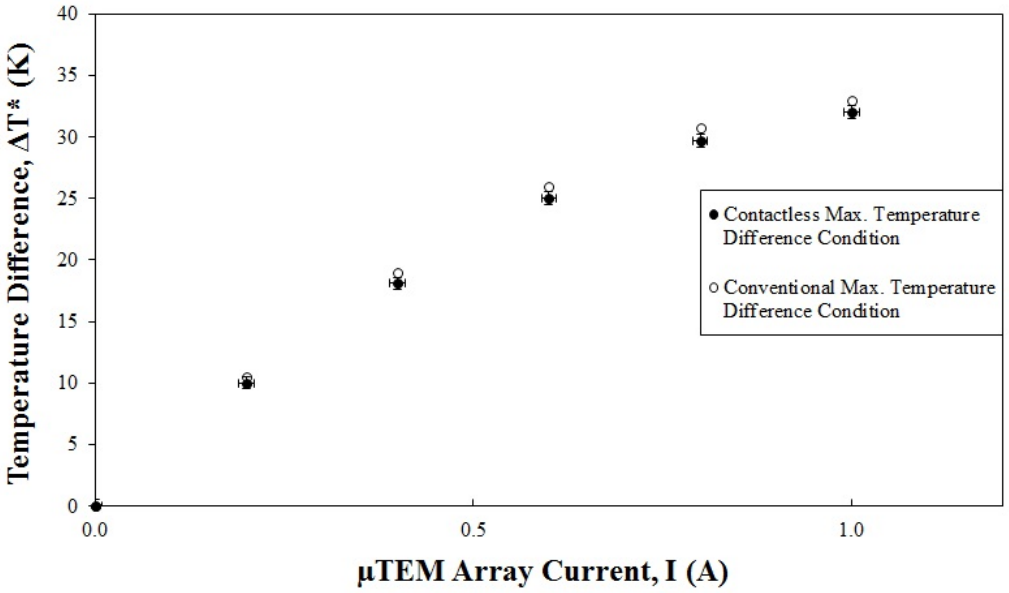

Figure 4.10: Combined plot of ΔT as a function of I for conventional and contactless characterisation of 4x3 MPC D303 μTEM array normalised for a hot side temperature of T_h = 45°C as per section 2.6.

In Figure 4.10, there is close agreement (within 1 K, 3.5% on average) between both methods with the contactless data consistently lower. This is consistent with the data in Figure 4.7.

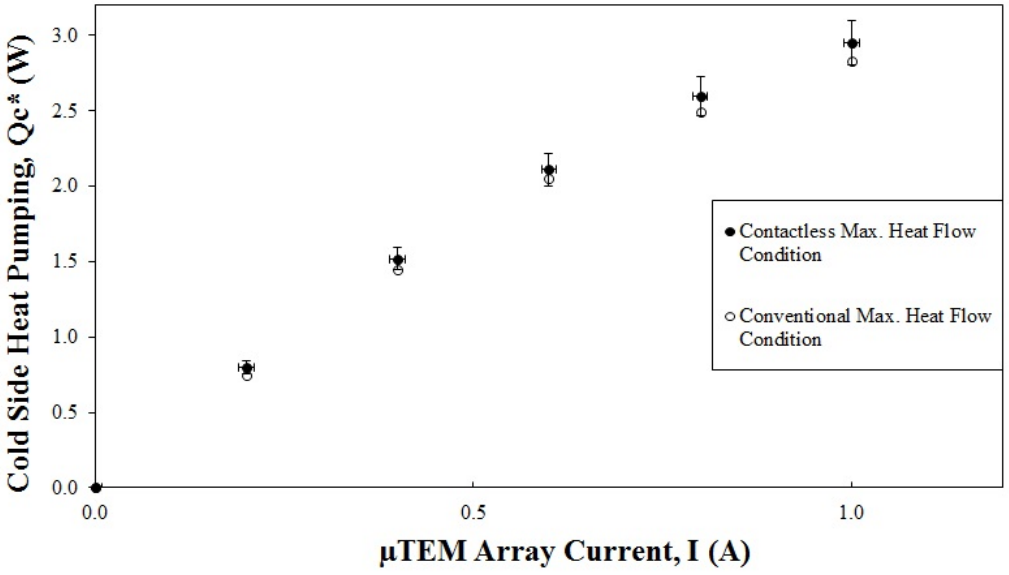

Figure 4.11: Combined plot of $Q_c$as a function of I for conventional and contactless characterisation of 4x3 MPC D303 μTEM array normalised for a hot side temperature of T_h = 45°C as per section 2.6.

In Figure 4.11, the values for maximum heat pumping for the contactless method are consistently greater than those for the conventional bench-marking method (on average 80 mW, 5.2%); this is consistent to what is seen in Figure 4.7, where Q_c values are consistently higher, 15-100 mW (2.5 – 15%), for the contactless characterisation data.

Having presented the characterisation results for the array of μTEMs, the next sub-section isolates the performance of a single μTEM from the composite array and presents the resulting thermoelectric and performance characteristics.

4.2.2 Single μTEM performance data

The ultimate objective of characterising a μTEM array was to obtain the thermal characteristics of a single μTEM. Isolating the performance of a single μTEM from that of the array required three steps:

- At the array level, the thermal resistance contributed by the substrate materials as well as the thermal grease and bonding agents was calculated and accounted for as described in sub-section 4.2.1. The true value for temperature difference across the μTEM array, ΔT^*, and the true heat pumped through it, Q_c^*, was determined from the corrected data. As outlined previously in sub-section 4.2.1, however, for the contactless array $Q_c^* = Q_c$ due to the absence of a superstrate and epoxy support structure.

- To determine ΔT^* for a single μTEM, the temperature difference across the array was assumed equal across each individual μTEM.

- In order to isolate Q_c^* for a single μTEM the heat pumped through the array was assumed equal through each device in the array. The heat pumped was then divided by the number of devices (12) to arrive at Q_c^* for a single μTEM.

Having isolated the performance of a single μTEM from the array, and accounted for the thermal resistance losses associated with the heat spreader and thermal interface materials, the values for ΔT^* and Q_c^* were calculated and mapped to a 3D curve fit using the Matlab Curve Fitting Toolbox as per 2.5. The results for thermal performance characteristics and

module level characteristics of a single μTEM were determined and are presented in Table 4.6.

Table 4.6: Module level parameters and performance maxima for a single Micropelt MPC D303.

	ΔT_{max} (K)	$Q_{c\ max}$ (W)	I_{max} (A)	α_M (V/K)	R_M (Ω)	K_M (W/K)	ZT (T_h = 318 K) -
Conventional	36.5	0.260	1.2	0.00118	0.229	0.00582	0.308
Contactless	34.1	0.271	1.2	0.00123	0.236	0.00648	0.292
Manufacturer	36.0	0.257	1.2	0.00116	0.260	0.00560	0.275

Due to the removal of the contributions of the array substrates and interface materials in 4.2.1, the values determined for a single μTEM from the 3D curve fit compare identically between the characterisation methods and manufacturer's data as seen in Table 4.5. Notable comparisons for the performance characteristics of the single μTEM are the value for $Q_{c\ max}$ being within 5% of both the manufacturer and the conventional compression method, with ΔT_{max} being within 6.5% of both.

4.3 Summary

This chapter describes the results obtained from the thermal characterisation of a macro-scale TEM and a μTEM array using a conventional compression apparatus and a novel contactless apparatus. These results are discussed in the context of bench-marking the novel contactless apparatus against the conventional compression characterisation in the macro-scale TEM case, while then comparing the results obtained for the characterisation of the μTEM array. The ultimate objective to quantify the performance and thermoelectric characteristics of a single μTEM is determined by accounting for the contributions of thermal resistances in the μTEM array materials and calculating the "true" values of ΔT^* and Q_c^* for a single device.

In the next chapter, the conclusions drawn from the discussion on experimental results are presented and recommendations are made for future work on the thermal characterisation of μTEMs.

Chapter 5

Conclusions and Recommendations

5.1 Conclusions

In this thesis a novel contactless thermoelectric characterisation method has been designed, commissioned and used to characterise an array of μTEMs. From this, the thermoelectric and performance characteristics for a single μTEM were derived. The contactless apparatus utilised an infra-red heat source and temperature sensor to obviate potentially damaging stresses from the upper surface of the μTEMs. The contactless method was bench-marked against a high precision steady-state apparatus, which utilised a conventional compression characterisation methodology, using a macro-scale Multicomp MCPF-031-10-25 TEM. Both methods were then used to characterise a μTEM array and the results were compared; in the case of the conventional compression characterisation, the μTEM array was designed to accommodate the compressive load applied without damaging the micro-scale devices. This chapter distills conclusions from the results presented in Chapter 4 and recommends steps for future work on contactless characterisation of μTEMs.

5.1.1 Bench-marking the for the macro-scale TEM case

- There is moderate overall agreement between the contactless characterisation method and the convention compression method for the Multicomp MCPF-031-10-25 TEM (Q_c within 15 – 357 mW (1 – 25.5%) and values for ΔT within 0.4 – 6.2 K (0.5 – 7.6%)).

- The largest discrepancy between the contactless and conventional compression methods occurs for higher values of Q_c for each I series and for the lower range of ΔT (below $\Delta T = 20\ K$). The largest differences in Q_c in the this range vary from 196 mW to 357 mW (6.7 – 25.5%) across all values of current. It is hypothesised that the discrepancy between the data sets occurs for two main reasons:

    1. Within the evacuated bell jar in the contactless method, reflected radiation from the large surface area of the IR heat source is not shielded as rigorously as the bench-mark (the conventional method). This reflected radiation, received in part by the apparatus' calorimeter, increases with heater power and manifests itself in the increasing discrepancy between the methods as Q_c increases.

    2. The other observed difference between both data sets is the deviation of the ΔT measurement in the contactless method above the threshold of $\Delta T = 60\ K$. The reason for this is that the cold side temperature measurement above the threshold is -35°C, which is outside the calibration limit (-30°C to 30°C) of the IR temperature sensor. This issue does not affect the characterisation of μTEMs as the temperatures measured in that instance were within the calibration range.

5.1.2 Characterisation of μTEM array

- Once the contributions of the thermal interfaces present in the μTEM array preparation were identified and accounted for, there was good agreement between both characterisation methods for the μTEM array performance and thermoelectric characteristics. Q_c measured within 15 – 100 mW (2.5 – 15%) and values for ΔT were within 0.5 – 1.9 K (1.5 – 6.5%). The improved agreement is due to the smaller heat pumping loads of the μTEM array compared to the macro-scale case, resulting in smaller discrepancies at higher Q_c for the μTEMs.

- The contactless characterisation method compared reasonably well with both the conventional bench-mark method and Micropelt's data sheet on the thermoelectric characteristics α_M, R_M and K_M. Values for α_M are within +5.7% (0.0006 V/K) of both, values for R_M within +9.3% (0.29 Ω) and values for K_M within +15.8% (0.0106

W/K). The contactless method yields an overall value for ZT within ± 6.1% in comparison to the conventional compression method and the manufacturer Micropelt.

5.1.3 Single μTEM performance data

- The performance characteristics of a single μTEM were determined using the novel contactless characterisation method, developed as part of this thesis, and the following values were achieved: ΔT_{max} = 34.1 K, $Q_{c\ max}$ = 0.271 W and I_{max} = 1.2 A. The values compare well with the conventional compression characterisation method and the manufacturer's data supplied by Micropelt; the contactless method's value for $Q_{c\ max}$ was within 5% of both, with ΔT_{max} within 6.5%.

- The thermoelectric figure of merit ZT (0.292) determined using the contactless method, calculated from α_M (0.0147 V/K), K_M (0.07782 W/K) and R_M (2.83 Ω), is within ± 6.1% of both the conventional compression method (0.308) and the manufacturer (0.275).

5.2 Recommendations

- To minimise the discrepancies observed between the contactless method and the conventional compression bench-mark at higher values of Q_c, it would be necessary to improve the thermal shielding around calorimeter of the contactless apparatus to minimise reflected radiation heat transfer. This could be achieved by using a highly reflective guard structure around the calorimeter to minimise radiation heat transfer from the surrounding surfaces.

- The evacuated bell-jar test environment could be improved in the contactless apparatus. The bench-mark conventional apparatus used a diffusion vacuum pump to establish an absolute vacuum of 0.002 Pa, compared to an absolute vacuum of 400 Pa in the contactless apparatus. It is clear that improved vacuum seals and a better pump could reduce the heat losses caused by convective heat transfer.

- To further minimise stray heat in the contactless apparatus, a more focused infra-red heater could be used as a cold side heat source. IR lasers hold potential to focus the heat load on the surface of the μTEMs using optics. This would reduce the reflected radiation seen for the 60 mm x 60 mm ceramic heater used for this thesis. IR lasers were investigated for the purposes of this thesis but budgetary constraints prevented further exploration.

References

[1] Jeremy Bernstein. *Three degrees above zero: Bell Laboratories in the information age*. CUP Archive, 1987. 1.1

[2] Bishnu P Pal. *Fundamentals of fibre optics in telecommunication and sensor systems*. Bohem press, 1992. 1.1

[3] Ryan Enright, Shenghui Lei, Kevin Nolan, Ian Mathews, Alexandre Shen, Guillaume Levaufre, Ronan Frizzell, Guang-Hua Duan, and Domhnaill Hernon. A vision for thermally integrated photonics systems. *Bell Labs Technical Journal*, 19:31–45, 2014. (document), 1.1, 1.2, 1.2, 1.3

[4] Marc Taubenblatt. Optical interconnects for high performance computing. In *Optical Fiber Communication Conference*, page OThH3. Optical Society of America, 2011. 1.2

[5] Seamus Hickey, Jeff Punch, John Daly, and Nicholas Jeffers. The influence of heat spreading on the thermal control of photonics integrated circuits. In *ASME 2011 International Mechanical Engineering Congress and Exposition*, pages 35–42. American Society of Mechanical Engineers, 2011. 1.2

[6] N Jeffers, J Stafford, K Nolan, B Donnelly, R Enright, J Punch, A Waddell, L Erlich, J OŠConnor, A Sexton, et al. Microfluidic cooling of photonic integrated circuits (pics). In *4th European Conference on Microfluidics, Limerick, Ireland*, pages 10–12, 2014. 1.2, 1.3

[7] Allan D Kraus and Avram Bar-Cohen. *Thermal analysis and control of electronic equipment*, volume 1. McGraw Hill, 1983. 1.2, 2.1, 2.1.4, 3.3.1, 4.1.1, 4.1.2

[8] Laird. *Thermoelectric Modules 2015*. Laird Technologies, 2015. (document), 1.3

[9] Colm O'Dwyer, Renkun Chen, Jr-Hau He, Jaeho Lee, and Kafil M Razeeb. Scientific and technical challenges in thermal transport and thermoelectric materials and devices. *ECS Journal of Solid State Science and Technology*, 6:3058 – 3064, 2017. 1.3

[10] TC Harman and JM Honig. Theory of galvano-thermomagnetic energy conversion devices. ii. refrigerators and heat pumps. *Journal of Applied Physics*, 33(11):3188–3194, 1962. 1.4

[11] Akram I Boukai, Yuri Bunimovich, Jamil Tahir-Kheli, Jen-Kan Yu, William A Goddard Iii, and James R Heath. Silicon nanowires as efficient thermoelectric materials. In *Materials For Sustainable Energy: A Collection of Peer-Reviewed Research and Review Articles from Nature Publishing Group*, pages 116–119. World Scientific, 2011. 1.4

[12] Sabah K Bux, Richard G Blair, Pawan K Gogna, Hohyun Lee, Gang Chen, Mildred S Dresselhaus, Richard B Kaner, and Jean-Pierre Fleurial. Nanostructured bulk silicon as an effective thermoelectric material. *Advanced Functional Materials*, 19(15):2445–2452, 2009. 1.4

[13] Allon I Hochbaum, Renkun Chen, Raul Diaz Delgado, Wenjie Liang, Erik C Garnett, Mark Najarian, Arun Majumdar, and Peidong Yang. Enhanced thermoelectric performance of rough silicon nanowires. *Nature*, 451(7175):163, 2008. 1.4

[14] H Iwasaki and H Hori. Thermoelectric property measurements by the improved harman method. In *Thermoelectrics, 2005. ICT 2005. 24th International Conference on*, pages 513–516. IEEE, 2005. 1.4

[15] W Kobayashi, W Tamura, and I Terasaki. Thermal conductivity and dimensionless figure of merit of thermoelectric rhodium oxides measured by a modified harman method. *Journal of electronic materials*, 38(7):964–967, 2009. 1.4

[16] Bed Poudel, Qing Hao, Yi Ma, Yucheng Lan, Austin Minnich, Bo Yu, Xiao Yan, Dezhi Wang, Andrew Muto, Daryoosh Vashaee, et al. High-thermoelectric performance of nanostructured bismuth antimony telluride bulk alloys. *Science*, 320(5876):634–638, 2008. 1.4

[17] K Valset. A technique to measure thermoelectric figure of merit and heat flow at high temperatures by cancelling heat losses. *Materials Today: Proceedings*, 2(2):721–728, 2015. 1.4

[18] Rama Venkatasubramanian, Edward Siivola, Thomas Colpitts, and Brooks O'quinn. Thin-film thermoelectric devices with high room-temperature figures of merit. *Nature*, 413(6856):597, 2001. 1.4

[19] Eduardo E Castillo, Claudiu L Hapenciuc, and Theodorian Borca-Tasciuc. Thermoelectric characterization by transient harman method under nonideal contact and boundary conditions. *Review of Scientific Instruments*, 81(4):044902, 2010. 1.4

[20] LV Van der Pauw. A method of measuring specific resistivity and hall effect of discs of arbitrary shape. *Philips Res. Rep*, 13(1):1–9, 1958. 1.4

[21] Johannes de Boor and Volker Schmidt. Complete characterization of thermoelectric materials by a combined van der pauw approach. *Advanced Materials*, 22(38):4303–4307, 2010. (document), 1.4, 1.5

[22] Richard J Buist. A new method for testing thermoelectric materials and devices. In *11th International Conference on Thermoelectrics*, 1992. 1.5

[23] D Mitrani, JA Tome, J Salazar, A Turo, MJ Garcia, and JA Chavez. Dynamic measurement system of thermoelectric module parameters. In *Thermoelectrics, 2003 Twenty-Second International Conference on-ICT*, pages 524–527. IEEE, 2003. 1.5

[24] Daniel Mitrani, José Antonio Tomé, Jordi Salazar, Antoni Turó, Miguel Jesús García, and Juan Antonio Chávez. Methodology for extracting thermoelectric module parameters. *IEEE transactions on instrumentation and measurement*, 54(4):1548–1552, 2005. (document), 1.5, 1.6

[25] Suresh V Garimella. Advances in mesoscale thermal management technologies for microelectronics. *Microelectronics Journal*, 37(11):1165–1185, 2006. 1.5

[26] Kafil M Razeeb, Eric Dalton, Graham Lawerence William Cross, and Anthony James Robinson. Present and future thermal interface materials for electronic devices. *International Materials Reviews*, 63(1):1–21, 2018. 1.5

[27] Paul Kolodner. High-precision thermal and electrical characterization of thermoelectric modules. *Review of Scientific Instruments*, 85(5):–, 2014. 1.5, 1.6, 2.4, 3.2, 4.1.1

[28] Gao Min and DM Rowe. A novel principle allowing rapid and accurate measurement of a dimensionless thermoelectric figure of merit. *Measurement Science and Technology*, 12(8):1261, 2001. 1.5

[29] Zeshen Wang, Jianzhong Zhang, and Yang Liu. A practical method for measuring thermal conductance and cooling power of thermoelectric modules. In *Thermoelectrics, 2001. Proceedings ICT 2001. XX International Conference on*, pages 515–518. IEEE, 2001. (document), 1.6, 1.7

[30] Emil Sandoz-Rosado and Robert J Stevens. Experimental characterization of thermoelectric modules and comparison with theoretical models for power generation. *Journal of electronic materials*, 38(7):1239–1244, 2009. 1.6

[31] Kelly Lofgreen. A metrology for comprehensive thermoelectric device characterization. Master's thesis, Arizona State University, 2011. 1.6, 1

[32] L Rauscher, S Fujimoto, HT Kaibe, and S Sano. Efficiency determination and general characterization of thermoelectric generators using an absolute measurement of the heat flow. *Measurement Science and Technology*, 16(5):1054, 2005. (document), 1.6, 2.4, 2.6

[33] D Beretta, M Massetti, G Lanzani, and M Caironi. Thermoelectric characterization of flexible micro-thermoelectric generators. *Review of Scientific Instruments*, 88(1):015103, 2017. (document), 1.6, 1.8

[34] S Hickey, J Punch, and N Jeffers. Benchmarking of a novel contactless characterisation method for micro thermoelectric modules (utems). In *Journal of Physics: Conference Series*, volume 525, page 012021. IOP Publishing, 2014. 1.7

[35] David Michael Rowe. *CRC handbook of thermoelectrics*. CRC press, 1995. Peltier coolers performance measurement methodology. Buist. 2.1, 2.1.4

[36] Marc Hodes. On one-dimensional analysis of thermoelectric modules (tems). *IEEE Transactions on Components and packaging technologies*, 28(2):218–229, 2005. 1

[37] Mathworks. *Mathlab Curve Fitting Toolbox*. https://uk.mathworks.com/help/curvefit/product-description.html, 2018. 2.5

[38] Abderrahim Boudenne, Laurent Ibos, and Yves Candau. Analysis of uncertainties in thermophysical parameters of materials obtained from a periodic method. *Measurement Science and Technology*, 17(7):1870, 2006. 3.4.3

[39] WJ Parker, RJ Jenkins, CP Butler, and GL Abbott. Flash method of determining thermal diffusivity, heat capacity, and thermal conductivity. *Journal of applied physics*, 32(9):1679–1684, 1961. 1

[40] Stephen J Kline and FA McClintock. Describing uncertainties in single-sample experiments. *Mechanical engineering*, 75(1):3–8, 1953. 3.4.3

[41] Jason Stafford, Ryan Enright, and Roger Kempers. Rarefied conditions in the convective-diffusive regimes of a disc in natural convection. In *ASME 2013 4th International Conference on Micro/Nanoscale Heat and Mass Transfer*, pages V001T11A005–V001T11A005. American Society of Mechanical Engineers, 2013. 4.1.3

[42] JP Holman and PRS White. *Heat Transfer Seventh Edition in SI Units*, volume 7. McGraw Hill, 1992. 4.2.1

Appendix A

Data Sheets

Peltier Cooler - 4.5W

multicomp

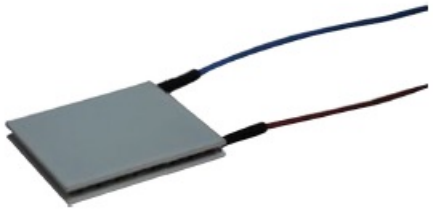

Features:

Transducer Function: Thermoelectric modules

Specifications:

Parameters			Remarks
Internal resistance	1.76Ω ± 10%		Note-1
Imax.	2A		Note-2
Vmax.	3.8V		Note-3
	Th=25°C		
Qmax.	4.4W		Note-4
⊿Tmax.	73°C		Note-5
Solder Melting Point	232°C		Note-6
Max. Compress	1MPa		Note-7
Operating Temperature	-150°C to +200°C		
External Depth	4.8mm		
External Length / Height	15mm		

Note-1 Measured by AC 4-terminal method at 25°C
Note-2 Max. current at ⊿Tmax
Note-3 Max. voltage at ⊿Tmax
Note-4 Max. cooling capacity at Imax.,Vmax. and ⊿T=0°C
Note-5 Max. temperature difference at Imax.,Vmax. and Q=0W
(Max. parameters are measured in a vacuum 1.3P)
Note-6 The solder melting point of thermoelectric module
Note-7 Recommended Max. compression (not destruction limit)

Recommendations:

- ON/OFF cycling mode reliability at high temperature
- Recommended operation current not higher than 0.7 of Imax
- Preferable application; thermal management

Figure A.1: Multicomp Data Sheet part 1

Peltier Cooler - 4.5W

multicomp

2-3 Performance Graph (298K and 323K respectively)

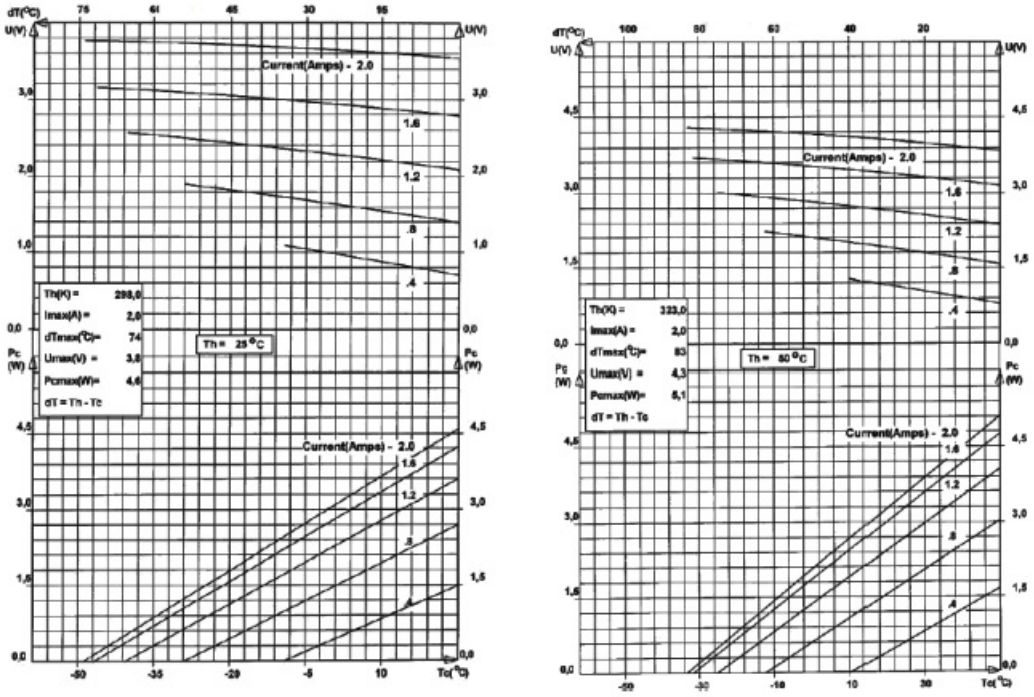

Part Number Table

Description	Part Number
Peltier Cooler, 4.5W	MCPF-031-10-25

Figure A.2: Multicomp Data Sheet part 2

ΔT Defined

It would be tempting to specify our coolers by the more impressive ΔT_{max} value. However, with heating-up of the hot side and usually less-than-optimal thermal coupling to the heat sink in mind, we have decided to be conservative and publish more realistic net values T_c !

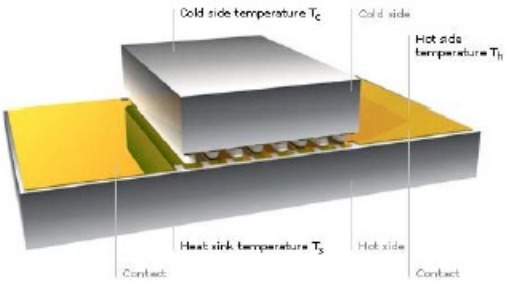

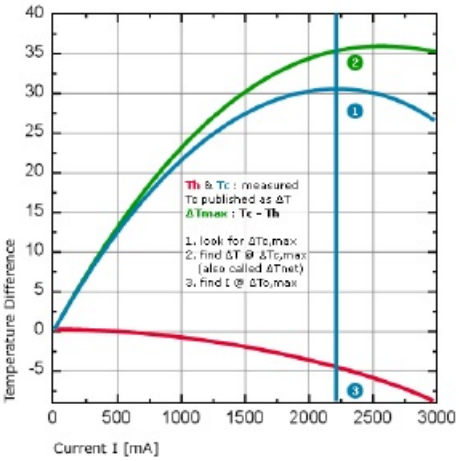

Product Family

Type	Dimensions [mm] cold side hot side	Thickness [µm]	Number of leg pairs	Thermal Resistance at 85 °C	Electric Resistance at 23 °C	ΔT_{max} at 85 °C	Q_{max} at 85 °C	I_{max} at 85 °C
MPC-D303	1.18 x 0.832 2.142 x 0.832	1090	4	135 K/W	0.3 Ω	48 K	0.33 W	1.2 A
MPC-D305	0.94 x 0.832 1.666 x 0.832	1090	3	175 K/W	0.3 Ω	40 K	0.23 W	1.0 A

micropelt
Cooling in new dimensions.

Figure A.3: Micropelt MPC D303 Data Sheet part 1

Technical Overview MPC-D303

Calculated values based on material properties at selected ambient temperatures T_a:

$T_a = 25\ °C$ $T_a = 60\ °C$ $T_a = 85\ °C$

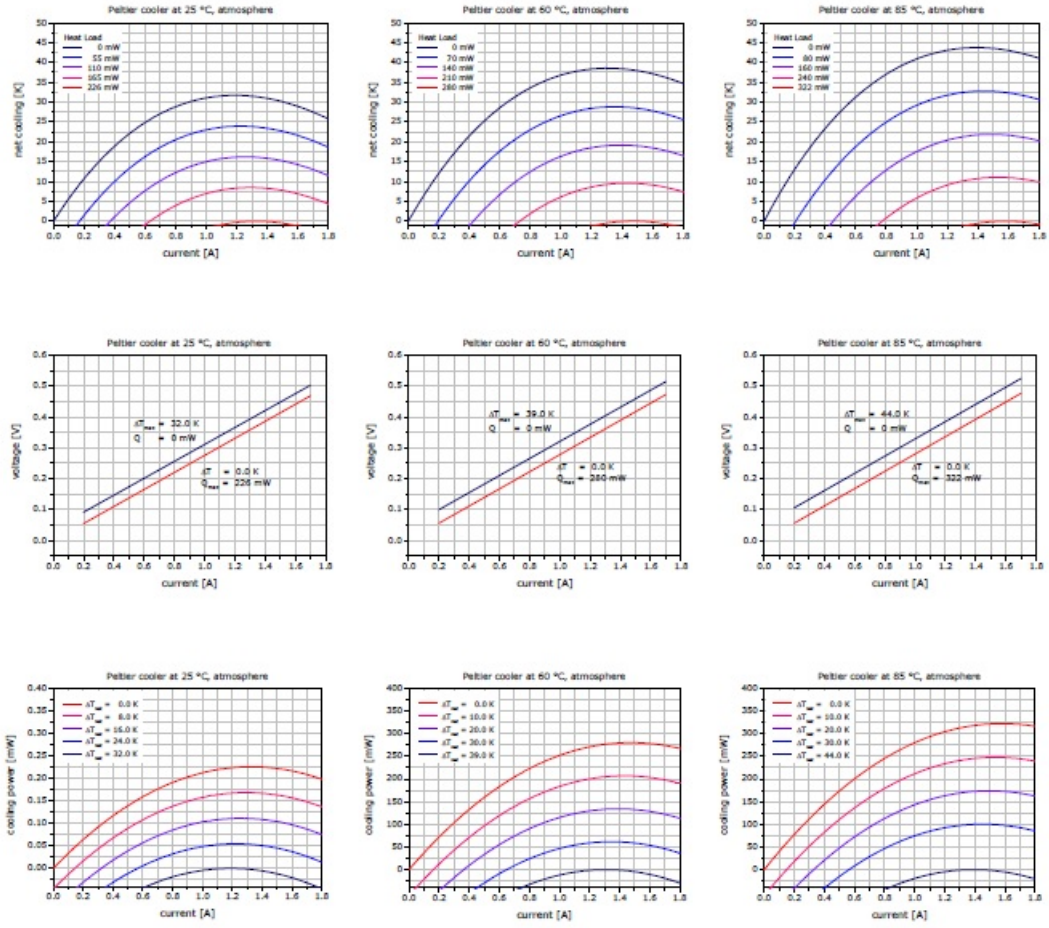

Figure A.4: Micropelt MPC D303 Data Sheet part 2

Appendix B

Calibration Certificates

CERTIFICATE OF CALIBRATION

Issued By
Calibration Specialists Ltd., Holland Rd., National Technology Pk.,
Castletroy, Limerick. Ireland.
Tel: +353 61 330333 - Fax: +353 61 330452 - website: www.calibrationspecialists.ie

An INAB Accredited Calibration Laboratory Reg No.001C — Certificate No: 1311004

Date of Issue: 7TH NOVEMBER 2013 — Approved Signatory: Tony O'Mara

Timmy Davern (Head of Laboratory.)
Tony O'Mara (Technical Manager.)

Category: A - C..S.L. Co. LIMERICK

Customer: UNIVERSITY OF LIMERICK

Address: Co. LIMERICK

Details Of Unit Calibrated:

Manufacturer:	FLUKE	Date Received:	04TH ONVEMBER 2013
Model:	37	Date Calibrated:	06TH NOVEMBER 2013
Serial No:	004825314	Calibrated by:	DOMINIK STAWIARSKI
Ref No:	N/A	Temperature:	(23± 5) °C
Description:	DIGITAL MULTIMITER	Humidity:	(50±25) %

The above instrument was tested against the manufacturer's accuracy specification at the points shown and the results are tabulated in the following report. This report relates solely to the instrument described above.

This certificate is issued in accordance with the conditions of accreditation laid down by the Irish National Accreditation Board, which has assessed the measurement capability of the Laboratory. The reported results are traceable to recognised National and International standards. The copyright of this report is reserved to Calibration Specialists Limited (CSL) and it shall not be used either in whole or in part for the purposes of advertising, publicity, litigation or otherwise without the prior consent of CSL. This calibration certificate contains information belonging to Calibration Specialists Ltd.,which is confidential and/or legally privileged. Information is intended only for the use of the entity named above. If you have received this certificate in error,please notify us by telephone immediately at the above number.

The reported expanded uncertainty is stated as the standard uncertainty of measurement multiplied by the coverage factor k=2, which for a normal distribution corresponds to a coverage probability of approximately 95%. The standard uncertainty of measurement has been determined in accordance with EAL Publication EA-4/02.

Figure B.1: Fluke 37 multimeter calibration certificate part 1

CERTIFICATE OF CALIBRATION

Issued By

Calibration Specialists Ltd., Holland Rd., National Technology Pk., Castletroy, Limerick. Ireland.
Tel: +353 61 330333 - Fax: +353 61 330452 - website: www.calibrationspecialists.ie

Date of Calibration: 06TH NOVEMBER 2013 **Certificate No:** 1311004

Method: The unit under test was first allowed to stabilise. Precisely known values were then applied to the input of the unit under test and the resultant readings compared against manufacturer's specifications. The Fluke 37 Multimeter, specification data sheet provided by manufacturer was used as a base to verify accuracy of the UUT.

AC VOLTAGE ACCURACY TEST

RANGE (V)	VALUE (V)	MIN (V)	ACTUAL (V)	MAX (V)	Uncertainty (±V)
320.0 m	300.0 m/1kHz	298.2 m	299.1 m	301.8 m	0.4 m
m	300.0 m/5kHz	293.7 m	299.2 m	306.3 m	0.4 m
m	300.0 m/20kHz	287.0 m	299.4 m	313.0 m	0.4 m
3.200	3.000 1kHz	2.982	2.994	3.018	0.003
	3.000 5kHz	2.937	2.985	3.063	0.003
	3.000 20kHz	2.870	2.995	3.130	0.003
32.00	30.00 1kHz	29.82	29.99	30.18	0.03
	30.00 5kHz	29.37	29.96	30.63	0.03
	30.00 20kHz	28.70	29.93	31.30	0.03
320.0	300.0 1kHz	298.2	300.0	301.8	0.2
1000	750 1kHz	740	749	761	1

DC VOLTAGE ACCURACY TEST

RANGE (V)	VALUE (V)	MIN (V)	ACTUAL (V)	MAX (V)	Uncertainty (±V)
320.0 m	300.0 m	299.6 m	300.0 m	300.4 m	0.1 m
3.200	3.000	2.996	3.001	3.004	0.001
32.00	30.00	29.96	30.01	30.04	0.01
320.0	300.0	299.6	300.1	300.4	0.1
1000	1000	998	1000	1002	1

AC CURRENT @ 100 Hz ACCURACY TEST

RANGE (A)	VALUE (A)	MIN (A)	ACTUAL (A)	MAX (A)	Uncertainty (±A)
320.0 µ	300.0 µ	295.3 µ	299.8 µ	304.7 µ	0.6 µ
3200 µ	3000 µ	2953 µ	3000 µ	3047 µ	5 µ
32.00 m	30.00 m	29.53 m	30.02 m	30.47 m	0.05 m
320.0 m	300.0 m	295.3 m	300.6 m	304.7 m	0.5 m
10.00	1.90	1.85	1.89	1.95	0.01

DC CURRENT ACCURACY TEST

RANGE (A)	VALUE (A)	MIN (A)	ACTUAL (A)	MAX (A)	Uncertainty (±A)
320.0 µ	300.0 µ	297.6 µ	299.9 µ	302.5 µ	0.2 µ
3200 µ	3000 µ	2976 µ	3000 µ	3025 µ	2 µ
32.00 m	30.00 m	29.76 m	30.02 m	30.25 m	0.02 m
320.0 m	300.0 m	297.6 m	300.6 m	302.5 m	0.2 m
10.00	1.90	1.87	1.89	1.93	0.01

Figure B.2: Fluke 37 multimeter calibration certificate part 2

CERTIFICATE OF CALIBRATION

Issued By
Calibration Specialists Ltd., Holland Rd., National Technology Pk., Castletroy, Limerick. Ireland.
Tel: +353 61 330333 - Fax: +353 61 330452 - website: www.calibrationspecialists.ie

Date of Calibration: 06TH NOVEMBER 2013 **Certificate No:** 1311004

RESISTANCE ACCURACY TEST

RANGE (Ω)	VALUE (Ω)	MIN (Ω)	ACTUAL (Ω)	MAX (Ω)	Uncertainty (±Ω)
320.0	100.0	99.5	100.2	100.5	0.1
3.200 k	1.000 k	0.997 k	1.000 k	1.003 k	0.001 k
32.00 k	10.00 k	9.97 k	10.00 k	10.03 k	0.001 k
320.0 k	100.0 k	99.7 k	100.0 k	100.3 k	0.001 k
3.200 M	1.000 M	0.997 M	1.000 M	1.003 M	0.001 M
32.00 M	10.00 M	9.89 M	10.00 M	10.11 M	0.001 M

DIODE TEST

RANGE (V)	VALUE (V)	MIN (V)	ACTUAL (V)	MAX (V)	Uncertainty (±V)
2.080	1.000	0.998	0.999	1.002	0.001

RESISTANCE TEST	RESULT
CONDUCTANCE TEST	PASS
REL FUNCTION	PASS
MIN/MAX FUNCTION	PASS
HOLD FUNCTION	PASS

Standards Used:
Asset No. 192 CALIBRATOR, Cal. due Feb-2014,

Comments:
Upon receipt this unit meets or exceeds manufacturer's specification at all points tested.
No adjustments were necessary.
The 630mA Fuse was replaced.
Functional Tests do not form part of our Accredited Schedule.
----------End of Certificate----------

Figure B.3: Fluke 37 multimeter calibration certificate part 3

CERTIFICATE OF CALIBRATION

Issued By
Calibration Specialists Ltd., Holland Rd., National Technology Pk.,
Castletroy, Limerick. Ireland.
Tel: +353 61 330333 - Fax: +353 61 330452 - website: www.calibrationspecialists.ie

An INAB Accredited Calibration Laboratory Reg No.001C

Certificate No: 1311005

Date of Issue: 7TH NOVEMBER 2013

Approved Signatory:

Timmy Davern (Head of Laboratory.)
Tony O'Mara (Technical Manager.)

Category: A - C..S.L. Co. LIMERICK

Customer: UNIVERSITY OF LIMERICK

Address: Co. LIMERICK

Details Of Unit Calibrated:

Manufacturer:	FLUKE	Date Received:	04TH NOVEMBER 2013
Model:	45	Date Calibrated:	06TH NOVEMBER 2013
Serial No:	7594003	Calibrated By:	DOMINIK STAWIARSKI
Ref No:	N/A	Temperature:	(23± 5) °C
Description:	DUAL DISPLAY DIGITAL MULTIMETER	Humidity:	(50±25) %

The above instrument was tested against the manufacturer's accuracy specification at the points shown and the results are tabulated in the following report. This report relates solely to the instrument described above.

This certificate is issued in accordance with the conditions of accreditation laid down by the Irish National Accreditation Board, which has assessed the measurement capability of the Laboratory. The reported results are traceable to recognised National and International standards. The copyright of this report is reserved to Calibration Specialists Limited (CSL) and it shall not be used either in whole or in part for the purposes of advertising, publicity, litigation or otherwise without the prior consent of CSL. This calibration certificate contains information belonging to Calibration Specialists Ltd.,which is confidential and/or legally privileged. Information is intended only for the use of the entity named above. If you have received this certificate in error,please notify us by telephone immediately at the above number.

The reported expanded uncertainty is stated as the standard uncertainty of measurement multiplied by the coverage factor k=2, which for a normal distribution corresponds to a coverage probability of approximately 95%. The standare uncertainty of measurement has been determined in accordance with EAL Publication EA-4/02.

Figure B.4: Fluke 45 multimeter calibration certificate part 1

CERTIFICATE OF CALIBRATION

Issued By

Calibration Specialists Ltd., Holland Rd., National Technology Pk., Castletroy, Limerick. Ireland.
Tel: +353 61 330333 - Fax: +353 61 330452 - website: www.calibrationspecialists.ie

Date of Calibration: 04TH NOVEMBER 2013 **Certificate No:** 1311005

Method: The unit under test was first allowed to stabilise. Precisely known values were then applied to the input of the unit under test and the resultant readings compared against manufacturer's specifications. The Manufacturer Published Performance Test Procedure is carried out in reference to the Fluke 45 Dual Display User Manual P/N 855981 Rev.2, 12/89 published in 1989.

DC Voltage Test

Range (V)	Value (V)	Min (V)	Actual (V)	Max (V)	Uncertainty (±V)
(slow) 100 m	Short	-0.006 m	0.000 m	0.006 m	0.0005 m
	90 m	89.971 m	89.978 m	90.029 m	0.004 m
(slow) 1000 m	900 m	899.71 m	899.79 m	900.29 m	0.02 m
300 m	Short	-0.02 m	0.00 m	0.02 m	0.005 m
	300 m	299.90 m	299.94 m	300.10 m	0.01 m
3	3	2.9990	2.9993	3.0010	0.0001
	-3	-3.0010	-2.9993	-2.9990	0.0001
30	30	29.990	29.992	30.010	0.001
300	300	299.90	299.93	300.10	0.01
1000	1000	999.5	999.8	1000.5	0.1

AC Voltage Test

Range (V)	Value (V)	Min (V)	Actual (V)	Max (V)	Uncertainty (±V)	
300 m	#Short	-0.75 m	0.12 m	0.75 m	0.005 m	
	15m, 1kHz	14.87 m	14.99 m	15.13 m	0.01 m	
	15m, 100kHz	13.75 m	14.15 m	16.25 m	0.02 m	
	300m, 1kHz	299.30 m	299.88 m	300.70 m	0.05 m	
	300m,100kHz	284.50 m	293.34 m	315.50 m	0.07 m	
3	3, 1kHz	2.9930	2.9985	3.0070	0.0005	
30	30, 1kHz	29.930	29.984	30.070	0.005	
300	300, 1kHz	299.30	299.88	300.70	0.09	
750	750, 1kHz	747.5	741.1	752.5	0.3	Fail

DC Current

Range (A)	Value (A)	Min (A)	Actual (A)	Max (A)	Uncertainty (±A)
30 m	30.000 m	29.982 m	FAULTY m	30.018 m	0.007 m
100 m	90.00 m	89.93 m	FAULTY m	90.07 m	0.007 m
10	1.900	1.891	1.900	1.909	0.001

Figure B.5: Fluke 45 multimeter calibration certificate part 2

CERTIFICATE OF CALIBRATION

Issued By

Calibration Specialists Ltd., Holland Rd., National Technology Pk., Castletroy, Limerick. Ireland.
Tel: +353 61 330333 - Fax: +353 61 330452 - website: www.calibrationspecialists.ie

Date of Calibration: 04TH NOVEMBER 2013 Certificate No: 1311005

AC Current @ 1kHz

Range (A)	Value (A)	Min (A)	Actual (A)	Max (A)	Uncertainty (±A)
30 m	30.000 m	29.840 m	FAULTY m	30.160 m	0.020 m
100 m	90.00 m	89.40 m	FAULTY m	90.60 m	0.07 m
10	1.900	1.871	1.898	1.929	0.0020

Resistance

Range (Ω)	Value (Ω)	Min (Ω)	Actual (Ω)	Max (Ω)	Uncertainty (±Ω)
300	#Short	0.00	0.02	0.04	0.005
	99.9897	99.90	99.99	100.08	0.01
3 k	#Short	0.0000 k	0.0001 k	0.0002 k	0.0001 k
	0.9998975 k	0.9992 k	0.9999 k	1.0026 k	0.0001 k
30 k	9.99956 k	9.993 k	10.000 k	10.007 k	0.001 k
300 k	99.9933 k	99.92 k	100.03 k	100.06 k	0.01 k
3 M	0.9998916 M	0.9991 M	0.9998 M	1.0006 M	0.0001 M
30 M	9.998427 M	9.970 M	9.997 M	10.026 M	0.001 M

Frequency Test (Rate Slow/Medium @1V)

Range (Hz)	Value (Hz)	Min (Hz)	Actual (Hz)	Max (Hz)	Uncertainty (±Hz)
100 k	100.000 k	99.949 k	99.999 k	100.060 k	0.0100 k

Diode Test

Range (V)	Value (V)	Min (V)	Actual (V)	Max (V)	Uncertainty (±V)	
n/a	short	-0.0008 (tone)	0.0001	0.0008 (tone)	0.0001	PASS
n/a	open	OL	OL	OL	n/a	PASS

Figure B.6: Fluke 45 multimeter calibration certificate part 3

CERTIFICATE OF CALIBRATION

Issued By

Calibration Specialists Ltd., Holland Rd., National Technology Pk., Castletroy, Limerick. Ireland.
Tel: +353 61 330333 - Fax: +353 61 330452 - website: www.calibrationspecialists.ie

Date of Calibration: 06TH NOVEMBER 2013 **Certificate No:** 1311005

MEASUREMENTS TAKEN AFTER ADJUSTMENTS

AC Voltage Test

Range (V)	Value (V)	Min (V)	Actual (V)	Max (V)	Uncertainty (±V)
300 m	#Short	-0.75 m	0.12 m	0.75 m	0.005 m
	15m, 1kHz	14.87 m	15.01 m	15.13 m	0.01 m
	15m, 100kHz	13.75 m	14.20 m	16.25 m	0.02 m
	300m, 1kHz	299.30 m	299.99 m	300.70 m	0.05 m
	300m,100kHz	284.50 m	293.99 m	315.50 m	0.07 m
3	3, 1kHz	2.9930	2.9999	3.0070	0.0005
30	30, 1kHz	29.930	30.000	30.070	0.005
300	300, 1kHz	299.30	300.00	300.70	0.09
750	750, 1kHz	747.5	750.0	752.5	0.3

Standards Used:

Asset No. 192 CALIBRATOR, Cal. due Feb-2014,

Comments:

On receipt this unit was found to be outside manufacturer's published specification at the points identified with a "FAIL". It was adjusted as per Manufacturer's Published Service Manual and any necessary readings retaken.
The AC/DC 30mA and 100mA Current Range were found to be FAULTY, no repair was carried out.
This unit meets or exceeds manufacturer's specifications at all other points tested.
Functional Test, Short verification for 2 Wire Resistance and AC Volts do not form part of our Accredited Schedule.

----------END OF CERTIFICATE----------

Figure B.7: Fluke 45 multimeter calibration certificate part 4

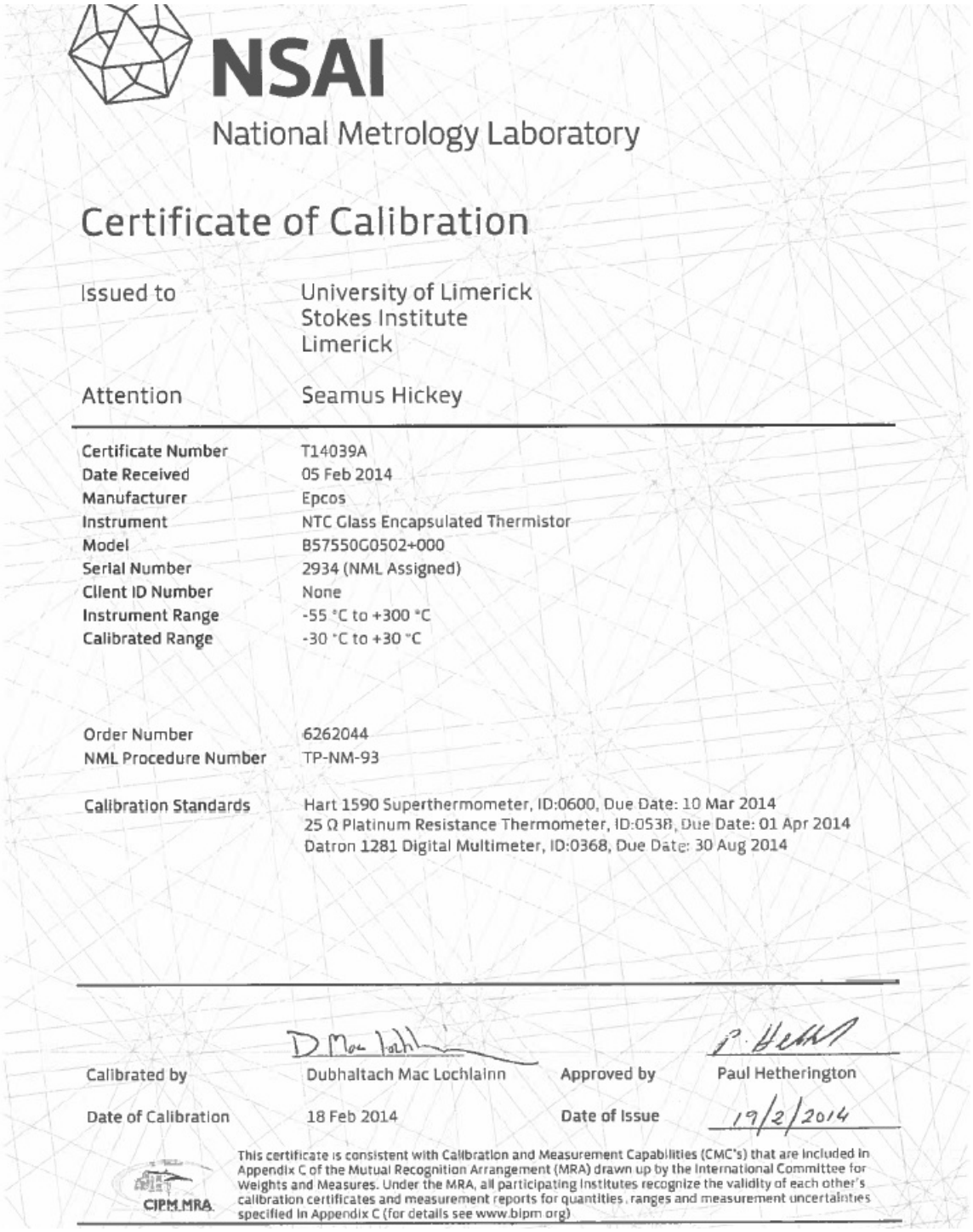

NSAI

National Metrology Laboratory

Certificate of Calibration

Issued to	University of Limerick Stokes Institute Limerick
Attention	Seamus Hickey

Certificate Number	T14039A
Date Received	05 Feb 2014
Manufacturer	Epcos
Instrument	NTC Glass Encapsulated Thermistor
Model	B57550G0502+000
Serial Number	2934 (NML Assigned)
Client ID Number	None
Instrument Range	-55 °C to +300 °C
Calibrated Range	-30 °C to +30 °C
Order Number	6262044
NML Procedure Number	TP-NM-93
Calibration Standards	Hart 1590 Superthermometer, ID:0600, Due Date: 10 Mar 2014 25 Ω Platinum Resistance Thermometer, ID:0538, Due Date: 01 Apr 2014 Datron 1281 Digital Multimeter, ID:0368, Due Date: 30 Aug 2014

Calibrated by	Dubhaltach Mac Lochlainn	Approved by	Paul Hetherington
Date of Calibration	18 Feb 2014	Date of Issue	19/2/2014

CIPM MRA

This certificate is consistent with Calibration and Measurement Capabilities (CMC's) that are included in Appendix C of the Mutual Recognition Arrangement (MRA) drawn up by the International Committee for Weights and Measures. Under the MRA, all participating Institutes recognize the validity of each other's calibration certificates and measurement reports for quantities, ranges and measurement uncertainties specified in Appendix C (for details see www.bipm.org)

Figure B.8: Epcos thermistor calibration certificate part 1

NSAI
National Metrology Laboratory

Certificate No.: T14039A

Specifications

Resistance Tolerance ±2%

Results

Reference Reading (°C)	UUT Reading (Kohms)
-29.9941	58.8344
-15.0059	27.9209
-0.0021	14.0094
14.9973	7.4393
30.0013	4.1643

Comments

The probe was immersed to 195 mm in the constant temperature metrology wells.

The sensor resistance was measured using a 100µA current on the 100Kokm range setting of the digital multimeter, listed in the standards above.

The estimated uncertainty associated with the reference reading is:

±0.05 °C at all the points calibrated

This reported expanded uncertainty of measurement (which includes the uncertainty of the reference temperature) is stated as the standard uncertainty of measurement multiplied by the coverage factor $k = 2$, which for a normal distribution corresponds to a coverage probability of approximately 95%. The standard uncertainty of measurement has been determined in accordance with ISO "Guide to the expression of uncertainty in measurement".

This calibration was undertaken at an ambient laboratory temperature of 20 °C ± 2 °C

This certificate provides traceability of measurement to recognised national standards, and to the units of measurement realised at the NSAI National Metrology Laboratory (NML) or other recognised national standards laboratories in accordance with the International Temperature Scale of ITS 90.

Figure B.9: Epcos thermistor calibration certificate part 2

Appendix C

Experimental software

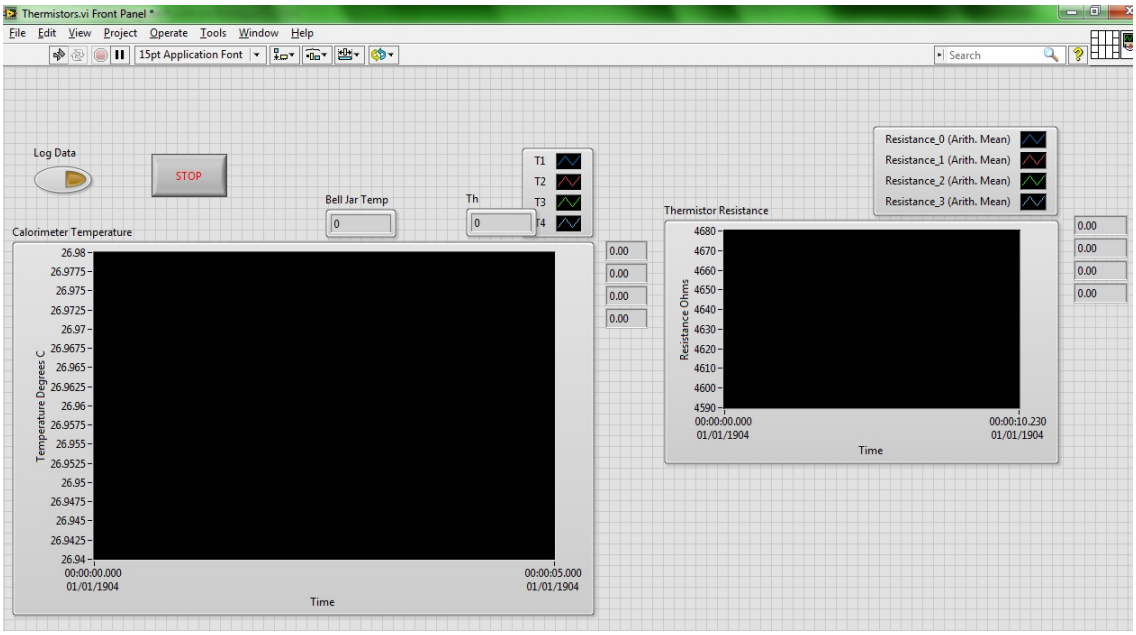

Figure C.1: Labview front panel

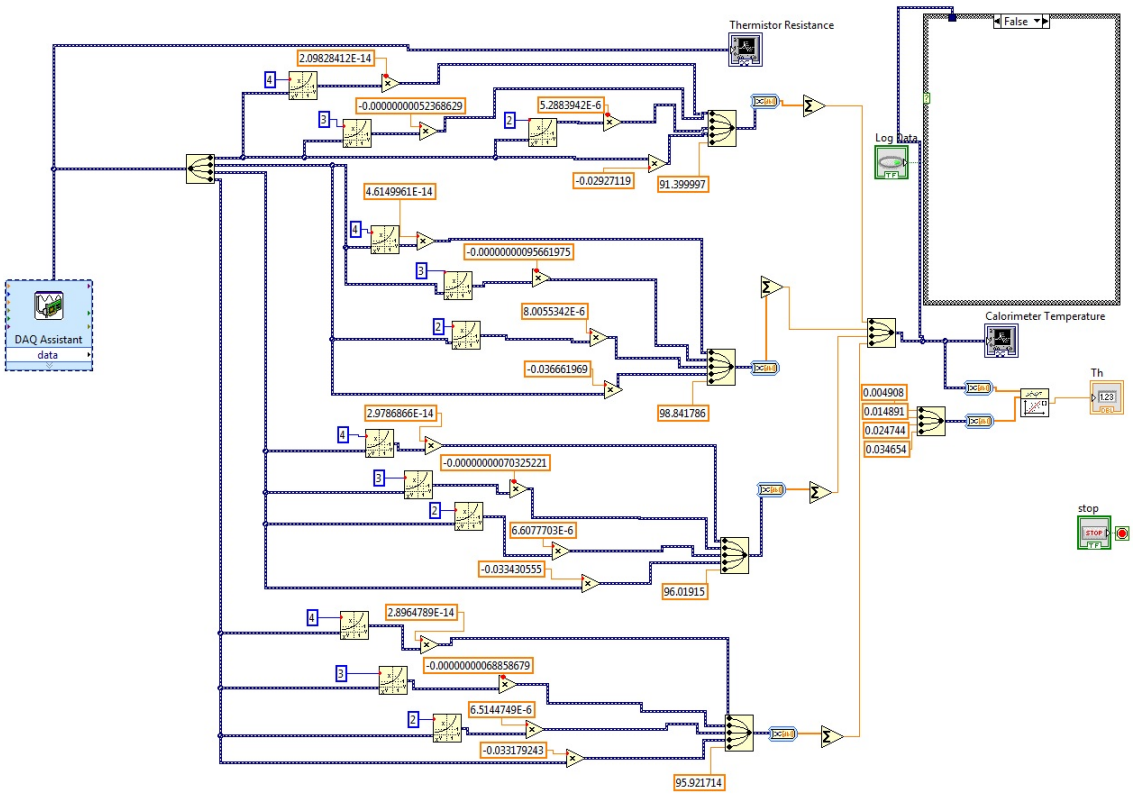

Figure C.2: Labview block diagram